An astronomically dated record of Earth's climate and its predictability over the last 66 Million Years

Authors: Thomas Westerhold[1*], Norbert Marwan[2,3], Anna Joy Drury[1,4], Diederik Liebrand[1], Claudia Agnini[5], Eleni Anagnostou[6], James S. K. Barnet[7,8], Steven M. Bohaty[9], David De Vleeschouwer[1], Fabio Florindo[10,11], Thomas Frederichs[1,12], David A. Hodell[13], Ann E. Holbourn[14], Dick Kroon[15], Vittoria Lauretano[16], Kate Littler[7], Lucas J. Lourens[17], Mitchell Lyle[18], Heiko Pälike[1], Ursula Röhl[1], Jun Tian[19], Roy H. Wilkens[20], Paul A. Wilson[9], James C. Zachos[21]

Affiliations:

[1]MARUM – Center for Marine Environmental Sciences, University of Bremen, 28359 Bremen, Germany.

[2]Member of the Leibniz Association, Potsdam Institute for Climate Impact Research (PIK), 14412 Potsdam, Germany

[3]University of Potsdam, Institute of Geosciences, 14469 Potsdam, Germany

[4]Department of Earth Sciences, University College London, Gower Street, London, WC1E 6BT, UK.

[5]Dipartimento di Geoscienze, Università degli Studi di Padova, Via Gradenigo 6, I-35131 Padova, Italy.

[6]GEOMAR Helmholtz-Zentrum für Ozeanforschung Kiel, Wischhofstrasse 1-3, 24148 Kiel, Germany.

[7]Camborne School of Mines and Environment and Sustainability Institute, University of Exeter, Penryn Campus, Penryn, UK.

[8]School of Earth and Environmental Sciences, University of St Andrews, St Andrews, Scotland, UK

[9]Ocean and Earth Science, University of Southampton, National Oceanography Centre, Southampton, UK.

[10]Istituto Nazionale di Geofisica & Vulcanologia, INGV, Rome, Italy.

[11]Institute for Climate Change Solutions, Pesaro e Urbino, Italy

[12]Faculty of Geosciences, University of Bremen, Bremen, Germany.

[13]Godwin Laboratory for Palaeoclimate Research, Department of Earth Sciences, University of Cambridge, Cambridge, UK.

[14]Institute of Geosciences, Christian-Albrechts-University, Kiel 24118, Germany.

[15]School of GeoSciences, University of Edinburgh, Edinburgh, UK.

[16]School of Chemistry, University of Bristol, Bristol BS8 1TS, UK.

[17]Department of Earth Sciences, Faculty of Geosciences, Utrecht University, Princetonlaan 8a, 3584 CB Utrecht, Netherlands.

[18]College of Earth, Ocean, and Atmospheric Science, Oregon State University, Corvallis, Oregon 97331, USA.

[19]State Key Laboratory of Marine Geology, Tongji University, Siping Road 1239, Shanghai 200092, PR China.

[20]University of Hawaii, School of Ocean and Earth Science and Technology, Honolulu Hawaii 96822, USA.

[21]Department of Earth and Planetary Sciences, University of California Santa Cruz, California, USA.

*Correspondence to: twesterhold@marum.de

Abstract:

Much of our understanding of Earth's past climate comes from the measurement of oxygen and carbon isotope variations in deep-sea benthic foraminifera. Yet, long intervals in existing records lack the temporal resolution and age control needed to thoroughly categorize climate states of the Cenozoic Era and to study their dynamics. Here we present a new, highly resolved, astronomically dated, continuous composite of benthic foraminifer isotope records developed in our laboratories. Four climate states – Hothouse, Warmhouse, Coolhouse, Icehouse – are identified based on their distinctive response to astronomical forcing depending on greenhouse gas levels and polar ice sheet volume. Statistical analysis of the non-linear behavior encoded in our record reveals the key role that polar ice volume plays in the predictability of Cenozoic climate dynamics.

One Sentence Summary:

During the last 66 million years Earth's climate system response to astronomical forcing was state-dependent.

Global changes in Earth's climate during the Cenozoic Era, the last 66 million years, have long been inferred from stable isotope data in carbonate shells of benthic foraminifers, which are single-celled amoeboid organisms that live on the seafloor. Carbon and oxygen isotope records from deep-sea benthic foraminifers are a proven, invaluable archive of long-term changes in Earth's carbon cycle, deep-sea temperature, and seawater composition driven by changes in ice volume (*1, 2*). In 1975, Shackleton and Kennett (*3*) produced one of the first deep-sea benthic foraminifer stable isotope records of the Cenozoic. Despite being of low temporal resolution it revealed that Earth's climate had transitioned from a warm state 60 to 40 million years ago (Ma) to a cool state 10 to 5 Ma. Over the last 45 years, many deep-sea benthic foraminifer stable isotope records of variable length and quality have been developed, resulting in a more detailed record of Cenozoic climate change. Compilations of these deep-sea isotope records provide a compelling chronicle of past trends, cyclic variations, and transient events in the climate system from the Late Cretaceous to today (*1, 4-10*). However, even the most recent benthic isotope compilations cannot accurately document the full range and detailed characteristics of Cenozoic climate variability on time scales of ten thousand to one million years. Age models and temporal resolution of Cenozoic benthic isotope compilations are either too coarse and/or include gaps, particularly prior to 34 Ma. These weaknesses hamper progress in determining the dynamics of the Cenozoic climate system (*4, 9, 11*), for example, because they prohibit application of advanced techniques of non-linear time series analysis at the required (astronomical) time-scales. The lack of highly-resolved, continuous, and accurately dated records constitutes a key limitation in our ability to identify and understand the characteristics of Earth's evolving climate during the Cenozoic.

Here, we present a new astronomically tuned deep-sea benthic foraminifer carbon $\delta^{13}C$ and oxygen $\delta^{18}O$ isotope reference record uniformly covering the entire Cenozoic, developed in our laboratories using sediment archives retrieved by scientific ocean drilling (Fig. 1). To produce this new composite record, we selected 14 ocean drilling records, checked and revised their composite splices where necessary, and preferentially selected records utilizing the genus *Cibicidoides* and *Nuttallides* to minimize systematic interspecies isotopic offsets (*1, 4, 12, 13*). We additionally generated new benthic stable isotope data spanning the late Miocene and middle-to-late Eocene to fill intervals inadequately covered by existing records. We collated existing astrochronologies for all records, recalibrated them to the La2010b orbital solution (*14*) if required, and developed a new astrochronology for the middle-to-late Eocene (*13*). We estimate our chronology to be accurate to ± 100-kyr for the Paleocene and Eocene, ± 50-kyr for the Oligocene to middle Miocene, and ± 10-kyr for the late Miocene to Pleistocene. The composite record is affected by some spatial bias arising from the uneven distribution of deep-sea stable isotope data that mainly derive from low- to mid-latitudes (*13*). Nevertheless, the resulting new **Ceno**zoic **G**lobal **R**eference benthic foraminifer carbon and oxygen **I**sotope **D**ataset (CENOGRID) provides a refined record with higher signal-to-noise ratio than any previous compilations ((*13*); text S1), and better coverage of the Paleocene, Eocene and late Miocene intervals (Fig. S32). The CENOGRID serves as an astronomically tuned high-definition stratigraphic reference of past global climate evolution for the past 66 million years.

On time scales of ten thousand to one million years, global climate is a complex, dynamical system responding non-linearly to quasi-periodic astronomical forcing. By combining the latest high-resolution generation of Cenozoic deep-sea isotope records on a highly accurate timescale, CENOGRID enables the definition of Earth's fundamental climates and investigation of the

predictability of their dynamics. We used recurrence analysis (RA) of the CENOGRID record (*13, 15*) to identify fundamental climate states that internally share characteristic and statistically distinctive dynamics. Recurrence is a major property of dynamical systems and RA provides information about non-linear dynamics, dynamical transitions, and even non-linear interrelationships (*15*), and facilitates evaluation of underlying dynamical processes – e.g., whether they are stochastic, regular, or chaotic. We present recurrence plots and their quantification of the benthic foraminifer $\delta^{13}C$ and $\delta^{18}O$ records to recognize different climate states and apply the RA measure of 'determinism' (DET) to quantify the predictability of Cenozoic climate dynamics.

Four distinctive climate states emerge as distinct blocks from our recurrence plots of the $\delta^{18}O$ CENOGRID record that we label Hothouse, Warmhouse, Coolhouse, and Icehouse state (Fig. 2). Block-like structures in the recurrence plots identify epochs where the dynamical system is 'trapped' in a particular state. This interpretation of Cenozoic climate history is broadly consistent with previous interpretations but our recurrence plot analysis of the highly resolved CENOGRID data provides a more statistically robust and objective exposition of events.

Detailed features of the four climate states can be inferred from the isotope profiles (Fig. 1) and scatter plots of the CENOGRID $\delta^{13}C$ and $\delta^{18}O$ data, and atmospheric CO_2 concentration estimates (Fig. 2; (*13)*). Warmhouse and Hothouse states prevailed from the Cretaceous/Paleogene boundary (K/Pg, 66 Ma) to the Eocene-Oligocene Transition (EOT, 34 Ma). During the Warmhouse, global temperatures were more than 5°C warmer than today (*13*) and benthic $\delta^{13}C$ and $\delta^{18}O$ show a persistent positive correlation with one another. The Hothouse operated between the Paleocene-Eocene Thermal Maximum at 56 Ma and the end of the Early Eocene Climate Optimum (EECO) at 47 Ma (*16*), when temperatures were more than 10°C

warmer than today and displayed greater amplitude variability. Transient warming events (hyperthermals) are an intrinsic feature of the Hothouse, wherein paired negative excursions in $\delta^{13}C$ and $\delta^{18}O$ reflect warming globally through rapid addition of carbon to the ocean-atmosphere system. The two Warmhouse phases from 66 to 56 Ma (Paleocene) and 47 to 34 Ma (middle-late Eocene) share a similar temperature range but have distinct background $\delta^{13}C$ isotope values and atmospheric CO_2 levels (Fig. 2, S35). At the EOT, the Warmhouse transitioned into the Coolhouse state, marked by a stepwise, significant drop in temperature and a major increase in continental ice volume with large ice-sheets appearing on Antarctica (*17*) to establish a unipolar glacial state (*18*). The recurrence plots mark out the EOT as the most prominent transition of the whole Cenozoic, which highlights the important role of ice sheets in modulating Earth's climate state (Fig. S33; (*13)*).

The Coolhouse state spans ~34 Ma (EOT) to 3.3 Ma (mid Pliocene M2 glacial), and is divided into two phases by the marked shift in $\delta^{18}O$ increase at 13.9 Ma related to the expansion of Antarctic ice sheets during the middle Miocene Climate Transition (mMCT; (*19)*). Warmer conditions culminating in the Miocene Climatic Optimum (MCO; ~17-14 Ma; (*20*)) characterize the first phase, followed by cooling and increasing $\delta^{18}O$ during the second phase (Fig 2). RA of carbon isotope data documents an additional major transition in the carbon cycle around 7 Ma related to end of the late Miocene Carbon Isotope Shift (*11, 21, 22*). A major change in the correlation between benthic foraminifer $\delta^{13}C$ and $\delta^{18}O$ occurs during the Pliocene epoch (*23*). The Icehouse climate state (Fig. 2), driven by the appearance of waxing and waning ice sheets in the northern hemisphere, was fully established by the Pliocene-Pleistocene transition (*24*) (Fig. 1, 2) with Marine Isotope Stage M2 at 3.3 Ma being a possible harbinger. The recurrence plots are less pronounced and more transparent from 3.3 Ma to today (Fig. 2, S34), suggesting that

Earth's climate-cryosphere dynamics entered a state not comparable to anything seen in the preceding 60 or more million years.

The CENOGRID allows us to scrutinize the state-dependency of climate system response to CO_2 and astronomical forcing on ten thousand to one million year time scales (*13*). Astronomical forcing throughout the Cenozoic is consistently uniform, but the RA indicates that the non-linear response in climate variability to this forcing is strongly influenced by the fundamental state of climate. Evolutionary spectrograms characterize the dominant climatic response to astronomical forcing during the Cenozoic (Fig. 3). We find that the prevailing climate state as characterized by atmospheric CO_2 concentration and polar ice sheets seems to orchestrate the response and impact of climate processes to astronomical forcing. Modeled insolation-driven global temperature variability on astronomical time scales suggest that different temperature response regimes exist: eccentricity dominates temperature responses in low latitudes, precession in mid latitudes and obliquity in high latitudes (*25*). Thus, pronounced astronomical cyclicity in the CENOGRID could reflect climate-state dependent amplifications of latitude-specific climate processes.

In the Hothouse and Warmhouse, as well as the first Coolhouse phase, eccentricity-related cycles dominate the CENOGRID indicating a strong influence of low-latitude processes on climate variations. Obliquity-related cycles are sparse in these intervals, but have been documented in other geochemical records (*26, 27*) exhibiting perhaps local lithological responses. Weak response in the obliquity-band during the Hothouse and Warmhouse intervals might be related to the absence of a high-latitude ice sheet that could have amplified climate response to obliquity forcing. The driving mechanism for the prevailing eccentricity cyclicity in the benthic $\delta^{13}C$ and $\delta^{18}O$ records is still unknown, but modeling suggests that low- and mid-latitude processes in the climate system respond in a non-linear way to insolation forcing (*25*, *28-30*). In this regard, a key

feedback likely involves the hydrological cycle with highly seasonal precipitation patterns during intervals of strong monsoon response to precession-induced insolation change which could play a major role in the global distribution of moisture and energy (*31-34*). The expression of precession is apparently weak in the CENOGRID composite record despite the dominant eccentricity forcing, likely due to the long residence time of carbon in the oceans enhancing longer forcing periods (*30, 35*), as well as our strategy to avoid 'overtuning' the record. Following the increasing influence of high latitude cooling and ice growth during the second Coolhouse phase, the obliquity-band response steadily increases after the mMCT before dominating climate dynamics by the late Miocene-early Pliocene (*11, 22, 36*). In the Icehouse state, the progressive decrease in atmospheric CO_2 and major growth of polar ice sheets, which enhanced variability in $\delta^{18}O$, steadily amplified the influence of complex high latitude feedbacks until they essentially dominate climate dynamics.

To better understand the complexity of climate dynamics recorded in the CENOGRID, we computed the RA measure of determinism (DET, (*13)*). This parameter quantifies the predictability of dynamics in a system's state. Predictability estimates the stochastic (unpredictable) versus the deterministic (predictable) nature of climate dynamics recorded in CENOGRID (*13*). DET values near zero correspond to unpredictable dynamics, whereas large values indicate predictable dynamics, which are especially interesting to examine on the approach to tipping points. Changes in DET can thus reveal transitions between fundamentally different climate regimes.

Our RA suggests that climate dynamics during the Warmhouse and Hothouse Cenozoic states are more predictable or more regular than those of the Coolhouse and Icehouse states (Fig. 3). The growth of polar ice sheets at the EOT enhanced the effect of obliquity pacing of high

latitude climate that interacted with eccentricity-modulated precession forcing at lower latitudes from that point in time. This led to increased non-linear interactions among astronomically paced climate processes, and thus more complex, stochastic climate dynamics. The development of large Antarctic ice volume at the inception of the Coolhouse is associated with a fundamental regime change towards less predictable climate variability (lower DET values calculated from benthic $\delta^{18}O$, Fig. 3). From 25 to 13.9 Ma DET is elevated again, related to a reduction in ice volume in relatively warmer times of the Coolhouse, culminating in the MCO. Despite the growing influence of ice sheets in the Coolhouse, until ~6 to 7 Ma carbon cycle dynamics remain more deterministic than temperature because $\delta^{13}C$ variations are predominantly driven by low-latitude processes and less strongly influenced by the complex interaction with polar ice-sheet fluctuations. After ~6 Ma DET drops likely due to stronger cryosphere imprint on the carbon cycle. Upon initiation of the Icehouse at 3.3 Ma, $\delta^{18}O$ recorded climate dynamics become slightly more deterministic (*37*) and carbon cycle dynamics unpredictable, likely resulting from the complex response to the waxing and waning of polar caps (*38*).

The CENOGRID spectrogram displays a broader frequency range during several intervals with low DET values (e.g., Coolhouse), while high DET values (e.g., Warmhouse) occur when single frequencies dominate (Fig. 3). This could be signaling a more direct response to astronomical forcing in the Warmhouse compared to the Coolhouse. Our RA suggests that the Hothouse is more stochastic (less predictable) than the Warmhouse, presumably induced by the occurrence of extreme hyperthermal events and their strong non-linear and much amplified climate response to astronomical forcing (*39, 40*). The evolving pattern in the DET from the onset of cooling after the EECO to the EOT is striking (Fig. 3). The amplitude in fluctuations between stochastic and deterministic dynamics intensifies from 49 Ma to 34 Ma, consistent with how Earth's climate

system is suggested to behave (*41, 42*) as it moves towards a major tipping point. Once that tipping point is reached at the EOT, a rapid shift toward more permanently stochastic dynamics marks the inception of a new climate state (*43*). Thus polar ice volume is not only critical to defining Earth's fundamental climate state, it also seems to play a critical role in determining the predictability of its climatological response to astronomical forcing.

References and Notes:

1. J. Zachos, M. Pagani, L. Sloan, E. Thomas, K. Billups, Trends, Rhythms, and Aberrations in Global Climate 65 Ma to Present. *Science* **292**, 686-693 (2001).
2. K. G. Miller, G. Mountain, J. D. Wright, J. V. Browning, A 180-Million-Year Record of Sea Level and Ice Volume Variations from Continental Margin and Deep-Sea Isotopic Records. *Oceanography* **24**, 40-53 (2011).
3. N. J. Shackleton, J. P. Kennett, in *Init. Repts. DSDP , 29: Washington (U.S. Govt. Printing Office),* J. P. Kennett, R. E. Houtz, et al., Eds. (1975), pp. 743-755.
4. B. S. Cramer, J. R. Toggweiler, J. D. Wright, M. E. Katz, K. G. Miller, Ocean overturning since the Late Cretaceous: Inferences from a new benthic foraminiferal isotope compilation. *Paleoceanography* **24**, (2009).
5. D. De Vleeschouwer, M. Vahlenkamp, M. Crucifix, H. Pälike, Alternating Southern and Northern Hemisphere climate response to astronomical forcing during the past 35 m.y. *Geology* **45**, 375-378 (2017).
6. O. Friedrich, R. D. Norris, J. Erbacher, Evolution of middle to Late Cretaceous oceans – A 55 m.y. record of Earth's temperature and carbon cycle. *Geology* **40**, 107-110 (2012).
7. K. G. Miller, R. G. Fairbanks, G. S. Mountain, Tertiary oxygen isotope synthesis, sea level history, and continental margin erosion. *Paleoceanography* **2**, 1-19 (1987).
8. J. Veizer, A. Prokoph, Temperatures and oxygen isotopic composition of Phanerozoic oceans. *Earth-Science Reviews* **146**, 92-104 (2015).
9. J. C. Zachos, G. R. Dickens, R. E. Zeebe, An early Cenozoic perspective on greenhouse warming and carbon-cycle dynamics. *Nature* **451**, 279-283 (2008).
10. K. G. Miller et al., Cenozoic sea-level and cryospheric evolution from deep-sea geochemical and continental margin records. *Science Advances* **6,** no. 20, (2020).
11. A. J. Drury, T. Westerhold, D. Hodell, U. Röhl, Reinforcing the North Atlantic backbone: revision and extension of the composite splice at ODP Site 982. *Clim. Past* **14**, 321-338 (2018).
12. M. E. Katz *et al.*, Early Cenozoic benthic foraminiferal isotopes: Species reliability and interspecies correction factors. *Paleoceanography* **18**, 10.1029/2002PA000798 (2003).
13. See supplementary materials.
14. J. Laskar, A. Fienga, M. Gastineau, H. Manche, La2010: a new orbital solution for the long-term motion of the Earth. *Astronomy and Astrophysics* **532**, 15 (2011).
15. N. Marwan, M. C. Romano, M. Thiel, J. Kurths, Recurrence plots for the analysis of complex systems. *Physics Reports* **438**, 237-329 (2007).
16. T. Westerhold, U. Röhl, B. Donner, J. C. Zachos, Global Extent of Early Eocene Hyperthermal Events: A New Pacific Benthic Foraminiferal Isotope Record From Shatsky Rise (ODP Site 1209). *Paleoceanography and Paleoclimatology* **33**, 626-642 (2018).
17. H. K. Coxall, P. A. Wilson, H. Pälike, C. H. Lear, J. Backman, Rapid stepwise onset of Antarctic glaciation and deeper calcite compensation in the Pacific Ocean. *Nature* **433**, 53-57 (2005).
18. J. F. Spray *et al.*, North Atlantic Evidence for a Unipolar Icehouse Climate State at the Eocene-Oligocene Transition. *Paleoceanography and Paleoclimatology* **34**, 1124-1138 (2019).

19. B. P. Flower, J. P. Kennett, The middle Miocene climatic transition: East Antarctic ice sheet development, deep ocean circulation and global carbon cycling. *Pal. Pal. Pal.*, **108**, 537-555 (1994).
20. A. E. Holbourn, W. Kuhnt, K. G. D. Kochhann, N. Andersen, K. J. S. Meier, Global perturbation of the carbon cycle at the onset of the Miocene Climatic Optimum. *Geology* **43**, 123-126 (2015).
21. D. A. Hodell, K. A. Venz-Curtis, Late Neogene history of deepwater ventilation in the Southern Ocean. *Geochemistry, Geophysics, Geosystems* **7**, (2006).
22. A. J. Drury *et al.*, Late Miocene climate and time scale reconciliation: Accurate orbital calibration from a deep-sea perspective. *Earth and Planetary Science Letters* **475**, 254-266 (2017).
23. S. Kirtland Turner, Pliocene switch in orbital-scale carbon cycle/climate dynamics. *Paleoceanography* **29**, 1256-1266 (2014).
24. I. Bailey *et al.*, An alternative suggestion for the Pliocene onset of major northern hemisphere glaciation based on the geochemical provenance of North Atlantic Ocean ice-rafted debris. *Quaternary Science Reviews* **75**, 181-194 (2013).
25. T. Laepple, G. Lohmann, Seasonal cycle as template for climate variability on astronomical timescales. *Paleoceanography* **24**, (2009).
26. T. Westerhold, U. Röhl, High resolution cyclostratigraphy of the early Eocene - new insights into the origin of the Cenozoic cooling trend. *Climate of the Past* **5**, 309-327 (2009).
27. M. Vahlenkamp et al., Astronomically paced changes in deep-water circulation in the western North Atlantic during the middle Eocene. *Earth and Planetary Science Letters* **484**, 329-340 (2018).
28. T. J. Crowley, K.-Y. Kim, J. G. Mengel, D. A. Short, Modeling 100,000 year climate fluctuations in pre-Pleistocene time series. *Science* **255**, 705-707 (1992).
29. D. A. Short, J. G. Mengel, T. J. Crowley, W. T. Hyde, G. R. North, Filtering of Milankovitch Cycles by Earth's Geography. *Quaternary Research* **35**, 157-173 (1991).
30. R. E. Zeebe, T. Westerhold, K. Littler, J. C. Zachos, Orbital forcing of the Paleocene and Eocene carbon cycle. *Paleoceanography* **32**, 440-465 (2017).
31. K. E. Trenberth, D. P. Stepaniak, J. M. Caron, The Global Monsoon as Seen through the Divergent Atmospheric Circulation. *Journal of Climate* **13**, 3969-3993 (2000).
32. P. X. Wang *et al.*, The global monsoon across time scales: Mechanisms and outstanding issues. *Earth-Science Reviews* **174**, 84-121 (2017).
33. M. Huber, A. Goldner, Eocene monsoons. *Journal of Asian Earth Sciences* **44**, 3-23 (2012).
34. J. H. C. Bosmans, S. S. Drijfhout, E. Tuenter, F. J. Hilgen, L. J. Lourens, Response of the North African summer monsoon to precession and obliquity forcings in the EC-Earth GCM. *Climate Dynamics* **44**, 279-297 (2015).
35. H. Pälike *et al.*, The Heartbeat of the Oligocene Climate System. *Science* **314**, 1894-1898 (2006).
36. A. E. Holbourn, W. Kuhnt, S. Clemens, W. Prell, N. Andersen, Middle to late Miocene stepwise climate cooling: Evidence from a high-resolution deep water isotope curve spanning 8 million years. *Paleoceanography* **28**, 2013PA002538 (2013).
37. S. R. Meyers, L. A. Hinnov, Northern Hemisphere glaciation and the evolution of Plio-Pleistocene climate noise. *Paleoceanography* **25**, PA3207 (2010).

38. D. Liebrand, A. T. M. de Bakker, Bispectra of climate cycles show how ice ages are fuelled. *Clim. Past* **15**, 1959-1983 (2019).
39. S. Kirtland Turner, P. F. Sexton, C. D. Charles, R. D. Norris, Persistence of carbon release events through the peak of early Eocene global warmth. *Nature Geoscience* **7**, (2014).
40. D. J. Lunt et al., A model for orbital pacing of methane hydrate destabilization during the Palaeogene. *Nature Geosci* **4**, 775-778 (2011).
41. V. Dakos *et al.*, Slowing down as an early warning signal for abrupt climate change. *Proceedings of the National Academy of Sciences* **105**, 14308-14312 (2008).
42. M. Scheffer *et al.*, Early-warning signals for critical transitions. *Nature* **461**, 53-59 (2009).
43. W. Steffen *et al.*, Trajectories of the Earth System in the Anthropocene. *Proceedings of the National Academy of Sciences*, (2018).
44. M. D. Palmer, G. R. Harris, J. M. Gregory, Extending CMIP5 projections of global mean temperature change and sea level rise due to thermal expansion using a physically-based emulator. *Environmental Research Letters* **13**, 084003 (2018).

Supplementary References

45. J. C. Zachos, D. Kroon, P. Blum, et al., *Proc. ODP, Init. Repts., 208: College Station, TX (Ocean Drilling Program)*. (2004).
46. T. B. Coplen, Editorial: More uncertainty than necessary. *Paleoceanography* **11**, 369-370 (1996).
47. T. Westerhold, U. Röhl, T. Frederichs, S. M. Bohaty, J. C. Zachos, Astronomical calibration of the geological timescale: closing the middle Eocene gap. *Clim. Past* **11**, 1181-1195 (2015).
48. T. Westerhold et al., Late Lutetian Thermal Maximum—Crossing a Thermal Threshold in Earth's Climate System? *Geochemistry, Geophysics, Geosystems* **19**, 73-82 (2018).
49. S. J. Langton, N. M. Rabideaux, C. Borrelli, M. E. Katz, Southeastern Atlantic deep-water evolution during the late-middle Eocene to earliest Oligocene (Ocean Drilling Program Site 1263 and Deep Sea Drilling Project Site 366). *Geosphere* **12**, 1032-1047 (2016).
50. C. R. Riesselmann, R. B. Dunbar, D. A. Mucciarone, S. S. Kitasei, "High resolution stable isotope and carbonate variability during the early Oligocene climate transition: Walvis Ridge (ODP Site 1263)," *Open-File Report* (Reston, VA, 2007).
51. D. B. Bell, S. J. A. Jung, D. Kroon, L. J. Lourens, D. A. Hodell, Local and regional trends in Plio-Pleistocene d18O records from benthic foraminifera. **15**, 3304-3321 (2014).
52. T. Westerhold *et al.*, Astronomical calibration of the Ypresian timescale: implications for seafloor spreading rates and the chaotic behavior of the solar system? *Clim. Past* **13**, 1129-1152 (2017).
53. W. F. Ruddiman, D. Cameron, B. M. Clement, in *Init. Repts. DSDP, 94: Washington (U.S. Govt. Printing Office),* W. F. Ruddiman, R. B. Kidd, E. Thomas, et al., Eds. (1987), pp. 615-634.
54. R. Wilkens *et al.*, Revisiting the Ceara Rise, equatorial Atlantic Ocean: isotope stratigraphy of ODP Leg 154 from 0 to 5 Ma. *Clim Past* **13**, 799-793 (2017).

55. J. L. Kirschvink, The least-squares line and plane and the analysis of paleomagnetic data. *Geophys. J. Roy. Astron. Soc.* **62**, 699-718 (1980).
56. A. Stephenson, Gyromagnetism and the remanence acquired by a rotating rock in an alternating field. *Nature* **284**, 48-49 (1980).
57. A. Stephenson, Gyroremanent magnetization in a weakly anisotropic rock sample. *Physics of the Earth and Planetary Interiors* **25**, 163-166 (1981).
58. J. D. A. Zijderveld, in *Methods in Paleomagnetism,* D. W. Collinson, K. M. Creer, S. K. Runcorn, Eds. (Elsevier, Amsterdam, 1967), pp. 254-286.
59. P. C. Lurcock, F. Florindo, New developments in the PuffinPlot paleomagnetic data analysis program. *Geochemistry, Geophysics, Geosystems* **20**, (2019).
60. J. G. Ogg, in *The Geologic Time Scale,* F. M. Gradstein, J. G. Ogg, M. D. Schmitz, G. M. Ogg, Eds. (Elsevier, Boston, 2012), pp. 85-113.
61. F. J. Hilgen *et al.*, in *The Geologic Time Scale,* F. M. Gradstein, J. G. Ogg, M. D. Schmitz, G. M. Ogg, Eds. (Elsevier, Boston, 2012), pp. 923-978.
62. N. Vandenberghe *et al.*, in *The Geologic Time Scale,* F. M. Gradstein, J. G. Ogg, M. D. Schmitz, G. M. Ogg, Eds. (Elsevier, Boston, 2012), pp. 855-921.
63. S. Galeotti *et al.*, Cyclochronology of the Early Eocene carbon isotope record from a composite Contessa Road-Bottaccione section (Gubbio, central Italy). *Lethaia* **50**, 231-244 (2017).
64. S. C. Cande, D. V. Kent, A New Geomagnetic Polarity Time Scale for the late Cretaceous and Cenozoic. *Journal of Geophysical Research* **97**, 13,917-913,951 (1992).
65. S. C. Cande, D. V. Kent, Revised calibration of the geomagnetic polarity timescale for the Late Cretaceous and Cenozoic. *Journal of Geophysical Research* **100**, 6093-6095 (1995).
66. L. A. Hinnov, F. J. Hilgen, in *The Geologic Time Scale,* F. M. Gradstein, J. G. Ogg, M. D. Schmitz, G. M. Ogg, Eds. (Elsevier, Boston, 2012), pp. 63-83.
67. A. E. Holbourn et al., Late Miocene climate cooling and intensification of southeast Asian winter monsoon. *Nature Communications* **9**, 1584 (2018).
68. A. E. Holbourn et al., Middle Miocene climate cooling linked to intensification of eastern equatorial Pacific upwelling. *Geology* **42**, 19-22 (2014).
69. J. Laskar *et al.*, A long-term numerical solution for the insolation quantities of the Earth. *Astronomy and Astrophysics* **428**, 261-285 (2004).
70. K. Littler *et al.*, Astronomical Time Keeping of Earth History: An Invaluable Contribution of Scientific Ocean Drilling. *Oceanography* **32**, 72-76 (2019).
71. I. J. Kocken, M. J. Cramwinckel, R. E. Zeebe, J. J. Middelburg, A. Sluijs, The 405 kyr and 2.4 Myr eccentricity components in Cenozoic carbon isotope records. *Clim. Past* **15**, 91-104 (2019).
72. J. Laskar, in *Phil. Trans. R. Soc. Lond. A,* N. J. Shackleton, I. N. McCave, G. P. Weedon, Eds. (1999), vol. 357, pp. 1735-1759.
73. L. J. Lourens, F. J. Hilgen, J. Laskar, N. J. Shackleton, D. Wilson, in *A Geological Timescale 2004,* F. Gradstein, J. Ogg, A. Smith, Eds. (Cambridge University Press, Cambridge University Press, UK, 2004), pp. 409-440.
74. C. Zeeden, F. J. Hilgen, S. K. Hüsing, L. L. Lourens, The Miocene astronomical time scale 9–12 Ma: New constraints on tidal dissipation and their implications for paleoclimatic investigations. *Paleoceanography* **29**, 2014PA002615 (2014).

75. R. E. Zeebe, L. J. Lourens, Solar System chaos and the Paleocene–Eocene boundary age constrained by geology and astronomy. *Science* **365**, 926-929 (2019).
76. T. Westerhold, U. Röhl, J. Laskar, Time scale controversy: Accurate orbital calibration of the early Paleogene. *Geochem. Geophys. Geosyst.* **13**, Q06015 (2012).
77. J. S. K. Barnet *et al.*, A new high-resolution chronology for the late Maastrichtian warming event: Establishing robust temporal links with the onset of Deccan volcanism. *Geology* **46**, 147-150 (2017).
78. B. S. Cramer, J. D. Wright, D. V. Kent, M.-P. Aubry, Orbital climate forcing of d13C excursions in the late Paleocene - Eocene (chrons C24n-C25n). *Paleoceanography* **18**, 1097 (2003).
79. J. C. Zachos, H. McCarren, B. Murphy, U. Röhl, T. Westerhold, Tempo and scale of late Paleocene and early Eocene carbon isotope cycles: Implications for the origin of hyperthermals. *Earth and Planetary Science Letters* **299**, 242-249 (2010).
80. J. Laurin, B. Růžek, M. Giorgioni, Orbital Signals in Carbon Isotopes: Phase Distortion as a Signature of the Carbon Cycle. *Paleoceanography* **32**, 1236-1255 (2017).
81. N. J. Shackleton, M. A. Hall, A. Boersma, in *Initial Reports Deep Sea Drilling Project, vol. 74. US Governmental Printing Office, Washington,* T. C. Moore, P. D. Rabinowitz, Eds. (1984), pp. 599–613.
82. C. H. Lear, H. Elderfield, P. A. Wilson, Cenozoic Deep-Sea Temperatures and Global Ice Volumes from Mg/Ca in Benthic Foraminiferal Calcite. *Science* **287**, 269-272 (2000).
83. G. W. Brass, J. R. Southam, W. H. Peterson, Warm saline bottom water in the ancient ocean. *Nature* **296**, 620-623 (1982).
84. M. Huber, L. C. Sloan, Heat transport, deep waters, and thermal gradients: Coupled simulation of an Eocene greenhouse climate. *Geophysical Research Letters* **28**, 3481-3484 (2001).
85. K. L. Bice, J. Marotzke, Numerical evidence against reversed thermohaline circulation in the warm Paleocene/Eocene ocean. *Journal of Geophysical Research* **106**, 11,529-511,542 (2001).
86. M. Huber, R. Caballero, The early Eocene equable climate problem revisited. *Clim. Past* **7**, 603-633 (2011).
87. P. N. Pearson et al., Stable warm tropical climate through the Eocene Epoch. *Geology* **35**, 211-214 (2007).
88. J. S. K. Barnet et al., A High-Fidelity Benthic Stable Isotope Record of Late Cretaceous–Early Eocene Climate Change and Carbon-Cycling. *Paleoceanography and Paleoclimatology* **34**, 672-691 (2019).
89. J. P. Eckmann, S. O. Kamphorst, D. Ruelle, Recurrence Plots of Dynamical Systems. *Europhysics Letters (EPL)* **4**, 973-977 (1987).
90. K. H. Krämer, R. Donner, J. Heitzig, N. Marwan, Recurrence threshold selection for obtaining robust recurrence characteristics in different embedding dimensions. *Chaos* **28**, (2018).
91. N. Marwan, S. Schinkel, J. Kurths, Recurrence plots 25 years later - Gaining confidence in dynamical transitions. *EPL (Europhysics Letters)* **101**, 20007 (2013).
92. J. Hansen, M. Sato, G. Russell, P. Kharecha, Climate sensitivity, sea level and atmospheric carbon dioxide. *Philosophical Transactions of the Royal Society A: Mathematical, Physical and Engineering Sciences* **371**, 20120294 (2013).

93. J. Oerlemans, Correcting the Cenozoic $\delta^{18}O$ deep-sea temperature record for Antarctic ice volume. *Palaeogeography, Palaeoclimatology, Palaeoecology* **208**, 195-205 (2004).
94. G. L. Foster, D. L. Royer, D. J. Lunt, Future climate forcing potentially without precedent in the last 420 million years. *Nature Communications* **8**, 14845 (2017).
95. S. Ji *et al.*, A symmetrical CO2 peak and asymmetrical climate change during the middle Miocene. *Earth and Planetary Science Letters* **499**, 134-144 (2018).
96. T. B. Chalk *et al.*, Causes of ice age intensification across the Mid-Pleistocene Transition. *Proceedings of the National Academy of Sciences* **114**, 13114-13119 (2017).
97. R. Greenop *et al.*, Orbital Forcing, Ice Volume, and CO2 Across the Oligocene-Miocene Transition. *Paleoceanography and Paleoclimatology* **34**, 316-328 (2019).
98. L. Londoño *et al.*, Early Miocene CO_2 estimates from a Neotropical fossil leaf assemblage exceed 400 ppm. *American Journal of Botany* **105**, 1929-1937 (2018).
99. S. M. Sosdian *et al.*, Constraining the evolution of Neogene ocean carbonate chemistry using the boron isotope pH proxy. *Earth and Planetary Science Letters* **498**, 362-376 (2018).
100. M. Steinthorsdottir, V. Vajda, M. Pole, G. Holdgate, Moderate levels of Eocene pCO_2 indicated by Southern Hemisphere fossil plant stomata. *Geology*, (2019).
101. J. R. Super *et al.*, North Atlantic temperature and pCO_2 coupling in the early-middle Miocene. *Geology* **46**, 519-522 (2018).
102. G. E. A. Swann, C. P. Kendrick, A. J. Dickson, S. Worne, Late Pliocene Marine pCO_2 Reconstructions From the Subarctic Pacific Ocean. *Paleoceanography and Paleoclimatology* **33**, 457-469 (2018).
103. C. R. Witkowski, J. W. H. Weijers, B. Blais, S. Schouten, J. S. Sinninghe Damsté, Molecular fossils from phytoplankton reveal secular pCO_2 trend over the Phanerozoic. *Science Advances* **4**, eaat4556 (2018).
104. A. P. Wolfe *et al.*, Middle Eocene CO_2 and climate reconstructed from the sediment fill of a subarctic kimberlite maar. *Geology* **45**, 619-622 (2017).
105. J. C. G. Walker, P. B. Hays, J. K. Kasting, A negative feedback mechanism for the long term stabilization of Earth´s surface temperature. *Journal of Geophysical Research* **86**, 9776-9782 (1981).
106. R. A. Berner, A model of atmospheric CO_2 over Phanerozoic time. *American Journal of Science* **291**, 339-376 (1991).
107. A. Holbourn, W. Kuhnt, M. Schulz, H. Erlenkeuser, Impacts of orbital forcing and atmospheric carbon dioxide on Miocene ice-sheet expansion. *Nature* **438**, 483-487 (2005).
108. S. C. Woodard et al., Antarctic role in Northern Hemisphere glaciation. *Science* **346**, 847-851 (2014).
109. M. R. Saltzman, E. Thomas, in *The Geologic Time Scale,* F. M. Gradstein, J. G. Ogg, M. D. Schmitz, G. M. Ogg, Eds. (Elsevier, Boston, 2012), pp. 207-232.
110. J. C. Zachos, M. A. Arthur, W. E. Dean, Geochemical Evidence for Suppression of Pelagic Marine Productivity at the Cretaceous/Tertiary Boundary. *Nature* **337**, 61-64 (1989).
111. A. K. Hilting, L. R. Kump, T. J. Bralower, Variations in the oceanic vertical carbon isotope gradient and their implications for the Paleocene-Eocene biological pump. *Paleoceanography* **23**, (2008).

112. A. C. Kurtz, L. R. Kump, M. A. Arthur, J. C. Zachos, A. Paytan, Early Cenozoic decoupling of the global carbon and sulfur cycles. *Paleoceanography* **18**, 1090, (2003).
113. E. Vincent, W. H. Berger, in *The carbon cycle and atmospheric CO_2: Natural variations Archean to Present.,* E. T. Sundquist, W. S. Broecker, Eds. (AGU, Washington D. C., 1985), pp. 455-468.
114. A. J. Drury, C. e. d. M. John, A. E. Shevenell, Evaluating climatic response to external radiative forcing during the late Miocene to early Pliocene: New perspectives from eastern equatorial Pacific (IODP U1338) and North Atlantic (ODP 982) locations. *Paleoceanography* **31**, 167-184 (2016).
115. L. J. Lourens *et al.*, Astronomical pacing of late Palaeocene to early Eocene global warming events. *Nature* **435**, 1083-1087 (2005).
116. B. S. Slotnick *et al.*, Large-Amplitude Variations in Carbon Cycling and Terrestrial Weathering during the Latest Paleocene and Earliest Eocene: The Record at Mead Stream, New Zealand. *The Journal of Geology* **120**, 487-505 (2012).
117. G. R. Dickens, Rethinking the global carbon cycle with a large, dynamic and microbially mediated gas hydrate capacitor. *Earth and Planetary Science Letters* **213**, 169-183 (2003).
118. D. L. Royer, CO_2-forced climate thresholds during the Phanerozoic. *Geochimica et Cosmochimica Acta* **70**, 5665-5675 (2006).
119. J. D. Hays, J. Imbrie, N. J. Shackleton, Variations in the Earth's Orbit: pacemaker of the Ice Ages. *Science* **194**, 1121-1132 (1976).
120. D. Liebrand et al., Cyclostratigraphy and eccentricity tuning of the early Oligocene through early Miocene (30.1–17.1 Ma): Cibicides mundulus stable oxygen and carbon isotope records from Walvis Ridge Site 1264. *Earth and Planetary Science Letters* **450**, 392-405 (2016).
121. H. M. Beddow, D. Liebrand, A. Sluijs, B. S. Wade, L. J. Lourens, Global change across the Oligocene-Miocene transition: High-resolution stable isotope records from IODP Site U1334 (equatorial Pacific Ocean). *Paleoceanography* **31**, 81-97 (2016).
122. D. J. Thomson, Spectrum estimation and harmonic analysis. *Proceedings of the IEEE* **70**, 1055-1096 (1982).
123. K. Billups, H. Palike, J. E. T. Channell, J. C. Zachos, N. J. Shackleton, Astronomic calibration of the late Oligocene through early Miocene geomagnetic polarity time scale. *Earth and Planetary Science Letters* **224**, 33-44 (2004).
124. N. J. Shackleton, S. J. Crowhurst, G. P. Weedon, J. Laskar, in *Phil. Trans. R. Soc. Lond. A*, N. J. Shackleton, I. N. McCave, G. P. Weedon, Eds. (1999), vol. **357**, pp. 1907-1929.
125. G. P. Weedon, N. J. Shackleton, P. N. Pearson, in *Proc. ODP, Sci. Results*, **154**: College Station, TX (Ocean Drilling Program), N. J. Shackleton, W. B. Curry, C. Richter, T. J. Bralower, Eds. (1997), pp. 101-114.
126. H. Pälike, J. Frazier, J. C. Zachos, Extended orbitally forced palaeoclimatic records from the equatorial Atlantic Ceara Rise. *Quaternary Science Reviews* **25**, 3138-3149 (2006).
127. J. Zachos, N. J. Shackleton, J. S. Revenaugh, H. Pälike, B. P. Flower, Climate Response to Orbital Forcing Across the Oligocene-Miocene Boundary. *Science* **292**, 274-278 (2001).
128. J. C. Zachos, B. P. Flower, H. Paul, Orbitally paced climate oscillations across the Oligocene/Miocene boundary. *Nature* **388**, 567-570 (1997).

129. IPCC, *Climate Change 2013: The Physical Science Basis. Contribution of Working Group I to the Fifth Assessment Report of the Intergovernmental Panel on Climate Change*. T. F. Stocker *et al.*, Eds., (Cambridge University Press, Cambridge United Kingdom and New York, NY, USA, 2013).
130. C. J. Hollis *et al.*, The DeepMIP contribution to PMIP4: methodologies for selection, compilation and analysis of latest Paleocene and early Eocene climate proxy data, incorporating version 0.1 of the DeepMIP database. *Geosci. Model Dev.* **12**, 3149-3206 (2019).
131. E. Anagnostou et al., Changing atmospheric CO_2 concentration was the primary driver of early Cenozoic climate. *Nature* **533**, 380-384 (2016).
132. P. N. Pearson, M. R. Palmer, Atmospheric carbon dioxide concentrations over the past 60 million years. *Nature* **406**, 695-699 (2000).
133. Y. G. Zhang, M. Pagani, Z. Liu, S. M. Bohaty, R. Deconto, A 40-million-year history of atmospheric CO_2. *Philos Trans A Math Phys Eng Sci* **371**, 20130096 (2013).
134. K. D. Burke *et al.*, Pliocene and Eocene provide best analogs for near-future climates. *Proceedings of the National Academy of Sciences*, 201809600 (2018).
135. E. Gasson, R. M. DeConto, D. Pollard, R. H. Levy, Dynamic Antarctic ice sheet during the early to mid-Miocene. *Proceedings of the National Academy of Sciences* **113**, 3459-3464 (2016).
136. M. A. Kominz *et al.*, Late Cretaceous to Miocene sea-level estimates from the New Jersey and Delaware coastal plain coreholes: an error analysis. *Basin Research* **20**, 211-226 (2008).
137. K. G. Miller, J. D. Wright, J. V. Browning, Visions of ice sheets in a greenhouse world. *Marine Geology* **217**, 215-231 (2005).
138. A. E. Shevenell, J. P. Kennett, D. W. Lea, Middle Miocene ice sheet dynamics, deep-sea temperatures, and carbon cycling: A Southern Ocean perspective. *Geochemistry, Geophysics, Geosystems* **9**, (2008).
139. M. Meinshausen *et al.*, The RCP greenhouse gas concentrations and their extensions from 1765 to 2300. *Climatic Change* **109**, 213-241 (2011).
140. R. M. DeConto, D. Pollard, Rapid Cenozoic glaciation of Antarctica induced by declining atmospheric CO2. *Nature* **421**, 245-249 (2003).
141. G. Doria *et al.*, Declining atmospheric CO_2 during the late Middle Eocene climate transition. *American Journal of Science* **311**, 63-75 (2011).
142. P. N. Pearson, Oxygen Isotopes in Foraminifera: Overview and Historical Review. *The Paleontological Society Papers* **18**, 1-38 (2012).
143. J. Bloch-Johnson, R. T. Pierrehumbert, D. S. Abbot, Feedback temperature dependence determines the risk of high warming. *Geophysical Research Letters* **42**, 4973-4980 (2015).
144. R. Caballero, M. Huber, State-dependent climate sensitivity in past warm climates and its implications for future climate projections. *Proceedings of the National Academy of Sciences* **110**, 14162-14167 (2013).
145. C. F. Dawber, A. K. Tripati, Exploring the controls on element ratios in middle Eocene samples of the benthic foraminifera Oridorsalis umbonatus. *Clim. Past* **8**, 1957-1971 (2012).

146. C. F. Dawber, A. K. Tripati, A. S. Gale, C. MacNiocaill, S. P. Hesselbo, Glacioeustasy during the middle Eocene? Insights from the stratigraphy of the Hampshire Basin, UK. *Palaeogeography, Palaeoclimatology, Palaeoecology* **300**, 84-100 (2011).
147. A. Dutton, K. C. Lohmann, R. M. Leckie, Insights from the Paleocene tropical Pacific: Foraminiferal stable isotope and elemental results from Site 1209, Shatsky Rise. *Paleoceanography* **20**, (2005).
148. S. R. Meyers. (2014). Astrochron: An R Package for Astrochronology, available at: https://CRAN.R-project.org/package=astrochron
149. C. Torrence, G. P. Compo, A Practical Guide to Wavelet Analysis. *Bulletin of the American Meteorological Society* **79**, 61-78 (1998).
150. A. Grinsted, J. C. Moore, S. Jevrejeva, Application of the cross wavelet transform and wavelet coherence to geophysical time series. *Nonlin. Processes Geophys*. **11**, 561-566 (2004).
151. D. Paillard, L. Labeyrie, P. Yiou, Macintosh Program performs time-series analysis. *Eos, Transactions American Geophysical Union* **77**, 379-379 (1996).
152. M. Meinshausen *et al.*, Historical greenhouse gas concentrations for climate modelling (CMIP6). *Geosci. Model Dev.* **10**, 2057-2116 (2017).
153. C. P. Morice, J. J. Kennedy, N. A. Rayner, P. D. Jones, Quantifying uncertainties in global and regional temperature change using an ensemble of observational estimates: The HadCRUT4 data set. *Journal of Geophysical Research: Atmospheres* **117**, (2012).
154. C. N. Waters *et al.*, The Anthropocene is functionally and stratigraphically distinct from the Holocene. *Science* **351**, aad2622 (2016).
155. C. Zeeden *et al.*, Revised Miocene splice, astronomical tuning and calcareous plankton biochronology of ODP Site 926 between 5 and 14.4 Ma. *Palaeogeography, Palaeoclimatology, Palaeoecology* **369**, 430-451 (2013).
156. T. Westerhold *et al.*, Orbitally tuned timescale and astronomical forcing in the middle Eocene to early Oligocene. *Clim. Past* **10**, 955-973 (2014).
157. L. Rivero-Cuesta et al., Paleoenvironmental Changes at ODP Site 702 (South Atlantic): Anatomy of the Middle Eocene Climatic Optimum. *Paleoceanography and Paleoclimatology* **n/a**, (2019).
158. N. J. Shackleton, M. A. Hall, D. Pate, in Supplement to: Shackleton, NJ et al. (1995): Pliocene stable isotope stratigraphy of Site 864. In: Pisias, NG; Mayer, LA; Janecek, TR; Palmer-Julson, A; van Andel, TH (eds.), *Proceedings of the Ocean Drilling Program*, Scientific Results, College Station, TX (Ocean Drilling Program), **138**, 337-355, (1995).
159. T. Bickert, W. B. Curry, G. Wefer, in *Proc. ODP, Sci. Results, 154: College Station, TX (Ocean Drilling Program),* N. J. Shackelton, W. B. Curry, C. Richter, T. J. Bralower, Eds. (1997), pp. 239-254.
160. N. J. Shackleton, M. A. Hall, in Proc. ODP, Sci. Results, 154: College Station, TX (Ocean Drilling Program), N. J. Shackleton, W. B. Curry, C. Richter, T. J. Bralower, Eds. (1997), vol. **154**, pp. 367-373.
161. N. J. Shackleton, N. D. Opdyke, Oxygen isotope and palaeomagnetic stratigraphy of Equatorial Pacific core V28-238: Oxygen isotope temperatures and ice volumes on a 10^5 year and 10^6 year scale. *Quaternary Research* **3**, 39-55 (1973).
162. P. F. Sexton *et al.*, Eocene global warming events driven by ventilation of oceanic dissolved organic carbon. *Nature* **471**, 349-352 (2011).

163. K. Billups, A. C. Ravelo, J. C. Zachos, Early Pliocene deep water circulation in the western equatorial Atlantic: Implications for high-latitude climate change. *Paleoceanography* **13**, 84-95 (1998).
164. P. deMenocal, D. Archer, P. Leth, in *Proc. ODP, Sci. Results, 154: College Station, TX (Ocean Drilling Program),* N. J. Shackelton, W. B. Curry, C. Richter, T. J. Bralower, Eds. (1997), pp. 285-298.
165. S. O. Franz, R. Tiedemann. Stable isotope data of Hole 154-925C (Tab. A2) (PANGAEA, 2002). 10.1594/PANGAEA.67526.
166. J. Tian et al., Paleoceanography of the east equatorial Pacific over the past 16 Myr and Pacific–Atlantic comparison: High resolution benthic foraminiferal $\delta^{18}O$ and $\delta^{13}C$ records at IODP Site U1337. *Earth and Planetary Science Letters* **499**, 185-196 (2018).
167. R. Tiedemann, S. O. Franz, in *Proc. ODP, Sci. Results, 154: College Station, TX (Ocean Drilling Program),* N. J. Shackelton, W. B. Curry, C. Richter, T. J. Bralower, Eds. (1997), pp. 299-318.
168. F. Boscolo Galazzo *et al.*, The middle Eocene climatic optimum (MECO): A multiproxy record of paleoceanographic changes in the southeast Atlantic (ODP Site 1263, Walvis Ridge). *Paleoceanography* **29**, 2014PA002670 (2014).
169. H. K. Coxall, P. A. Wilson, Early Oligocene glaciation and productivity in the eastern equatorial Pacific: Insights into global carbon cycling. *Paleoceanography* **26**, PA2221 (2011).
170. A. Holbourn, W. Kuhnt, M. Schulz, J.-A. Flores, N. Andersen, Orbitally-paced climate evolution during the middle Miocene "Monterey" carbon-isotope excursion. *Earth and Planetary Science Letters* **261**, 534-550 (2007).
171. C. H. Lear, Y. Rosenthal, H. K. Coxall, W. P. A., Late Eocene to early Miocene ice sheet dynamics and the global carbon cycle. *Paleoceanography* **19**, (2004).
172. D. Liebrand et al., Antarctic ice sheet and oceanographic response to eccentricity forcing during the early Miocene. Clim. Past 7, 869-880 (2011).
173. J. Tian, W. Ma, M. W. Lyle, J. K. Shackford, Synchronous mid-Miocene upper and deep oceanic $\delta^{13}C$ changes in the east equatorial Pacific linked to ocean cooling and ice sheet expansion. *Earth and Planetary Science Letters* **406**, 72-80 (2014).
174. V. Lauretano, F. J. Hilgen, J. C. Zachos, L. J. Lourens, Astronomically tuned age model for the early Eocene carbon isotope events: A new high-resolution $\delta^{13}C$ benthic record of ODP Site 1263 between ~49 and ~54 Ma. *Newsletters on Stratigraphy* **49**, 383–400 (2016).
175. V. Lauretano, K. Littler, M. Polling, J. C. Zachos, L. J. Lourens, Frequency, magnitude and character of hyperthermal events at the onset of the Early Eocene Climatic Optimum. *Clim. Past* **11**, 1313-1324 (2015).
176. B. S. Wade, H. Pälike, Oligocene climate dynamics. *Paleoceanography* **19**, PA4019 (2004).
177. K. Littler, U. Röhl, T. Westerhold, J. C. Zachos, A high-resolution benthic stable-isotope record for the South Atlantic: Implications for orbital-scale changes in Late Paleocene–Early Eocene climate and carbon cycling. *Earth and Planetary Science Letters* **401**, 18-30 (2014).
178. L. Stap *et al.*, High-resolution deep-sea carbon and oxygen isotope records of Eocene Thermal Maximum 2 and H2. *Geology* **38**, 607-610 (2010).

179. E. Thomas *et al.*, Early Eocene Thermal Maximum 3: Biotic Response at Walvis Ridge (SE Atlantic Ocean). *Paleoceanography and Paleoclimatology* **33**, 862–883 (2018).
180. P. M. Hull et al., On impact and volcanism across the Cretaceous-Paleogene boundary. *Science* **367**, 266-272 (2020).
181. V. Lauretano, J. C. Zachos, L. J. Lourens, Orbitally Paced Carbon and Deep-Sea Temperature Changes at the Peak of the Early Eocene Climatic Optimum. *Paleoceanography and Paleoclimatology* **33**, 1050-1065 (2018).

Acknowledgments: We thank Henning Kuhnert and his team for stable isotope analyses at MARUM, and the teams at the IODP Gulf Coast Core Repository (GCR) and the IODP Bremen Core Repository (BCR) for sampling. **Funding:** This research used samples and/or data provided by the International Ocean Discovery Program (IODP). Funding for this research was provided by the Deutsche Forschungsgemeinschaft (DFG, German Research Foundation) to TW (Project numbers 320221997, 242225091), UR (Project numbers 5410858, 28504316, 179386126, 242241969, 320221997); AH (Project numbers 48739182, 224193684 and 142157224); the Natural Environmental Research Council (NERC) to DAH; the DFG (Project numbers 386137731, 405856037) and the European Union's Horizon 2020 research and innovation program under grant agreement No 820970 to NM; the DFG (Project number 408101468) and by the European Union's Horizon 2020 research and innovation programme under the Marie Sklodowska-Curie grant agreement No 796220 to AJD; the National Science Foundation of China (Grant No. 41525020, 41776051) to JT; the NERC Isotope Geosciences Facility at the British Geological Survey (IP-1581–1115) to JB and KL; the NWO-ALW grant (project number 865.10.001) and Netherlands Earth System Science Centre (gravitation grant number 024.002.001) to LJL; the NSF (grant number EAR-0628719) to J.Z.. Funded through the Cluster of Excellence ›The Ocean Floor – Earth's Uncharted Interface‹ (research unit Recorder).
Author contributions: TW, UR, AJD, JCZ designed the study; TW, AJD, DL, DDV compiled and revised the astrochronology; NM applied recurrence analysis; EA synthesized the pCO_2 data; CA evaluated calcareous nannofossil datums; FF and TF produced magnetostratigraphic results and interpretation for ODP 1263; DAH, AJD, TW, UR provided bulk and benthic isotope data; AJD and RHW wrote the code for data processing and interpretation; JSKB, SMB, AJD, NM, AEH, DK, VL, KL, LJL, ML, HP, JT, PAW, UR, TW designed projects and generated data basis for the reference record as well as discussed/modified the manuscript. All authors contributed to writing the final manuscript. **Competing interests:** The authors declare no competing interests. **Data and materials availability:** All data are available in the main text or in the supplementary materials. All data are available open access in electronic form at the PANGAEA data repository (www. pangaea.de) http://doi.pangaea.de/ 10.1594/PANGAEA.10.1594/PANGAEA.917503.

Supplementary Materials:

Materials and Methods

Supplementary Text S1-S4

Figures S1-S35

Tables S1-S7

Data S8-S34

References (*45-181*)

Fig. 1. Cenozoic Global Reference benthic carbon and oxygen Isotope Dataset (CENOGRID) from ocean drilling core sites spanning the past 66 million years. Data are mostly generated using benthic foraminifera tests of the taxa *Cibicidoides* and *Nuttalides* extracted from carbonate rich deep-sea sediments drilled during ODP / IODP expeditions. Genus-specific corrections were applied and oxygen isotope data adjusted by +0.64‰ and +0.4‰, respectively (*12*), with the green dot indicating the average oxygen isotope composition of the last 10 kyr. Average resolution for the last 34 million years is one sample every 2 kyr, for the interval from 34 to 67 million years 4.4 kyr. After binning data were resampled and smoothed by a locally weighted function over 20 kyr (blue curve) and 1 Myr (red curve) to accentuate the different rhythms and trends in Earth's carbon cycle and temperature operating on various time scales. Oxygen isotope data have been converted to average temperature differences with respect to today (*13*). Future projections for global temperature (*44*) in the Year 2300 are shown by plotting three Representative Concentration Pathways (RCP) scenarios are plotted (light and dark blue, red dots). Gray horizontal bars mark rough estimates of ice volume in each hemisphere. Absolute ages for epochs and stages of the Cenozoic (GTS2012) and geomagnetic field reversals (this study) are provided for reference. Note that the oxygen isotope data axis is reversed to reflect warmer temperatures at times of lower $\delta^{18}O$ values. K/Pg is the Cretaceous/Paleogene boundary, Oi-1 is the first major glacial period in the Oligocene, M2 is the first major glacial event in the Northern Hemisphere.

Fig. 2. Climate states of the Cenozoic. Deep-sea benthic foraminifer high-resolution carbon (A) and oxygen (B) isotope records and the respective recurrence plots as well as scatter plots of long-term benthic foraminifer carbon versus oxygen values (C) and oxygen values versus atmospheric CO_2 concentrations (D). Recurrence analysis compares climate change patterns occurring in a specific interval to the entire record. If climate dynamics have similar patterns they will show up as darker areas in the plot, if they have no common dynamics the plot will remain white. Four distinct climate states can be identified as Hothouse, Warmhouse, Coolhouse, and Icehouse with distinct transitions among them. The relation of oxygen isotopes, representative for average global temperature trends, to atmospheric CO_2 concentrations suggests that the present climate system as of today (415 ppm CO_2) is comparable to the Miocene Coolhouse close to the Miocene Climate Optimum. If CO_2 emissions continue unmitigated until 2100 as assumed for the RCP8.5 scenario, the Earth climate system will be moved abruptly from the Icehouse into the Warmhouse or even Hothouse climate state.

Fig. 3. Quasi-periodic changes and determinism in the global reference carbon cycle and oxygen isotope record. Evolutionary FFT spectrogram, recurrence determinism analysis and benthic foraminifer oxygen (A) and carbon (B) isotope data plotted on age with the four climate states. Frequencies between two and sixty cycles per million years are related to changes in Earth's orbital parameters, known as Milankovitch cycles. The FFT spectrograms were computed with a 5-Myr window on the detrended records of benthic carbon and oxygen isotope data. From 67 to 13.9 Ma cyclic variations in global climate are dominated by the 405- and 100-kyr eccentricity cycles. Thereafter, in particular in the oxygen isotope record, the influence of obliquity increased, dominating the rhythm of climate in the record younger than ~7.7 million years. Recurrence analysis of determinism (DET) shows that climate in the Warmhouse state is more deterministic (predictable) than in the Hot-, Cool- and Icehouse. From 47 Ma towards the Eocene-Oligocene Transition at 34 Ma climate dynamic changes are rising in amplitude

approaching a threshold in the Climate System. If DET tends to low values, the dynamics are stochastic, whereas high values represent deterministic dynamics.

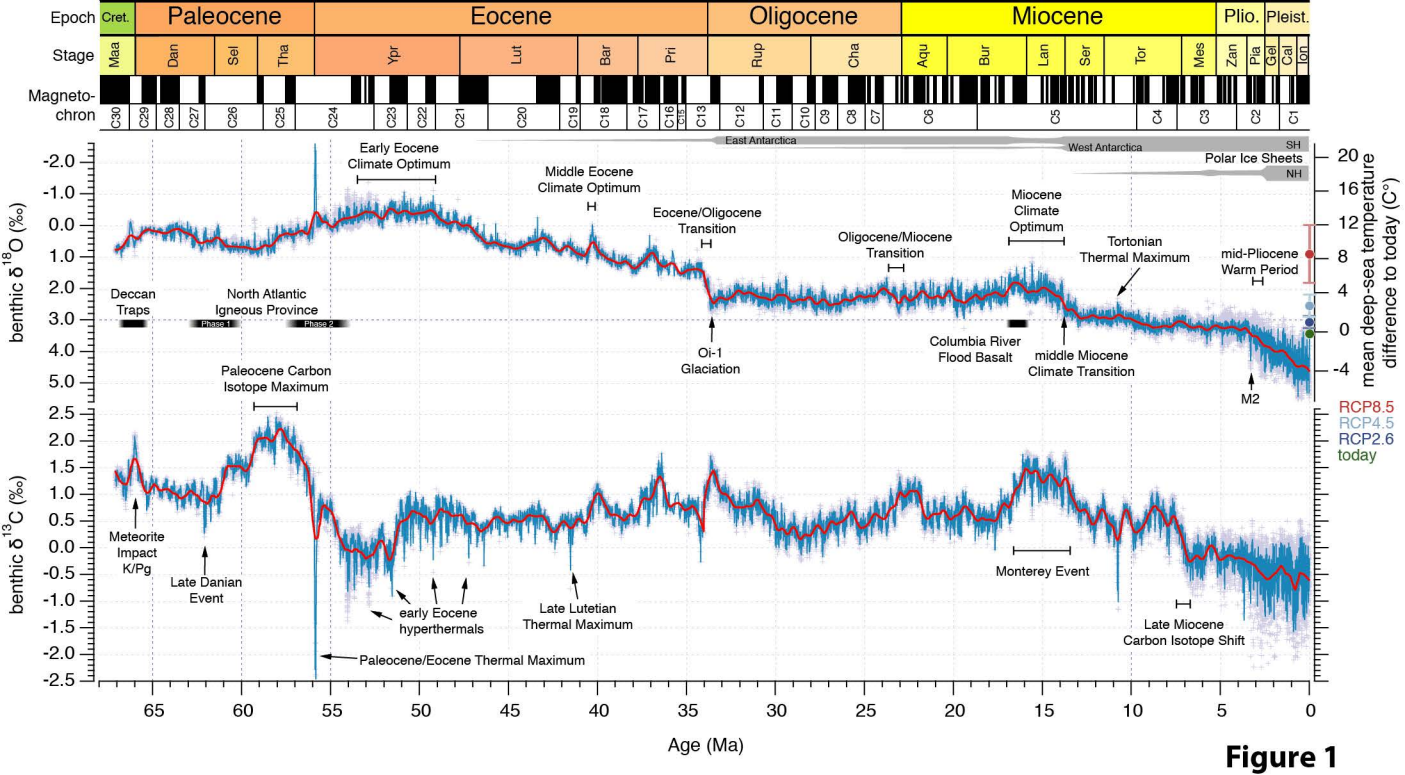
Epoch
Cret.
Paleocene
Eocene
Oligocene
Miocene
Plio.
Pleist.
Stage
Maa
Dan
Sel
Tha
Ypr
Lut
Bar
Pri
Rup
Cha
Aqu
Bur
Lan
Ser
Tor
Mes
Zan
Pia
Gel
Cal
Tgn
Magneto-chron
C30
C29
C28
C27
C26
C25
C24
C23
C22
C21
C20
C19
C18
C17
C16
C15
C14
C13
C12
C11
C10
C9
C8
C7
C6
C5
C4
C3
C2
C1
East Antarctica
West Antarctica
SH
NH
Polar Ice Sheets
Early Eocene Climate Optimum
Middle Eocene Climate Optimum
Eocene/Oligocene Transition
Oligocene/Miocene Transition
Miocene Climate Optimum
Tortonian Thermal Maximum
mid-Pliocene Warm Period
Deccan Traps
North Atlantic Igneous Province
Phase 1
Phase 2
Oi-1 Glaciation
Columbia River Flood Basalt
middle Miocene Climate Transition
M2
Paleocene Carbon Isotope Maximum
benthic δ18O (‰)
mean deep-sea temperature difference to today (C°)
RCP8.5
RCP4.5
RCP2.6
today
benthic δ13C (‰)
Meteorite Impact K/Pg
Late Danian Event
early Eocene hyperthermals
Late Lutetian Thermal Maximum
Paleocene/Eocene Thermal Maximum
Monterey Event
Late Miocene Carbon Isotope Shift
Age (Ma)

Figure 1

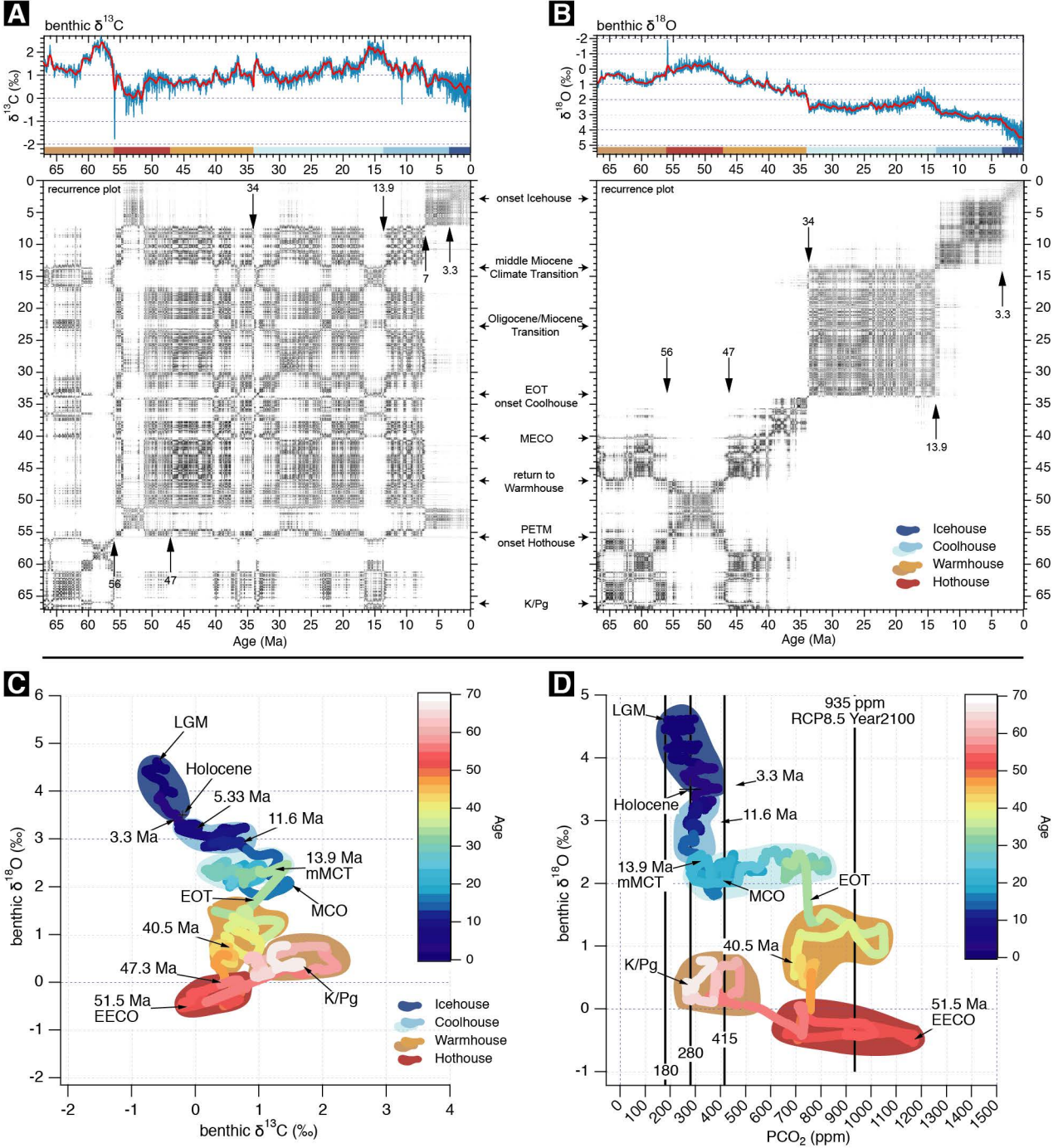
A
benthic δ13C
δ13C (‰)
B
benthic δ18O
δ18O (‰)
recurrence plot
34
13.9
7
3.3
56
47
onset Icehouse
middle Miocene Climate Transition
Oligocene/Miocene Transition
EOT onset Coolhouse
MECO
return to Warmhouse
PETM onset Hothouse
K/Pg
Age (Ma)
Icehouse
Coolhouse
Warmhouse
Hothouse
C
LGM
Holocene
5.33 Ma
11.6 Ma
3.3 Ma
13.9 Ma mMCT
EOT
MCO
40.5 Ma
47.3 Ma
51.5 Ma EECO
K/Pg
benthic δ18O (‰)
benthic δ13C (‰)
Age
D
935 ppm RCP8.5 Year2100
LGM
3.3 Ma
Holocene
11.6 Ma
13.9 Ma mMCT
MCO
EOT
40.5 Ma
K/Pg
51.5 Ma EECO
180
280
415
PCO2 (ppm)

Figure 2

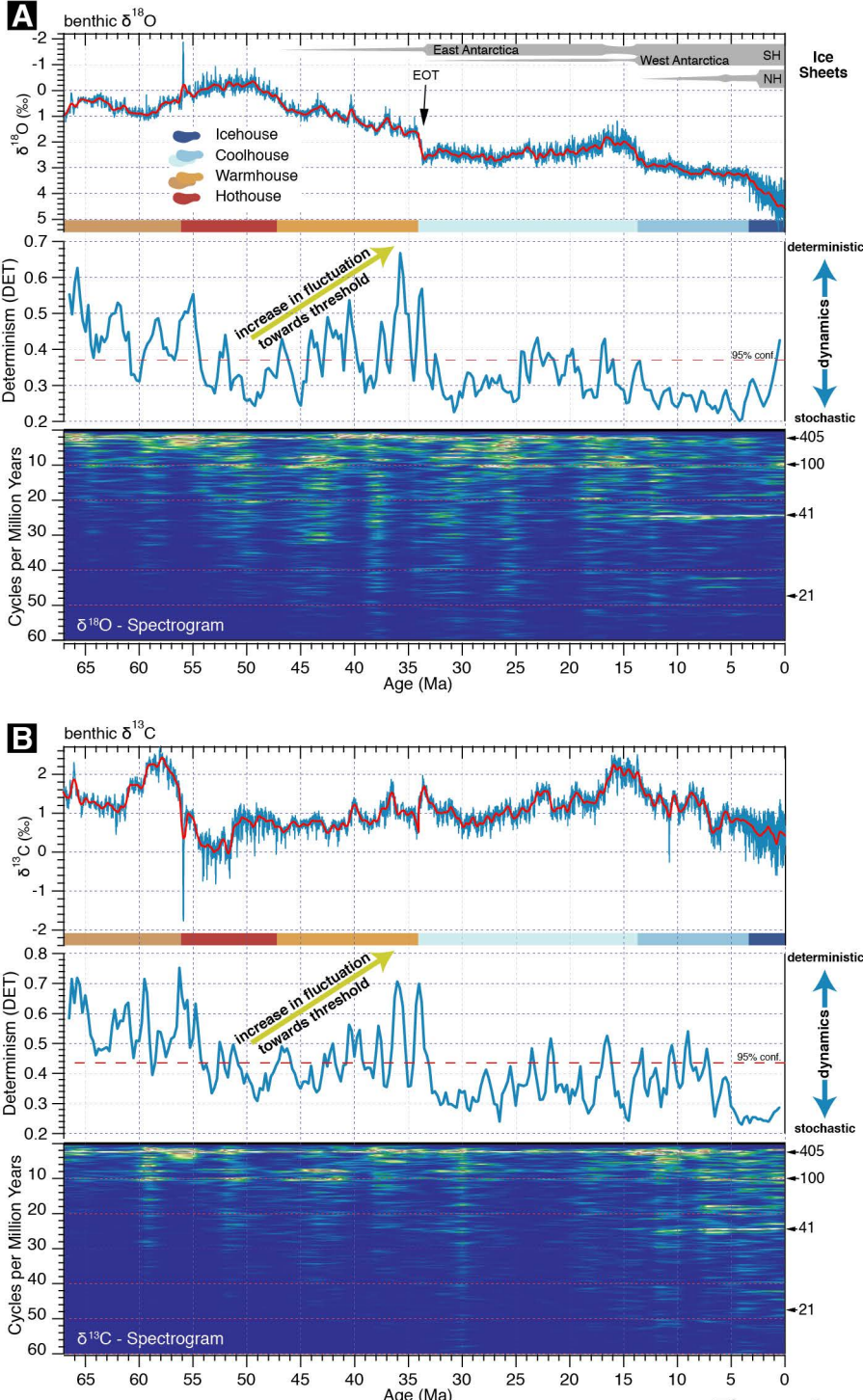
A
benthic δ18O
East Antarctica
West Antarctica
SH
NH
Ice Sheets
EOT
Icehouse
Coolhouse
Warmhouse
Hothouse
δ18O (‰)
Determinism (DET)
increase in fluctuation towards threshold
95% conf.
deterministic
dynamics
stochastic
Cycles per Million Years
405
100
41
21
δ18O - Spectrogram
Age (Ma)
B
benthic δ13C
δ13C (‰)
δ13C - Spectrogram

Figure 3

Science
AAAS

Science
AAAS

Supplementary Materials for

An astronomically dated record of Earth's climate and its predictability over the last 66 Million Years

Thomas Westerhold*, Norbert Marwan, Anna Joy Drury, Diederik Liebrand, Eleni Anagnostou, Claudia Agnini, James S. K. Barnet, Steven M. Bohaty, David De Vleeschouwer, Fabio Florindo, Thomas Frederichs, David A. Hodell, Ann E. Holbourn, Dick Kroon, Vittoria Lauretano, Kate Littler, Lucas J. Lourens, Mitchell Lyle, Heiko Pälike, Ursula Röhl, Jun Tian, Roy H. Wilkens, Paul A. Wilson, James C. Zachos

Correspondence to: twesterhold@marum.de

This PDF file includes:

Other Supplementary Materials for this manuscript include the following:

Data S8 to S34 as xlsx file

Data table titles S8 – S34:

Materials and Methods

1. New Stable Carbon and Oxygen Isotope Data

New high-resolution stable carbon and oxygen isotope data were generated on bulk carbonate and deep-sea benthic foraminifer carbonate from key intervals to assure full coverage of the Cenozoic. Here we describe the methods used to collect new data from biogenic carbonates at Sites 1263, 1264, and 1265. Ocean Drilling Program (ODP) Leg 208 Sites 1263 (28°32'S, 2°47'E), 1264 (28°32'S, 2°51'E), and 1265 (28°50'S, 2°38'E) drilled during Ocean Drilling Program (ODP) Leg 208 are located on the Walvis Ridge in the SE Atlantic (*45*) in 2,717 m, 2,505 m, and 3,059 m water depth (Fig. S1).

Bulk carbonate $\delta^{13}C$ and $\delta^{18}O$ analyses on 2000 freeze-dried and pulverized sediment samples from Site 1263 (80.69 to 156.40 rmcd depth) spanning the period from 32 to 41.7 Ma were undertaken at MARUM, University Bremen to validate and improve the benthic record. The bulk stable carbon and oxygen isotope data from the MARUM lab are reported relative to the Vienna Pee Dee Belemnite (VPDB) international standard, determined via adjustment to calibrated in-house standards and NBS-19. Bulk carbonate analyses at MARUM were carried out on Finnigan MAT 251 mass spectrometers equipped with automated carbonate preparation lines (Kiel I or III). Carbonate was reacted with orthophosphoric acid at 75 °C. Analytical precision based on replicate analyses of in-house standard (Solnhofen Limestone) is 0.03‰ (1σ) for $\delta^{13}C$ and 0.05 - 0.07‰ (1σ) for $\delta^{18}O$.

Benthic foraminifer tests carbonate $\delta^{13}C$ and $\delta^{18}O$ were measured on 2934 samples at MARUM and University of Cambridge. At the MARUM lab, good to moderately preserved specimen of benthic foraminifera *Nuttallides truempyi*, *Cibicidoides praemundulus, Oridorsalis umbonatus* (Eocene) from the >150µm fraction, as well as *Cibicidoides mundulus (C. kullenbergi)* and *Cibicidoides wuellerstorfi* (Miocene-Pliocene) picked from the 250-500µm fraction were measured on samples from ODP Sites 1263 (1998 samples), 1264 (85 samples), and 1265 (217 samples). Each measurement was made using a single species. Analysis at MARUM were performed on Finnigan MAT 251 with Kiel III, Finnigan MAT 252 with Kiel III, or ThermoFisher Scientific 253plus with Kiel IV automated carbonate preparation line. Samples were reacted with orthophosphoric acid at 75 °C. Analytical precision based on replicate analyses of in-house standard (Solnhofener Limestone) averages 0.02 - 0.04‰ and 0.05 - 0.07‰ (1σ) for $\delta^{13}C$ and $\delta^{18}O$, respectively. Data are reported relative to the Vienna Pee Dee Belemnite international standard, determined via adjustment to calibrated in-house standards and NBS-19.

At the University of Cambridge lab 634 20-cc samples taken every 2-3 cm from the composite section of ODP Site 1264 between 58 and 75 rmcd were processed. Oxygen and carbon isotope ratios were measured on the benthic foraminifer *Cibicidoides wuellerstorfi* and *Cibicidoides mundulus* from the >150 µm size fraction. Benthic foraminifer tests were cleaned in an ultrasonic bath to remove fine-grained particles and soaked in 15% H_2O_2 to remove surface organic contaminants prior to analysis. The number of specimens of *C. wuellerstorfi*/*C. mundulus* varied from 1 to 4. Each measurement was made using a single species. Benthic tests were crushed and between 20 and 60 µg of calcite were used for each analysis. The foraminifer calcite was reacted in orthophosphoric acid at 70°C using a Finnigan-MAT Kiel III carbonate preparation device. Evolved CO_2 gas was measured online with a Finnigan-MAT 252 mass spectrometer at the University of Florida. All isotope results are reported in standard delta notation relative to Vienna Pee Dee Belemnite (*46*). Analytical precision for both $\delta^{18}O$ and $\delta^{13}C$ was better than ±0.1‰.

All new stable carbon and oxygen isotope data are reported in the other supplementary materials Tab. S8 (Site 1263), Tab. S9 (Site 1264), Tab. S10 (Site 1265), Tab. S11 (Site 1263 bulk), and plotted against drilled depth in Fig. S2.

Our new bulk stable isotope data from ODP Site 1263 combined with the previously published data (*47*) compose to a 150-meter-long record with 3-5 kyr resolution covering the entire middle to late Eocene from 32 to 49 Ma (Fig. S2). The new benthic foraminifer data presented here span the period from 35.6 to 48.2 Ma. Together with the published data of the Late Lutetian Thermal Maximum (LLTM, (*48*)), latest Eocene (*49*) and the EOT (*50),* the Site 1263 benthic foraminifer record has an unprecedented average resolution of 5-7 kyr over the entire middle to late Eocene.

New benthic foraminifer stable isotope data were generated with samples from ODP Site 1264 (Fig. S2) to fill gaps in the record after revision of the late Miocene-Pliocene shipboard composite splice and extend the published 0 to 5.25 Ma record (*51*) back to 6.1 Ma. At ODP Site 1265 new benthic foraminifer data (Fig. S2) were generated between 38.0 and 39.4 Ma to test the revised composite record for Site 1263 (see below) as well as between 48.0 and 49.8 Ma to cover an interval of coring disturbance in Site 1263 (*52*).

2. Splice revision Site 1263

Deep-sea drilling techniques and methods have evolved and now allow to retrieve complete nearly undisturbed and successive 9.6-meter-long cores from the upper 200 to 400 meters of the soft sediment pile. Between the consecutively taken drill cores a recovery gap always exists, mostly due to ship motion (*53*). Common practice is to drill several offset, parallel holes at the same site, to then correlate all cores using physical properties data and core images (*54*) to generate a complete record from spliced intervals out of the parallel cores that represents the full sedimentary package targeted by drilling. The splicing of cores towards a composite heavily relies on the core and data quality used for correlation. The shipboard composite record of Site 1263 was already revised using shipboard magnetic susceptibility data and high-resolution digital line scan core images (W15 splice; (*47*)). Due to slight coring disturbance this revision revealed a difficult to splice interval around 125 rmcd between cores 1263B-6H, 1263B-7H, and 1263C-2H, which required a reevaluation by additional parameters, in this case stable isotope data.

Therefore, we generated high-resolution stable isotope data at on benthic foraminifer tests extracted from Cores 1263C-2H and 1263B-7H (Fig. S3) that reveal a mismatch in the overlapping interval between cores at 126 rmcd in the W15 splice (*47*). By moving Core 1263C-2H up by 50 cm, a reasonable match was found. To validate this correlation, we generated a benthic foraminifer stable isotope data on the complementary interval in ODP Site 1265 that supports the new correlation. Revised offsets (Tab. S12), revised composite (Tab. S13), and revised mapping pairs (Tab. S14) as well as corrected site-to-site correlation ties are given in the other supplementary materials (Tab. S15, S16, S17).

3. Paleomagnetic data Site 1263

To contribute towards the compilation of an updated Cenozoic geomagnetic polarity time scale (GPTS; see Section 4), we generated a new astronomically-tuned magnetostratigraphy at ODP Site 1263 spanning Chron C12r to C19n, as this interval was poorly calibrated elsewhere.

The geocentric axial dipole field at the geographic latitude of Site 1263, assuming that the site location did not change significantly its position within the last 40 Myr, has an inclination of ca. ±47°, which makes it feasible to reconstruct paleomagnetic polarity using only inclinations. During ODP Leg 208, the bulk of the remanence measurements was made using a pass-through cryogenic magnetometer (model 760R) (*45*). The Natural Remanent Magnetization (NRM) was routinely measured before and after alternating field (AF) demagnetization at 5-cm increments, with 10-cm-long headers and trailers, on all archive-half core sections from Holes 1263A, 1263B, 1263C. Time constraints permitted analysis with only 2 or 3 AF demagnetization steps at 10 and 15 mT peak values for most of the core sections. Only Section 1263B-2H3 was demagnetized up to 25 mT. The low-maximum-peak AFs ensured that the archive halves remained useful for shore-based palaeomagnetic studies.

Natural remanent magnetization (NRM) was measured on 586 discrete cube samples (dimensions 2 cm x 2 cm x 2 cm) to document magnetic polarity Chrons C12r (earliest Oligocene) to C19r at ODP Site 1263. In total, 43 discrete samples were analyzed at the Faculty of Geosciences, University of Bremen, spanning Chrons C18n to C19r, and 543 discrete samples at Istituto Nazionale di Geofisica e Vulcanologia (INGV, Rome) covering Chrons C12r to C18r.

At the Faculty of Geosciences, University of Bremen, paleomagnetic directions and magnetization intensities were determined using a cryogenic magnetometer (2G Enterprises model 755 HR). NRM was measured on each sample before being subjected to a systematic alternating field demagnetization treatment involving steps of 7.5, 10, 15, 20, 25, 30, 40, and 60 mT. Intensities of orthogonal magnetic components of the remanent magnetization were measured after each step. A detailed vector analysis (*55*) was applied to the results in order to determine the characteristic remanent magnetization (ChRM) without anchoring to the origin of the orthogonal projections by choosing an individual demagnetization interval for each sample.

All samples but one showed a reversed, mostly steep, probably drilling induced, magnetic overprint of relative high intensity, which was easily removed at a demagnetization level of 7.5 mT (Fig. S4, S5). NRM intensities range from 3.1 to 33.4 $x10^{-3}$ Am^{-1} with a mean of 9.9 x 10^{-3} A m^{-1}. The maximum peak demagnetization field (60 mT) reduced the NRM to about 3% in average of the NRM intensity prior to AF demagnetization, indicating a dominant low-coercive magnetization and no clear evidence for high-coercive NRM carriers. Declinations shown here were not corrected for core orientation in the horizontal plane because our reversal stratigraphy is based on inclination data only.

The majority of the samples (> 95%) provide very stable ChRM results with maximum angular deviations (MAD), a measure of the determination of the ChRM direction, lower than 5° (mean ~3.4°). The mean normal (reversed) inclination is -32° (39°), which is slightly shallower than -47° to be expected for a geocentric axial dipole assuming that the site location had not significantly moved within the last 40 Myr.

For analysis at the INGV ODP Holes 1263A, 1263B, 1263C were sampled between August 2007 and April 2008 using standard 8 cm^3 plastic cubes at the Integrated Ocean Drilling Program (IODP) Bremen Core Repository, where the core is curated. 543 samples were taken from 1263B-2H-3,3 to 1263A-15H-7,29, between depths of 58.52 (67.53 rmcd) and 134.78 mbsf (158.65 rmcd) and oriented with respect to vertical. To minimize sample dehydration and alteration, samples were packed in sealed bags and were stored in a refrigerated room until they were processed at the INGV. NRMs were analyzed within a Lodestar Magnetics shielded room (internal field < 200 nT) using a 2-G Enterprises automated cryogenic magnetometer (model

755R) with an internal diameter of 4.2 cm and equipped with three DC SQUID sensors (noise level 3 x 10^{-9} Am^2/kg).

Before performing routine demagnetization of all samples a pilot study on 32 samples was conducted to determine the most appropriate demagnetization technique. Fourteen samples were subjected to AF demagnetization at successive peak fields of 5, 10, 15, 20, 25, 30, 35, 40, 50, 60, 70, 80, 90 and 100 mT. The remainder 18 samples were carefully removed from the plastic cubes and subjected to progressive thermal demagnetization from room temperature up to 650°C at the following steps: 100, 200, 300, 330, 360, 400, 500, 550, 600, 650°C.

In most cases, the pilot study at INGV demonstrated that thermal and AF demagnetization were both effective in removing secondary remanence components and in isolating the ChRM. AF demagnetization, up to peak fields of 80-100 mT, was adopted for routine treatment of samples because it was less time-consuming and because it avoided the possibility of thermal alteration during demagnetization, which would hinder future analysis of the magnetic mineralogy content. Most of the samples from ODP site 1263 are affected by a steep reversed polarity overprint which appears to be drilling induced (Fig. S6 and S7). This magnetic overprint was successfully removed at peak fields of 10-15 mT.

For a few samples, AF demagnetization above 40 mT was obscured by the simultaneous acquisition of a gyroremanent magnetization (GRM) (e.g., (*56, 57*) suggesting the presence of a single-domain material (Fig. S7d). The ChRM was generally isolated at fields below 40 mT and consequently the GRM acquisition did not hamper the polarity interpretation for these samples. NRM stability was assessed using vector component diagrams (*58*). Principal component analysis (*55*) was used to calculate characteristic remanent magnetization (ChRM) directions, with linear best fits calculated from a minimum of three demagnetization steps using the PuffinPlot paleomagnetic analysis application (*59*). The maximum angular deviation (MAD) was calculated to provide an estimate of the precision for each best-fit line. Samples were only included in this study if MAD values were less than 10°.

Five hundred twenty-nine samples (ca. 97%) are characterized by stable ChRMs which allows construction of a detailed magnetic polarity zonation for the studied interval. NRM intensities range between 2.65 x 10^{-5} A m^{-1} and 1.55 x 10^{-2} A m^{-1} with a mean of 5.52 x 10^{-3} A m^{-1}. The normal and reversed polarity ChRM inclinations are grouped in two nearly antipodal clusters, as expected for reliable ChRM directions, with the mean normal and reverse inclinations of -30° and 32°, respectively. In conjunction with evidence from vector component diagrams this indicates that secondary overprints were successfully removed by stepwise AF demagnetization.

Applying calcareous nannofossil events documented in Site 1263 (*45, 52*; Tab. 18) to the inclination record (Tab. S19), we establish a paleomagnetic polarity interpretation (Fig. S8, Tab. S20). The resulting new Site 1263 magnetostratigraphy spanning Chron C12r to C19n is given in Table S21.

4. Cenozoic Magnetostratigraphy

The complete Cenozoic geomagnetic polarity time scale (GPTS) is given in the *Geomagnetic Polarity Time Scale (60),* the *The Neogene Period* (*61*) and *The Paleogene Period* (*62*) chapters of the Geological Time Scale 2012. Since the publication of the GPTS in 2012 several new-high resolution magnetostratigraphic records have been produced mainly refining the Paleogene Period. Here we have compiled additional recent magnetostratigraphic

interpretations from base of Chron C6n to the top of C30n (Tab. S22) and applied the new astrochronology (see below) to form a new GPTS from 19.727 to 66.393 Ma (Tab. S23) consistent with the new tuned benthic foraminifer stable isotope reference record. The differences to the GPTS 2012 in this interval are less than 400 kyr (one 405 kyr eccentricity cycle) except for Chron C21n and C22n (Fig. S9). Two independent studies have refined the early to middle Eocene magnetostratigraphy for Chron 21 to 24 using deep-sea records (*52*) and a pelagic/hemipelagic succession of the western Tethys Possagno section (Southern Alps, northeastern Italy;(*63*)). Consistently they reach similar ages and durations for Chrons C21n, C21r and C22n. In the GPTS2012, the age calibration within this interval was difficult due to relatively large uncertainty in the radioisotopic ages of the Montanari ash, located in Chron C21n and used to calibrate the GPTS (*64, 65*). For the interval younger than the base of Chron C6n (19.727 Ma), we applied the GPTS2012 because no major changes are apparent so far. Only the interval between top Chron C3An.1n (6.023 Ma) and top Chron C4r.1n (8.236 Ma) was replaced by the recent refinement from IODP U1337 (*22*), where for the first time an astronomically tuned benthic foraminifer stable isotope stratigraphy (1.5 kyr resolution) and magnetostratigraphy from a single deep-sea location was combined for this time interval.

5. Astrochronology

Dating of geological archives by astrochronology provides accurate age models at a resolution not achieved by any other dating method for the Cenozoic (*66*). The breakthrough of our study is to present an unprecedently high resolution, astronomically tuned benthic foraminifer stable isotope record spanning over the entire Cenozoic. In this section, we describe the development of the astronomically tuned age model for the deep-sea sediment successions.

Quasiperiodic cycles with periods in the order of 10^4 and 10^5 years are found in many geological records and are known as Milankovitch cycles. The distribution and quantity of the incoming solar radiation vary due to subtle variations of the Earth's orbit around the Sun caused by the gravitational interaction of larger bodies in the Solar System. Over the timeframe of tens- to hundreds of thousands of years, climatic patterns on the Earth respond to the quasiperiodic orbital forcing recorded as rhythmic variations in numerous paleoclimate proxy records. Milankovitch cycles show characteristic rhythms of 21 kyr (precession), 41 kyr (tilt or obliquity), 100 and 405 kyr (both eccentricity). Cyclostratigraphic age models evolve out of the recognition of these cycles in geological data using the quasi-regular Milankovitch beats as a natural metronome to measure elapsed time. Matching Milankovitch cycles containing records to long-term numerical solutions for the insolation quantities of the Earth results in highly accurate astrochronologies (*66*).

By combining the numerical solutions of precession, obliquity and eccentricity one can form target curves to which to correlate geological data to. Correlation of the geological data to the astronomical target results in astrochronologies that are of much higher resolution and in effect more precise and accurate than any other geological dating technique over the Cenozoic. All of the published benthic foraminifer isotope records used in CENOGRID have an astrochronology, either as provided in the respective publication or refined if needed (see Tab. S1, S24 to S32). From 0 to 20 Ma, the integrated records are tuned to an astronomical target that is a appropriate combination of eccentricity, obliquity and/or precession (*20, 22, 54, 67-69*). For records older than 20 Ma, only eccentricity was used as a target curve due to (a) the less evolved expression of precession and obliquity in the geological records and (b) the uncertainty in

precession and obliquity in the astronomical solutions itself. Details about the splice reference record for each record are given in Section 6 below.

The most prominent and stable astronomical cycle is the 405-kyr eccentricity cycle, which is driven by the planetary perturbations caused by Venus and Jupiter (*70*). Cenozoic deep-sea foraminifer stable carbon isotope records are predominantly imprinted by this cycle (*71*) suggesting a tight link between orbital forcing and the climate system, likely due to intricate feedback mechanisms in the carbon cycle (*30, 72*). Most of the orbital cycles experience marked changes in their periodicity and phasing due to the dissipative effect of the Earth-Moon system, friction, dynamic changes in the distribution of masses in the Earth and on Earths' surface, as well as chaotic diffusion of the Solar System (*14, 66, 70, 73*). Therefore, numerical solutions for precession and obliquity can only provide accurate targets back to about 10 to 20 Ma (*74, 75*), and usable targets back to 40 Ma (*70*). As said before, for intervals older than 20 Ma, eccentricity-related cycles provides the only accurate tuning target.

Major components of Earths' orbital eccentricity have a period of ~95 kyr (Mars – Jupiter), ~124 kyr (Mars – Venus), ~405 kyr (Venus – Jupiter), and ~2.4 Myr (Earth – Mars) (*70*). Accurate tuning to numerical solutions of eccentricity are limited by the chaotic behavior of the inner Solar System planets and the largest bodies in the asteroid belt (*14, 70*). Recent orbital solutions (*14, 76*) are valid from 0 to ~54 Ma for all eccentricity components, whereas only the 405-kyr eccentricity cycle is stable and can be used for astronomical tuning back to 200 Ma (*14, 66, 77*). However, comparison to geological data from the Eocene (*52*) and Paleocene (*78*) suggests that the La2010b solution (*14*) best matches to the observed eccentricity related cycle modulations imprinted in the records older than 50 Ma. Therefore, we used the La2010b orbital eccentricity solution to establish a consistent astrochronology for the Eocene and Paleocene. Tuning more negative carbon isotope values to short eccentricity maxima in the La2010b solution (*30, 35, 79, 80*) avoids distortion effects in the $\delta^{13}C$ 405-kyr component due to the residence time of carbon in the ocean-atmosphere system and to the enhanced carbon isotope excursions of hyperthermal events (*52, 81*). We do not use the recently published ZB18a orbital solution because it is almost identical with the La2010b up to 58 Ma, and beyond 58 Ma it is unconstrained due to chaotic behavior (*76*). Furthermore, in the ZB18a solution some parameters have been varied beyond physically realistic values (pers.comm Jacques Laskar) and, thus, need to be tested first before being applied. For the same reason, we do not apply the recently proposed age (*76*) for the Paleocene/Eocene boundary or onset of the PETM.

All age models applied to the individual records used for the CENOGRID are given in Tab. S24 to S32. For the new benthic foraminifer stable isotope data generated from Site 1263 (middle to late Eocene) and Site 1264 (early Pliocene to late Miocene) samples we ascertained astrochronologies where necessary. Benthic carbon isotope data from the earliest Oligocene to late Eocene interval at Site 1263 exhibit a distinct eccentricity-related cyclicity (Fig. S10), which was used to tune the record from 32.7 to 42 Ma (Fig. S11). The astrochronology for Site 1264 from 0 Ma to 6.1 Ma is from Drury et al. (https://doi.pangaea.de/10.1594/PANGAEA.919489). It is based on tuning of the high-resolution $\%CaCO_3$ record was tuned to a normalized eccentricity, tilt and precession (E+T-P) target, guided by benthic $\delta^{18}O$ where available, using a similar approach ($\%CaCO_3$ maxima/benthic $\delta^{18}O$ minima tuned to E+T-P maxima) as in (*22*).

6. Cenozoic global reference benthic foraminifer carbon and oxygen isotope dataset (CENOGRID)

To compose the new high-fidelity Cenozoic benthic foraminifer stable carbon and oxygen isotope reference record, we selected the temporally best resolved deep-sea records from the Atlantic and Pacific Oceans featuring published astrochronologies. Additionally, we filled gaps, expanded these existing records, and generated new data for the early Pliocene to late Miocene (Site 1264) and middle to late Eocene (Site 1263) intervals. We included records from 14 ODP and IODP sites (Fig. S1) from the Atlantic: ODP Leg 154 Ceara Rise Sites 925, 926, 927, 928, and 929; ODP Leg 207 Demerara Rise Site 1258; ODP Leg 208 Walvis Ridge Sites 1262, 1263, 1264, and 1265; and the Pacific: ODP Leg 184 South China Sea Site 1146; ODP Leg 199 East Equatorial Pacific Site 1218; IODP Exp. 320/321 East Equatorial Pacific Sites U1337 and U1338. These sites are also ideal as it is possible to correlate between sites and compare coeval datasets, thereby highlighting the optimum, expanded intervals to use at each location in order to best target a consistent global signal. To avoid systematic interspecies isotopic offsets in isotope data (*12, 82*), whenever possible we only used species of the genus *Cibicidoides* and *Nuttallides*, as suggested by (*4*). The isotopic correction factors applied are given in Tab. S2 and Fig. S12. To obtain the best estimates of oxygen isotopic equilibrium and carbon isotopic composition of ocean deep-water dissolved CO_2, adjustment factors were applied (Tab. S3) and documented for each isotope value.

After compiling, generating, testing and refining astrochronologies for all the records as well as correcting interspecies offsets, we calculated a 10-point LOESS smooth and plotted the smooth along with the data (Fig. S13). Then we ascertained the optimal position to switch from one record to the next and determined the isotopic offsets between records from different ocean basins. The later step is necessary to produce a single high-fidelity reference record that documents the overall global carbon and oxygen isotope evolution in the Cenozoic. The Pacific Ocean is the largest ocean and probably best resembles a global mean, therefore all data were offset with respect to the equatorial Pacific values (Sits 1218, U1337, U1338; Fig. S14). One has to realize that single, continuous, individual high-resolution records for each of the different ocean basins and spanning the entire Cenozoic are unrealistic due to local sedimentation effects (gaps and condensed intervals) in available deep-sea sections. Comparing the evolution of ocean basin geochemistry is tempting having the new reference record at hand, but beyond the scope of this manuscript. It also involves an order of magnitude more effort to revise the published composite records from all three major ocean basins and their age models.

Ten switch points were defined where we switched from one record to the next (Fig. S15 to S24) to build a continuous high-fidelity record utilizing the specifies given in Tab. S5. We defined optimal points to switch between records to ensure the maximum resolution possible and from locations, where the isotope signals between records are highly consistent. In the latest Eocene interval the time resolution of available records is lower (Fig. S22 and S23), therefore we used the bulk isotope records to ensure that the age models are well synchronized. Due to severe dissolution across the 34.025 to 34.308 Ma interval of Site 1218, the Eocene-Oligocene Transition (EOT) (Fig. S22), we had to switch from Site 1218 to Site 1263. Low data coverage at 35.5 Ma forced us to introduce an uncertain switch (Fig. S23), which may need a refinement when additional benthic isotope records become available. However, this would require new ocean drilling campaines, because currently no high-resolution sedimentary section provides a continuous benthic foraminifer isotope record at a single location and at the same time unaffected by dissolution.

After the data for the reference record were merged (Fig. S25, Tab. 33), the average sample resolution was determined. Average sample resolution from 0 to 34.025 Ma is 2 kyr and from 34.025 to 67.100 Ma is 4.4 kyr (Tab. S6). The lower sample resolution for the Eocene and Paleocene is due to lower sedimentation rates and lower sample resolution of the available records. Based on this observation, we divided the reference record in two intervals for subsequent binning and smoothing of data. We binned the data into equally spaced bins of respectively 2 kyr and 5 kyr bins for the younger and older intervals. The bin sizes were determined based on the average sample resolution. Binning was done by dividing a weighted histogram of the data by a frequency histogram of the data in IGOR Pro 8 (Wavemetrics). Where empty bins occurred, the bin was filled with interpolated data based on surrounding bins, to provide a continuous and equally spaced dataset for smoothing. To minimize the effects of outliers the records were then smoothed in IGOR Pro 8 using a nonparametric LOESS quadratic regression smooth with a tricube locally-weighted function equivalent to a 20-kyr smooth window. This equated to a 10-point smooth for the 0 to 34.025 Ma interval and 5-point smooth for the 34.025 to 67.100 Ma interval. To generate a long-term trend curve equivalent to a 1-Myr smooth window, the reference record was LOESS smoothed over 500 points for the 0 to 34.025 Ma interval and 250 points for the 34.025 to 67.100 Ma interval (Fig. S26). The binning and smoothing avoid biases due to intervals with higher sample resolution and data density and provide a balanced view for the entire Cenozoic at higher resolution than before (Fig. S27). The benthic deep-sea foraminifer carbon and oxygen isotope reference record and LOESS smoothed data are provided in Tab. S33 and S34.

Sampling Biases - Cenozoic deep-sea benthic foraminifer oxygen isotope data essentially track mean deep-sea temperature and ice sheet evolution (see *1, 4, 83*). The temperature component of the oxygen isotope record essentially tracks mean deep-sea temperature which is set by surface conditions at sites of water mass formation. It has been suggested that the low latitudes may have contributed to sites of water mass formation under past warm climate states but the balance of evidence suggests that that the main explanation for the very warm intermediate and deep waters evidenced in the oxygen isotope record during the warm climate states are warm surface water conditions at high latitude sites of water mass formation during the season of deep convection (winter) with southern hemisphere sources dominant (e.g., *84-87*). Biases in benthic foraminifer records have been discussed in detail by (*1, 4*). Another issue is the bias due to the uneven distribution of deep-sea stable isotope data in both space and in time, particularly in the early Cenozoic with few high-resolution records. Splicing records from different regions can create artificial steps in the global record. Compared to previous records, the CENOGRID significantly reduces the temporal limitations (sampling density), but not the regional distribution issues (*4*). The regional distribution and water depth bias can only be solved by getting access to multiple new records from low to high latitudes over a range of water depth, a major endeavor for future scientific ocean drilling. However, the global imprint on the individual records included in CENOGRID is supported by the consistency in the variability of overlapping datasets, which partly mitigates the sampling bias caused by the regional distribution of sites. An additional bias of warmer time intervals like the Paleocene and Eocene is the perception that thermal gradients within the deep-sea were greater than today, making surface temperature reconstruction more complicated. Isotope records of planktic foraminifer to document surface ocean conditions could help here, but early diagenesis tends to bias the records towards deep-sea isotope values (see (*88*)).

For the Cenozoic temperature/ice-volume reconstructions the biases have limited affects. The late Neogene oceans were thermally homogeneous and a greater density of high-resolution available records means we have a greater understanding of the global versus regional imprint on individual records. In the compilation of Cramer et al. 2009, which separated records from different oceans, Eocene benthic foraminiferal $\delta^{18}O$ values seem rather homogenous and suggest minor temperature differentiation amongst deep water source regions. In contrast, $\delta^{18}O$ records from the Pacific Shatsky Rise Site 1209 (*16*) and the Atlantic Walvis Ridge Sites 1262/1263 (*89*) show a consistent pattern from 66 to 45 Ma. Thus, the CENOGRID presented here is assumed to be the currently best global temperature/ice-volume recorder.

For the global benthic foraminiferal carbon isotope record, spatial biases are more important toward the younger part of the record, the Neogene, because of circulation related basin to basin fractionation. Paleogene $\delta^{13}C$ records from Atlantic and Pacific show the same variability but are, as expected, offset and thus can be treated as an average global carbon cycle recorder.

7. Recurrence Analysis

Recurrence analysis (RA) is used to identify transitions between different types of dynamics. A recurrence plot (RP) is a binary matrix where the coordinates of each entry mark the pair of time points with recurring states (*90*). A value one at column i and row j represents that state at time i recurs at time j. A recurrence is defined by the pairwise comparison of all values in the time series, whether their distance is smaller than a predefined threshold. The threshold is selected in a way that the fraction of recurrences is 10% of the number of pairwise comparisons (*91*). The graphical rendering of the RP can be used to get a first visual impression of the type of dynamics and to identify changes of the dynamics. RP is a powerful tool to reveal nontrivial dynamical features, i.e., not only periodic dynamics, but also intermittent regimes or chaos-chaos-transitions. For example, block-like structures in the RP identify epochs where the dynamical system is 'trapped' in a particular state.

We conducted RA on the CENOGRID in the time domain. Analysis was performed on the undetrended (Fig. S32) and detrended isotopes records (Fig. S33). Data were resampled at 0.005 Ma and detrended using a 5^{th} order Butterworth-filter with cutoff-frequency of 0.1 Ma.

An RP contains a number of interesting and important small-scale features, such as single points or diagonal lines (*15*). A diagonal line corresponds to episodes of similar evolution of states. A dominance of single points indicates stochastic processes. The more diagonal lines exist with respect to single points, the more deterministic or predictable the process would be. To quantify this property, the fraction of recurrence points that form diagonal lines with respect to all recurrence points was introduced and is called "Determinism" (DET) (*15*). DET ranges from zero to one. If DET tends to low values, the dynamics is stochastic, whereas high values represent deterministic dynamics.

The temporal change of DET is calculated by using a sliding window approach (window size 1 Ma, moving step size 0.25 Ma). By using a specific bootstrap test, the 95% confidence level for significantly elevated DET values can be determined (*92*). It is important to note that each given DET value corresponds to the center of the moving window. Therefore, the analysis provides insight to significant changes in DET, equal to significant changes in the dynamics of the system, that occur within less than 1 Ma. The method cannot resolve abrupt changes on the order of thousands and tens of thousands of years. Nevertheless, the analysis of the detrended data (Fig. S33) documents distinct white bands in the recurrence plots. These bands mark

transitions in the climate dynamics and coincide with major changes or events recorded in benthic foraminifer isotopes.

8. Global Temperature Record and Past Atmospheric CO_2 Levels

We use the approach in (*93*) to transpose the deep-sea temperature changes recorded in the benthic foraminifer oxygen isotope data into average global changes in surface air temperature scaled to the 1961–1990 mean. Deep-sea benthic foraminifer oxygen isotope $\delta^{18}O$ values are controlled by changes in deep-ocean temperature and global ice mass over the Cenozoic (*83*). Therefore, variations in ice growth need to be taken into account prior to estimating deep-ocean temperature changes. Prior to the onset of large polar ice sheets on Antarctica at 34.025 Ma, deep-sea temperature can be approximated assuming that most of the ~1.8‰ increase in $\delta^{18}O$ from the Early Eocene Climate Optimum (EECO) to the end of the Eocene is due to a 7–8°C change in temperature (1). After the major onset of a large polar ice sheet in Antarctica at the Eocene-Oligocene Transition (EOT) ice volume and deep-sea temperature changes both contribute to the variance in benthic foraminifer $\delta^{18}O$ values (*94*). With the appearance of larger ice sheets in the Northern Hemisphere the contribution of global ice mass variations to $\delta^{18}O$ values increased at 3.6 Ma and 1.81 Ma. Taking this into account, (93) proposed three equations (equations 1 to 3 in Tab. S7) to transfer deep-sea $\delta^{18}O$ values into temperature estimates for the Cenozoic. We applied these three equations to the three time intervals to compensate for different contributions of ice sheet variations to the $\delta^{18}O$ signal. Our intent is not to develop a new scheme to transpose the benthic foraminifer record but just to account for the potential influences of ice-volume during those periods for which major ice-sheet expansion occurred (on Antarctica in the Miocene and the N. Hemisphere at 2.7 Ma) as indicated by independent evidence.

To compare changes in global temperature relative to today, the deep-sea $\delta^{18}O$-derived temperatures have to be transposed into surface air temperature changes. We follow the relation between deep ocean and surface temperature change (equations 4, 5, 6 in Tab. S7) and calculate the temperature change with respect to the Holocene mean temperature of 14.15 °C as given in (*93*).

Estimates for past atmospheric CO_2 levels are compiled from (*95*) and references therein, (*96*) and references therein, and from (*97-105*). Atmospheric CO_2 estimates including the upper and lower estimate were LOESS smoothed in IGOR Pro 8 over 30 data points. References in (*95*) are on the GPTS2012 (*60*). Additional atmospheric CO_2 estimates are on their individual age models, because the uncertainty for atmospheric CO_2 estimates is much larger than the difference between GPTS2012 and our updated GPTS ages.

Supplementary Text

S1 - Earth's Trends, Rhythms, and Aberrations

Trends: The general long-term trends in global climate as represented by the spliced oxygen isotope record (the red curve in Fig. 1) confirm the patterns obtained in the previously published low-resolution stacks (e.g. (*1*)). These trends are partly influenced by modifications in boundary conditions due to tectonic processes (*106*) including continental geography and topography, oceanic gateway locations and bathymetry, but mainly by the concentrations of atmospheric greenhouse gases, finely balanced between volcanic CO_2 outgassing and consumption by weathering of silicate mineral rocks (*107*). It is generally accepted that the overall increase in the relative abundance of oxygen isotopes values reflects the formation of large polar ice sheets and a decrease in mean deep-ocean temperature, a trend that largely corresponds with a long-term decline in atmospheric pCO_2. Supported by more recent independent evidence, its well accepted that the prominent steps towards greater oxygen isotope values mark major stages of polar ice sheet growth: the Eocene/Oligocene Transition (EOT) 34 million years ago with the large scale expansion of the East Antarctic Ice Sheet (EAIS, *17*), the middle Miocene Climate Transition (mMCT, *108*) 13.9 million years ago with the expansion of the West Antarctic Ice Sheet (WAIS) and with the re-expansion or further expansion of the EAIS, and the intensification of the Northern Hemisphere Glaciation ~2.7 million years ago (*109*).

The benthic carbon isotope record, which is generally assumed to be sensitive to changes in the global carbon cycle (*110*), over long time scales, shows a number of key features, most of which often relate to climate (Fig. 1). Aside from the effects of the K/Pg extinctions (*111*), the most striking features of the marine C isotope record are the late Paleocene carbon isotope maximum (PCIM) and the Miocene Monterey Event, thought to represent periods of large changes in organic carbon burial caused by enhanced marine productivity or increased burial of biomass, terrestrial and/or marine (*20, 82, 112-114*). Synchronous with the first major glacial event in the Pliocene at 3.3 Ma (M2), the amplitude in both the carbon and oxygen isotope signal increase on time scales of 10^5 years.

Rhythms: The main contribution of the current study is to reveal the general patterns of rhythmic fluctuations as superposed on the long-term trends. Fluctuations on time scales of 10^4 to 10^5 years dominate early-mid Cenozoic global oxygen and carbon isotope records (the blue curve in Fig. 1) and are related to the short eccentricity oscillations of about 95,000, 124,000 and 405,000 years, more distinctive in the carbon isotope record (Fig. 3). The influence of eccentricity on insolation are small compared to those of obliquity and precession, but it is the only orbital parameter that controls the total amount of solar radiation received by the Earth averaged over the course of one year (*14*). More importantly, eccentricity modulates the amplitude of the precession cycle affecting the intensity of seasons (e.g., during maxima in eccentricity, more intense wet and dry seasons caused a decrease in the net burial of carbon) (*30*). Modeling suggests that low- and mid- latitude processes in the climate system respond in a nonlinear way to insolation forcing (*28, 31-33*). Important feedback to be considered involves the global monsoon which plays a key role in distributing moisture and energy as driven by low-latitude insolation (*31, 32*). The high-resolution isotope record thus documents a nearly 50-million-year sustained dominance of low-latitude processes on Earth's climate system.

After the mMCT at 13.9 Ma, Earth's climatic regime and dynamic response changed with the re-expansion of Antarctic ice sheets and possible initiation of Northern Hemisphere Ice

Sheets (NHIS) in the late Miocene (*110*). After that time, a persistent response to obliquity gains power in the oxygen isotope signal, further strengthening after 7.7 Ma (Fig. 3; *22*, *36*), documenting the increasing influence of high latitudes on global climate variability caused by the expansion of polar ice-sheets. In contrast, carbon cycle dynamics remain strongly paced by eccentricity after the mMCT (*36, 67*), but obliquity only noticeably imprints on carbon isotope variability after 7.7 Ma before becoming the dominant influence in both oxygen and carbon isotopes after 6.4 Ma (*11, 22, 114*) (Fig. 3). About 800,000 years ago, the amplitude in oxygen isotope data, now showing a characteristic asymmetric pattern, increased due to the waxing and waning of large Northern Hemisphere ice sheets. The origin of the prevailing quasi 100-kyr cycle of the ice age is still an unsolved problem, but it is likely not directly related to the 95-kyr and 124-kyr eccentricity cycle. However, from the perspective of the last 66 Myr, the past 800,000 years represent a very unusual time with its asymmetric large scale amplitude fluctuations in oxygen isotope values due to the waxing and waning of massive bipolar ice-sheets.

Aberrations: Aberrations from the background global trends and rhythms are the third important feature of the Cenozoic deep-sea benthic carbon and oxygen isotope record. Transient climate warming events lasting 40-kyr to 200-kyr occurred frequently in the late Paleocene and early Eocene. Known as hyperthermal events, they are characteristically coupled to negative excursions in carbon and oxygen isotope values, which document rapid warming of the climate system on geological time scales associated with large perturbations of the carbon cycle (*4, 16, 39, 115*). By far the largest event, unprecedented in the last 100 million years, was the 5 to 8°C global warming of the Paleocene/Eocene Thermal Maximum (PETM) at ~56 Ma. It is evident that hyperthermals are orbitally forced disruptions in the carbon cycle (*39, 115, 116*) with infrequent and variable additional carbon released from slowly recharging reservoirs (*117*). These transient global warming events are an intrinsic feature of the climate system in the "hothouse mode" as is apparent in the early Eocene. After the East Antarctic Ice Sheet expansion at the EOT at ~34 Ma ago, only the Tortonian Thermal Maximum at 10.75 Ma (*36*) stands out as a potential similar warming event, but its global nature needs to be validated by additional records. High-amplitude variability of $\delta^{18}O$ and $\delta^{13}C$ during the Miocene Climate Optimum is reminiscent of hyperthermals ($\delta^{18}O$ and $\delta^{13}C$ decreases coupled to intense transient carbonate dissolution events). If we assume that pCO_2 level reconstructions around 600 ppm for that time are correct, the climatic implications are major. The detailed isotope record of the Cenozoic encompasses many more anomalies, but of lower magnitude than those discussed above. Many of these were very likely orbitally controlled dynamics in the climate system enhanced by non-linear effects (*30*).

S2 - Milankovitch cycles and astronomical tuning

Periodic variations in Earth's orbit around the Sun have remained relatively uniform over hundreds of millions of years. However, the climatic response to resulting changes in insolation have varied considerably (*1, 69, 106*). Average global temperature over millions of years mostly varied in concert with the concentration of greenhouse gases such as atmospheric CO_2 (*118*). Superposed on the long-term trends, fluctuations omnipresent in deep-sea benthic foraminifer isotope data are driven by variations in Earth's orbital parameters (*119*) with periodicities corresponding to the so-called Milankovitch cycles of precession (19 and 23 kyr), obliquity (41 kyr) and eccentricity (100 and 405 kyr). These cycles are the key quasi-periodic climate influencing changes in Earth's orbital geometry caused by the gravitational interaction of larger

bodies in the Solar System (*69*). Although the expression of these cycles in sediments can change with time the heartbeat of climate, the Milankovitch cycles, can be used as a metronome telling time. Such astronomical tuning, the correlation of Milankovitch cycles in sediment archives to numerical computations of insolation is now a cornerstone calibrating the geological time scale (*66*), and central to the contribution of this study.

S3 - Sampling resolution and site location artefacts

We have addressed the sampling biases of the CENOGRID already above. Here we elaborate on the limits and possible artefacts arising from the selection of ocean drilling sites. Sedimentary records are a mix of local, regional and global signals and their interactions. Deep-sea and far offshore ocean drilling records are good records to investigate global changes, as proven in 50 years of scientific ocean drilling. However, on time scales of ten thousand to one million years specific locations are better suited for resolving the higher frequency components of climate variability, in part, because of proximity to certain climate system processes (circulation/weathering). Just as an example, the Ceara Rise (ODP Leg 154) sites with relatively high sedimentation rates for a pelagic region and a location in the western Equatorial Atlantic (i.e., relative to the boundary between Antarctic Bottom Water and Northern Component Water) should record both obliquity and precession. Oligocene-early Miocene records from the eastern South Atlantic Walvis Ridge might not be as sensitive to obliquity (for discussion see (*120*)). How much of the signal in the Oligocene-early Miocene Site 1264 $\delta^{18}O$ or $\delta^{13}C$ is local versus global is debatable and can only be assessed with high fidelity records from multiple other sites from different regions and water depths (e.g. (*121*)). Stratigraphically continuous and splices composite scientific ocean drill cores are still rare. It will take another 50 years of scientific ocean drilling to systematically retrieve suitable records and generate high-resolution benthic stable isotope records needed to clearly disentangle regional from global signals as well as regional from global responses to astronomical forcing.

Due to the limited selection of currently available cores the results in our study will be biased towards the particular record used from Atlantic or Pacific. We are confident that the selected records still for the most part mainly reflect a global signal due to their well-connected/ventilated positions within vast ocean regions and high resolution expression of variability mirrored in other records. For the records in CENOGRID, we chose to apply a minimal tuning approach to avoid introduction of precession or obliquity components into the records prior to spectral analysis. The selection of mid- to low-latitude sites could bias the records as well as their position in the water column and thus the origin of the signal recorded. Benthic $\delta^{18}O$ values mainly tell about the climate (temperature) in the areas of deep-water formation (e.g., the high latitudes) and change in seawater isotope composition by ice sheet variations. Benthic $\delta^{13}C$ values are more complex, they mostly reflect the dissolved inorganic carbon inventory of the ocean and are influenced by the ocean circulation patterns. Records will thus be biased depending on their geographic position and influence the outcome of the spectral analysis. Thus artefacts can arise from changing between records. Additionally, the sample resolution (Fig. 28) and sedimentation rate at a given location will bias the outcome. Slow sedimentation rates of much less than 1 cm/kyr tend to amalgamate precession and obliquity related cycles, enhance the amplitude of longer cycles like eccentricity, and potentially lead to cycle misidentification. We use the best resolved records in the CENOGRID to avoid aliased signals or amplitude enhancement.

Different approaches for time series analysis to produce evolutive spectrograms exist. We applied various methods to avoid misinterpretation by method based artefacts. The Evolutive Power Spectral Analysis (Fig. S29) and the evolutionary FFT spectrogram (Fig. 3) give similar results but tend to smear out at significant power intervals. Wavelets generally perform better in identifying brief intervals with significant cyclicity, because this time series analysis tool adjusts window size for each periodicity. We computed 3D wavelets on CENOGRID (Fig. 29), which show a bit more detailed but consistent pattern compared to the Evolutive Power Spectral Analysis and evolutionary FFT spectrogram. The enhanced persistent appearance of obliquity cycles at around 13.9 Ma in $\delta^{18}O$ and 7.7 Ma in $\delta^{13}C$ can be seen in the 3D wavelets as well. These analyses are consistent with findings at multiple locations in different oceanic basins that pervasive obliquity pacing is imprinted in benthic oxygen and carbon isotopic records since the late Miocene to early Pliocene. A similar picture evolved using the Thomson multi-taper method (MTM, (122), Fig. S31). The latter method reveals in $\delta^{18}O$ data some more power in the obliquity band around 14.5 Ma, 19.5 Ma, 21 Ma, 23.7 Ma, 30.5 Ma, and 43 Ma. All of these intervals are characterized by low eccentricity modulation of the precession and larger obliquity amplitudes in the astronomical forcing. Higher power intervals in the obliquity band at 56 Ma (Paleocene/Eocene Thermal Maximum) and the Early Eocene Climate Optimum (EECO, 49.14 to 53.26 Ma) are an artifact of the hyperthermal events (*16*). The weak response to obliquity in the early Cenozoic could be partly biased by the selection of sites. Enhanced obliquity cyclicity was reported during the Oligocene from the Pacific ODP Site 1218 (*35*) in benthic stable isotope data, the early Miocene and Oligocene from Southern Ocean ODP Site 1090 (*123*) and Atlantic Ceara Rise ODP Leg 154 sites (*124-128*) in magnetic susceptibility and benthic stable isotope data. In our study we have revised the astronomical tuning for ODP Site 1218 using a minimal tuning approach. Spectral analysis of the benthic data on the new age model reveals less obliquity contribution than previously thought. Higher resolved benthic records spanning the early Miocene and late Oligocene from ODP Site 1264 (Walvis Ridge, (*120*)) and ODP Site U1334 (*121)* show less imprint of obliquity related cyclicity then the previous lower resolution record. We point out here that more detailed records spanning all intervals of the Cenozoic Era are needed to properly resolve the detailed response to astronomical forcing. Low amplitude variability will make this a challenging task for most of the Cenozoic, but we strongly recommend here to generate records at high resolution (2-3 kyr) and on monospecific species to avoid aliasing and distortion of the primary isotope signal.

S4 - Evolution of Earth's global temperature and its coupling to atmospheric CO_2 changes

Since the industrial revolution in the 1850s atmospheric CO_2 concentrations have risen as a result of anthropogenic carbon (C) emission due to fossil-fuel burning and net land use (*129*). At present, concentrations have increased to 415 ppm or by 40% relative to pre-industrial times, and depending on future fossil fuel (FF) consumption will rise following one of several potential C trajectories, or Representative Concentration Pathways (RCP). The response of future climate to anthropogenic carbon release, however, still has a large degree of uncertainty due to the nonlinear behavior of feedbacks in climate models, for example clouds. This is particularly true for scenarios of CO_2 levels exceeding those of the last several million years (~400 ppm) which are closer to the early Eocene levels (>800 ppm). Although reconstructions of deep time climate states and their associated dynamics, cannot be used as direct analogs for future climate due to different climate boundary conditions (e.g., configuration of continents and mountain ranges,

etc.), they can be used to assess climate model sensitivity, and thus test hypotheses about feedback mechanisms.

After removing the contribution of large polar ice-sheets, deep-sea benthic foraminifer oxygen isotope data essentially track mean deep-sea temperature over the Cenozoic (*1*) which can be transferred into average global changes in surface air temperature by scaling to the 1961–1990 average (Fig. S34; (*92*)). Over the same period atmospheric CO_2 levels can be reconstructed by a variety of methods (*130*). Assuming that atmospheric CO_2 concentrations mainly pace Cenozoic climate (*131-133*) a comparison of the RCP results to the average global temperature changes derived from the high-resolution benthic foraminifer record helps to (A) identify periods in Earth's history that are comparable to future scenarios and (B) unravel how dynamic climate evolves in these modes.

At 415 ppm, present day CO_2 levels are similar to those of the middle Pliocene (Fig. S34; (*134*)), before the establishment of a large Northern Hemisphere ice sheet (NHIS). By the year 2100 atmospheric CO_2 could reach 935 ppm, possibly causing a global warming of more than 4° Celsius according to RCP 8.5 (Fig. 31, (*44*)). The Miocene Climate Optimum, more than 15 million years ago, is the most recent period in the Earth's past with similar temperature increase relative to preindustrial (1961-1990), a time with insignificant NHIS and dynamic Antarctic Ice Sheets (e.g. (*135-138*)). If there is no considerable decrease in carbon emissions by the year 2200, atmospheric CO_2 could reach almost 2000 ppm, likely causing a warming of more than 8°C by the year 2300 (*44, 139*). The Earth was as warm during the middle to late Eocene (>40 Ma) and mid-Paleocene (~60 Ma) (Fig.31, (*44*)), a time of no significant polar ice-sheets and CO_2 level much higher than today (*133*). During the EOT, 34 Ma ago, the massive expansion of the Antarctic ice sheet is thought to be related to a CO_2 threshold for the establishment of continental ice sheets (~600 ppm; (*140-142*)). Even under the caution that past climates may not be direct analogues to Earth's short term future, because of non-linearities in forcing and feedbacks of the climate system (*143, 144*), under further unmitigated emissions of CO_2 there is a risk of pushing the climate system towards a state with ephemeral glaciations at the poles, where the climate system will lose a key thermostat and the influence of low-latitude processes on global climate will be strengthened. As is apparent in long-term detailed reconstructions such a major shift between states in climate would be unique in the past 66 Mya. While there have been similar magnitude warming events (e.g., the PETM), the main difference is that during these past events, the planet was already warm and ice-free, so lacking a major amplifying feedback on the climate system. Moreover, despite state, carbon cycle feedbacks have operated to varying degrees. As such, it is very likely that the rate and impacts of future warming will be severe and exceedingly challenging to forecast.

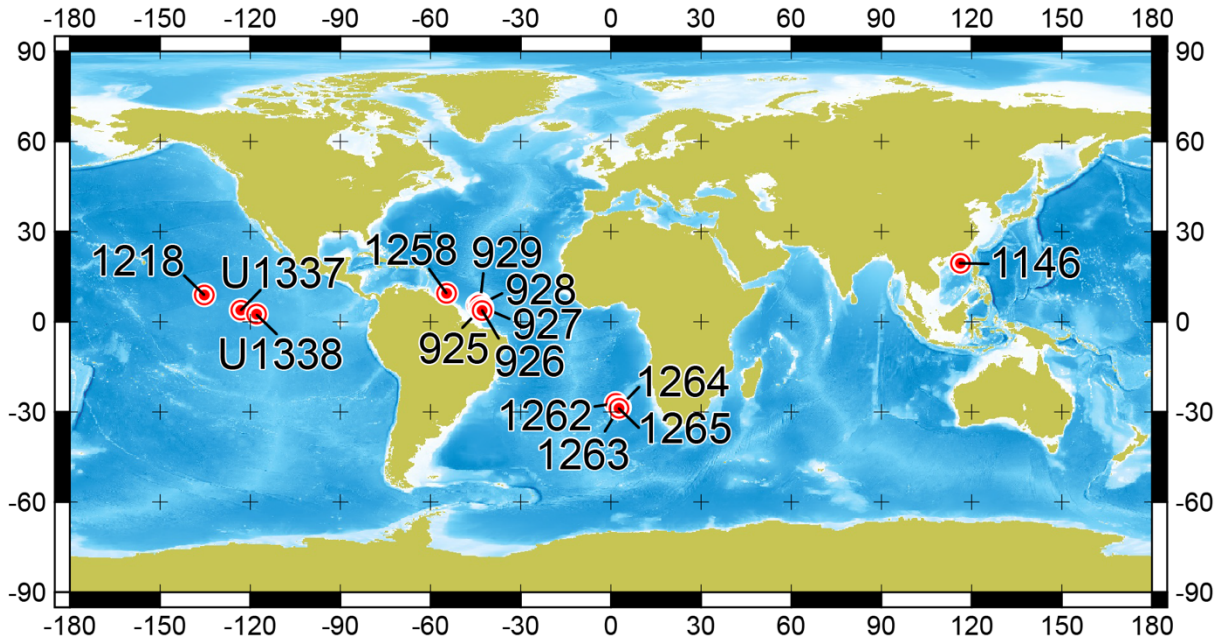

Fig. S1.

Location of ocean drilling sediment cores used to form the Cenozoic high-fidelity benthic stable isotope reference splice.

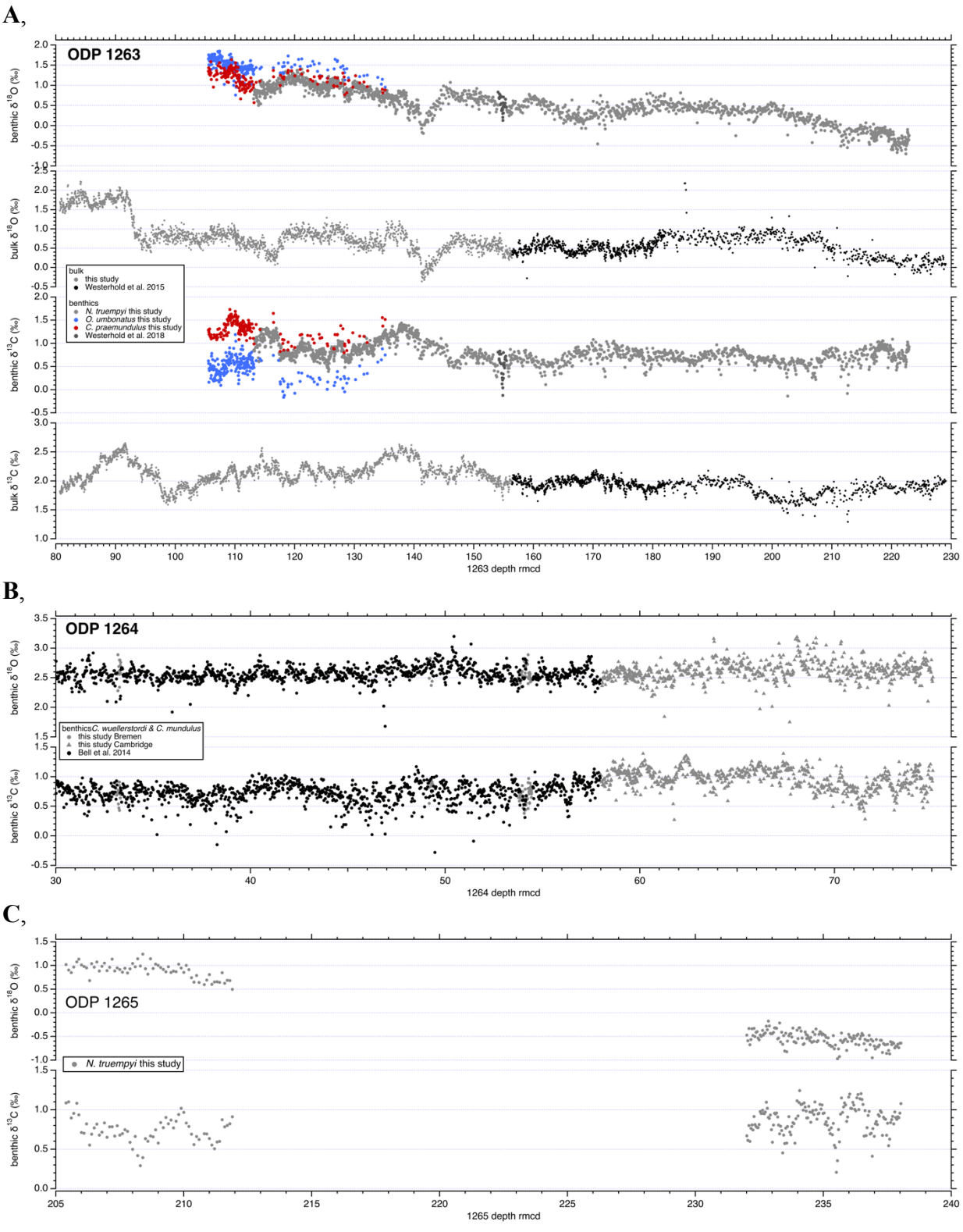

Fig. S2.

Bulk carbonate and benthic foraminifer stable carbon and oxygen isotope data for ODP Sites 1263 (A), 1264 (B) and 1265 (C) plotted versus revised meters composite depth (rmcd).

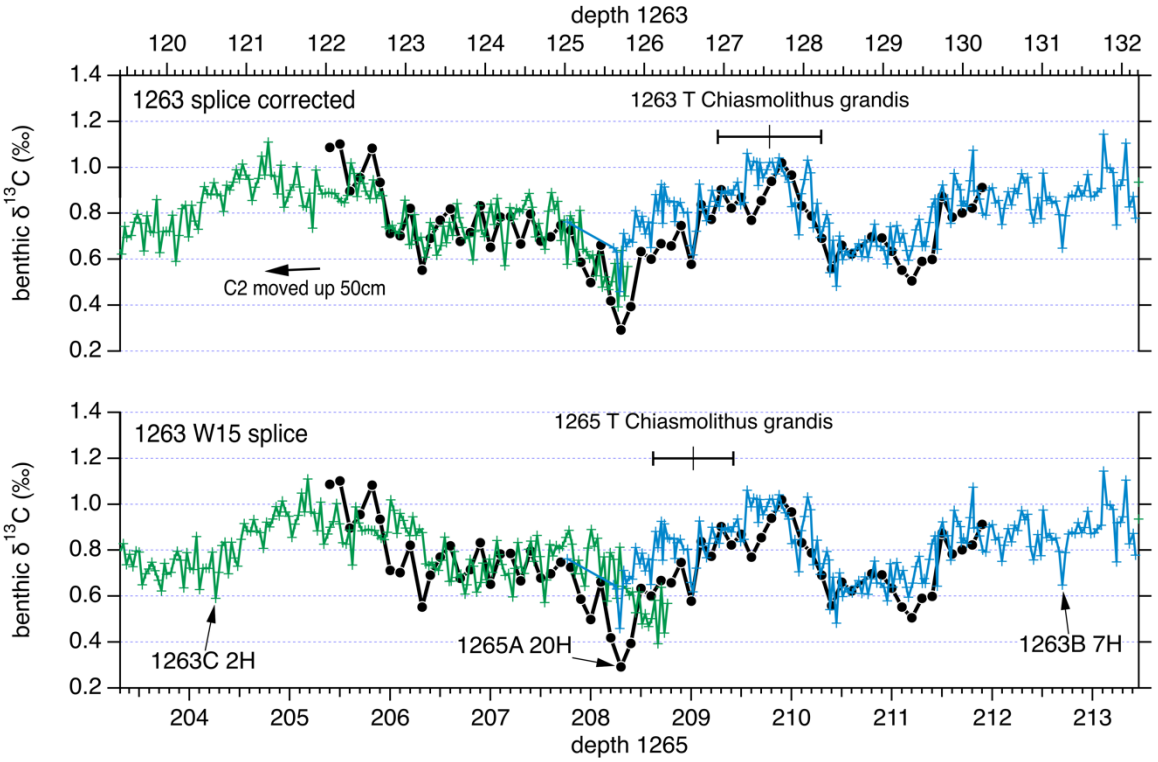

Fig. S3.

Benthic foraminifer carbon isotope data (*N. truempyi*) from ODP Sites 1263 and 1265 to illustrate the correction of the composite drill core depth at Site 1263. Isotope data from Cores 1263C-2H (green) and 1263B-7H (blue) plotted versus depth for Site 1263 (upper x-axis), and for Core 1265A-20H (black) plotted versus depth for Site 1265 (lower x-axis). The lower panel shows the data plotted on the (*47*) (W15) composite depth for Site 1263, the upper panel shows the corrected composite depth for Site 1263 presented in this study. Comparison with the equivalent interval from Site 1265 validates the correction of the composite depth at Site 1263 by moving Core 1263C2H upward by 50cm. The nannofossil event datum of Top *Chiasmolithus grandis* at Sites 1263 and 1265 is given to back-up the correlation between both sites.

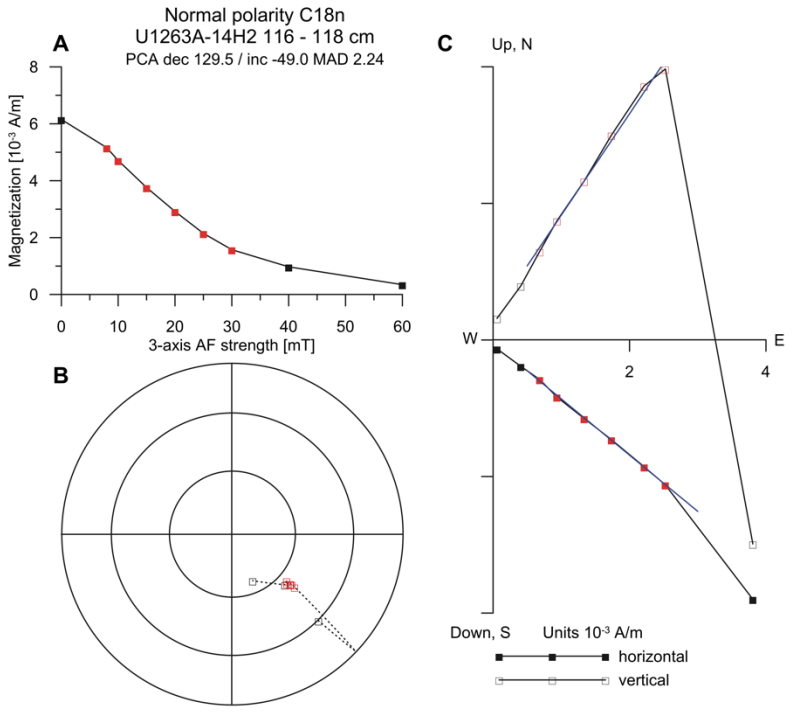

Fig. S4.

Natural remanent magnetization (NRM) data from the 0 to 60 mT AF peak field demagnetization interval for sample U1263A-14H2, 116-118 cm from normal magnetic polarity Chron C18n: (A) intensity of magnetization versus AF peak field; (B) stereographic projection of vector end-points with declination plotted on the circles (N at the top, E to the right) and inclination plotted on the radius (0° on the outer circle; 90° in the center); filled (open) symbols mark data on the upper (lower) hemisphere; (C) orthogonal projections of NRM component data; open (filled) symbols represent projection of vector end-points on the vertical (horizontal) plane; blue lines indicate direction of characteristic remanent magnetization (ChRM).

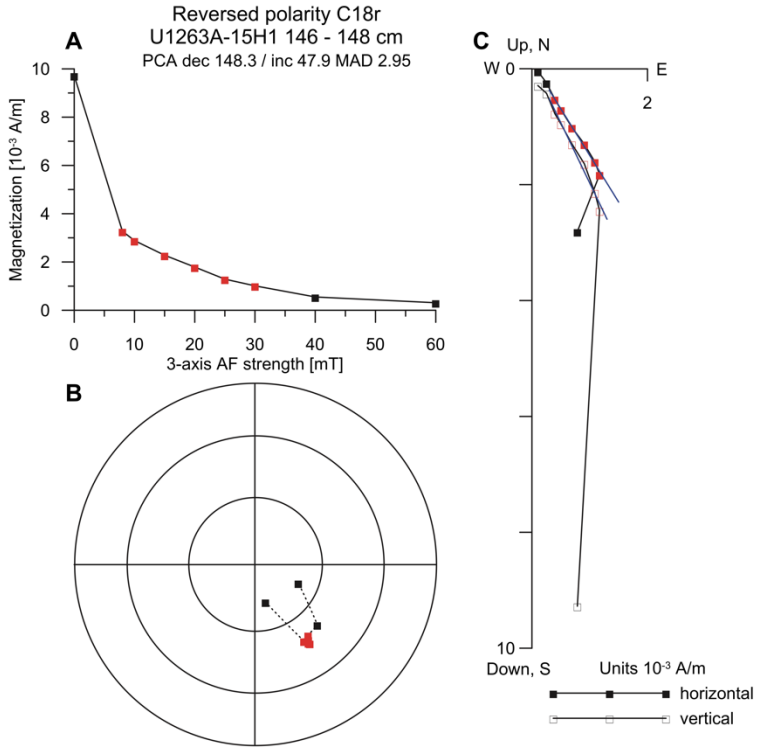

Fig. S5.

Natural remanent magnetization (NRM) data from the 0 to 60 mT AF peak field demagnetization interval for sample U1263A-15H1, 146-148 cm from reversed magnetic polarity Chron C18r: (A) intensity of magnetization versus AF peak field; (B) stereographic projection of vector end-points with declination plotted on the circles (N at the top, E to the right) and inclination plotted on the radius (0° on the outer circle; 90° in the center); filled (open) symbols mark data on the upper (lower) hemisphere; (C) orthogonal projections of NRM component data; open (filled) symbols represent projection of vector end-points on the vertical (horizontal) plane; blue lines indicate direction of characteristic remanent magnetization (ChRM).

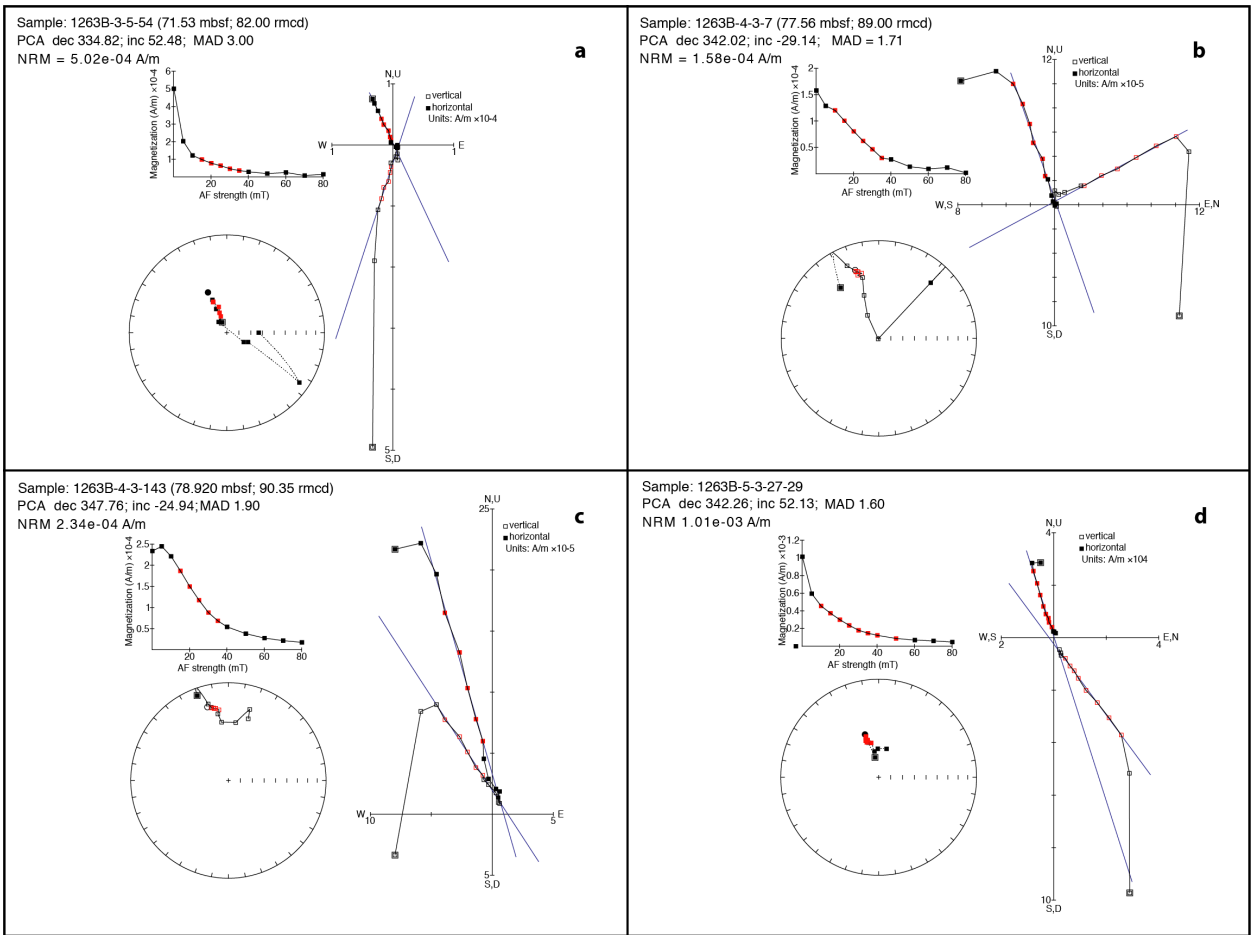

Fig. S6.

AF demagnetization behavior for representative samples from Hole 1263 B. For the vector component diagrams, open (closed) symbols represent projections onto the vertical (horizontal) plane. The blue lines represent linear regression fits that indicate the ChRM direction for each sample. The stereo plots are equal-area stereographic projections, with solid (open) symbols representing points projected onto the lower (upper) hemisphere. Plots were produced using PuffinPlot (*59*).

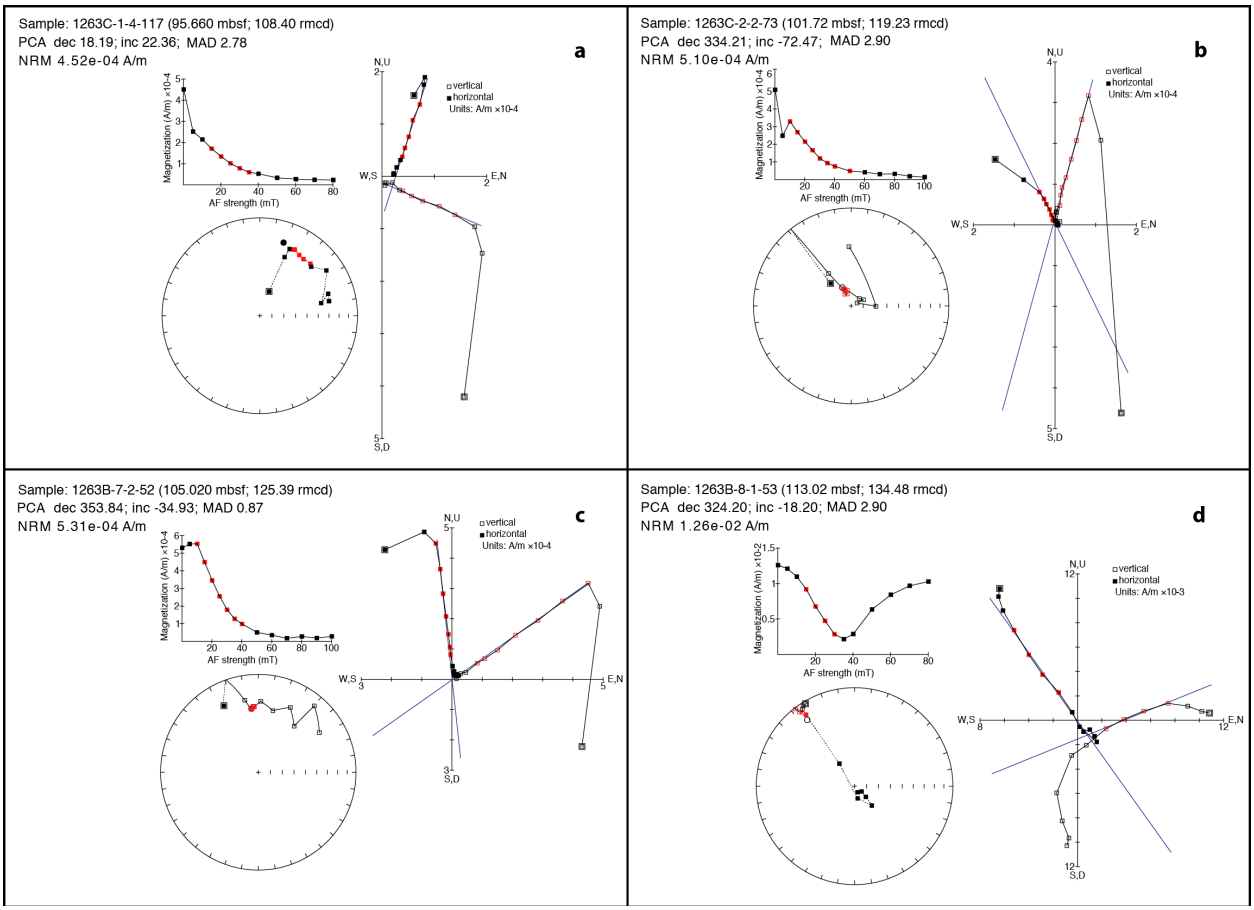

Fig. S7.

AF demagnetization behavior for representative samples from Hole 1263 B and C. For the vector component diagrams, open (closed) symbols represent projections onto the vertical (horizontal) plane. The blue lines represent linear regression fits that indicate the ChRM direction for each sample. The stereo plots are equal-area stereographic projections, with solid (open) symbols representing points projected onto the lower (upper) hemisphere. Plots were produced using PuffinPlot (*59*).

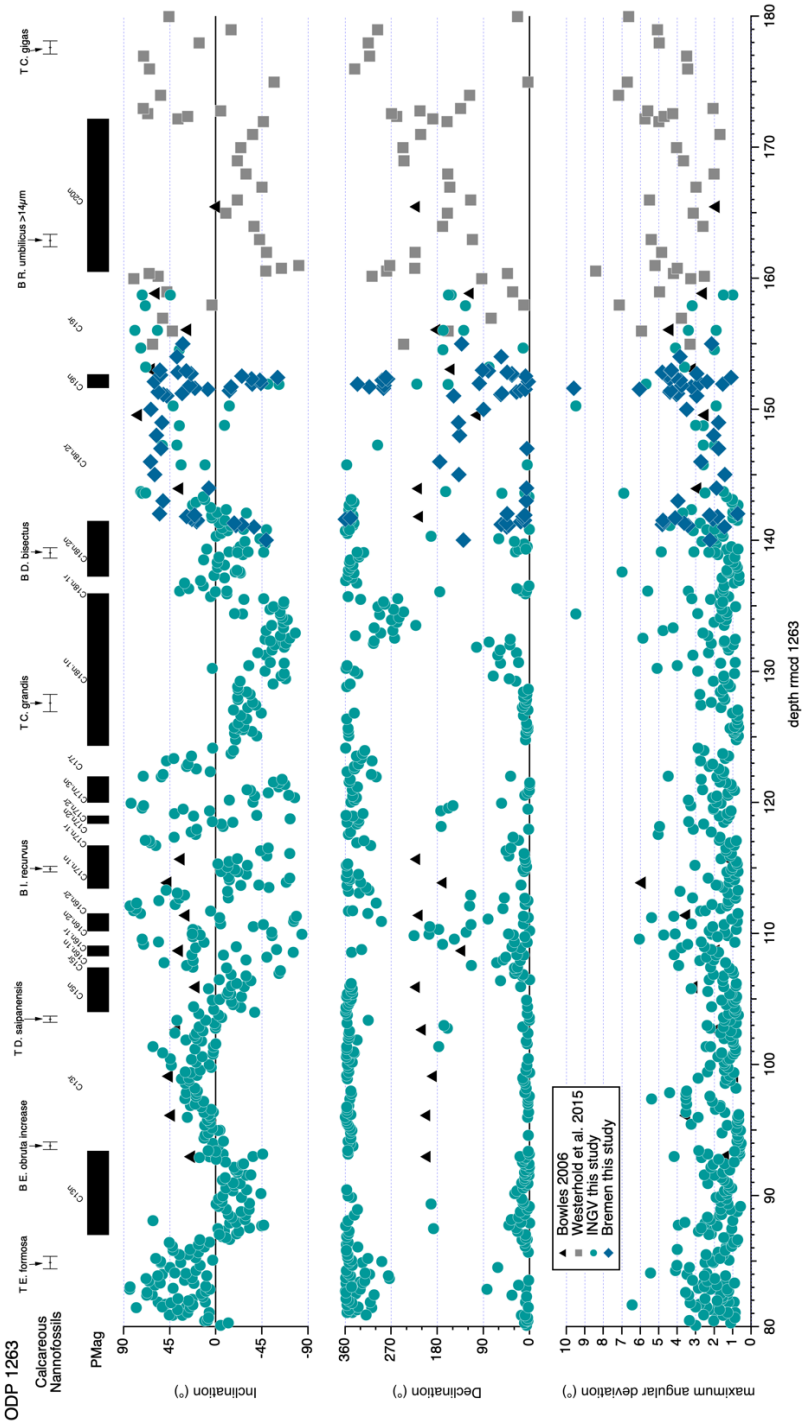

Fig. S8.

Overview of characteristic remanent magnetization results and data versus depth at Site 1263. Maximum angular deviation (MAD), declination and inclination results of discrete samples as well as the final magnetostratigraphic interpretation applying calcareous nannofossil datums.

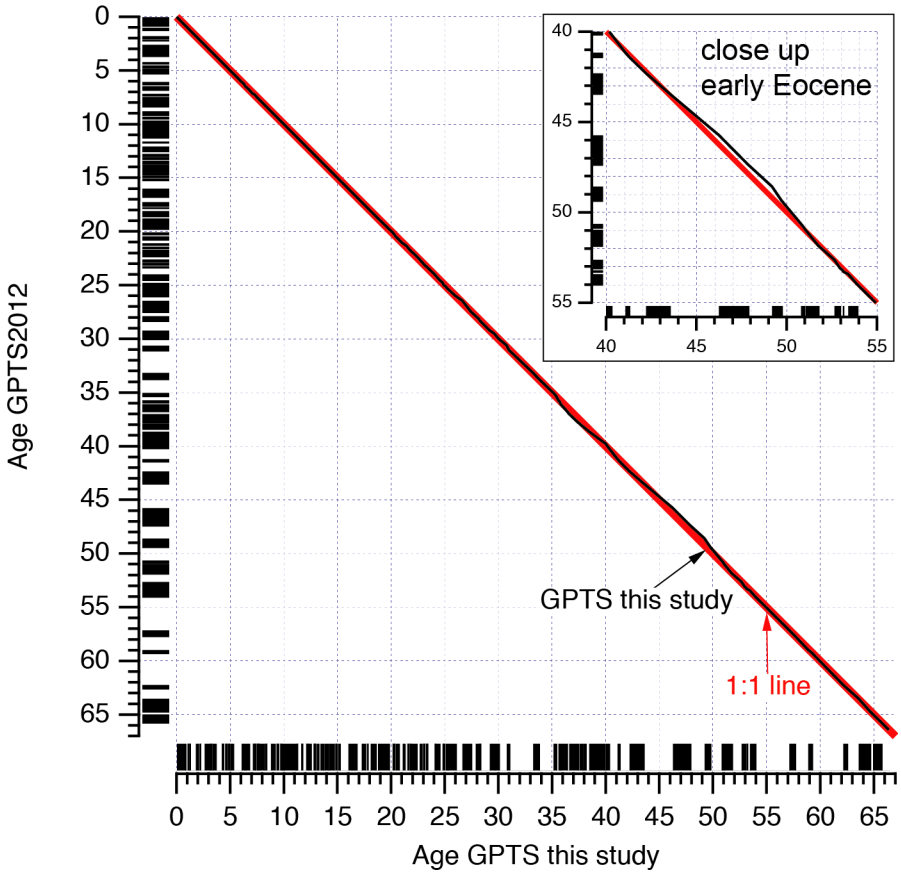

Fig. S9.

Comparison of magnetochron boundary ages between GPTS2012 (*60*) and astronomically tuned ages compiled from ocean drilling sediment cores (this study).

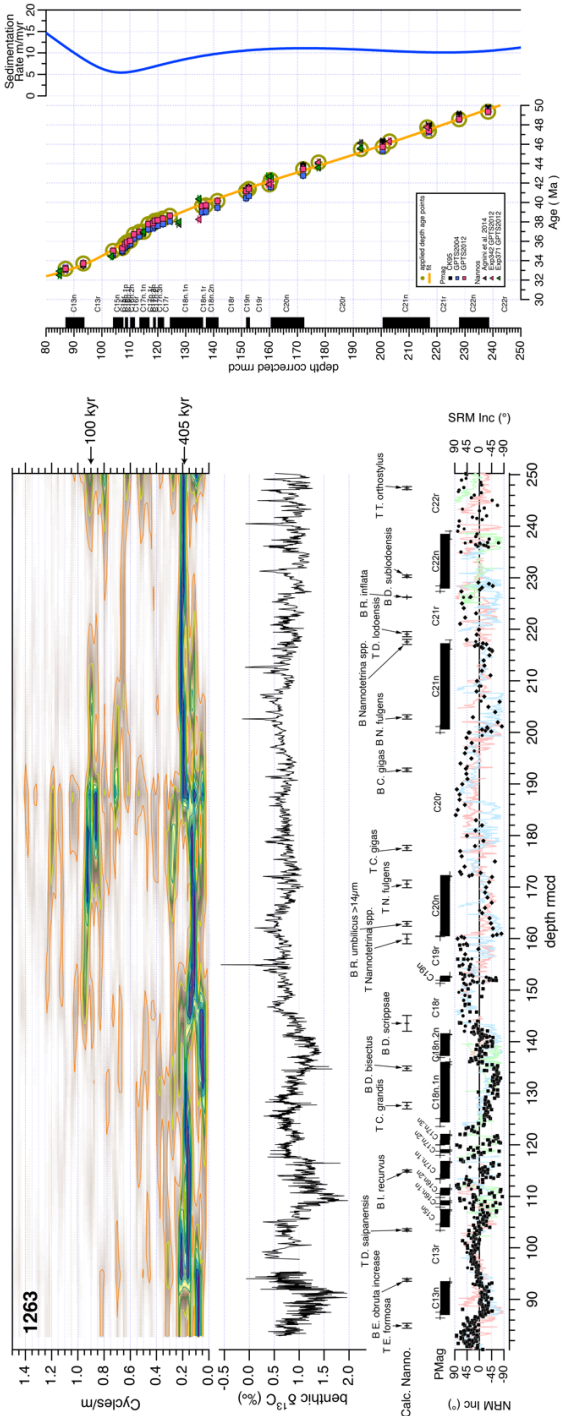

Fig. S10.

Spectral analysis of middle to late Eocene benthic foraminifer carbon isotope data plotted versus depth at Site 1263. Based on the calcareous nannofossil biostratigraphy and the magnetostratigraphy, sedimentation rates can be estimated showing that the dominant cycles with frequency of 0.2 cycles/meter (5 m-long cycles) are related to the 405 kyr eccentricity cycle. Shorter cycles in the order of 0.8 cycles/meter (1.25 m-long cycles) are related to short eccentricity.

Fig. S11. – oversized figure

Astronomical tuning of bulk and benthic foraminifer carbon isotope data from Sites 1258, 1262, 1263 and 1265 spanning the Paleocene and Eocene. For orientation, inclination data with magnetostratigraphic interpretation and calcareous nannofossil event datums are plotted along all available bulk and benthic carbon isotope data versus depth. The published age model for Sites 1262 (Tab. S28) and 1263 (Tab. S29) have been extended in this study from 32.7 to 41.9 Ma at Site 1263 to develop a complete astrochronology for the Paleocene and Eocene. Outstanding events (transitions, hyperthermals, boundaries) are indicated. Target for astronomical tuning was the numerical solution La2010b for eccentricity from (*14*). In the top panel the La2010b solution is plotted with the detrended carbon isotope data to document the good agreement between data and model with respect to the amplitude modulation of short eccentricity.

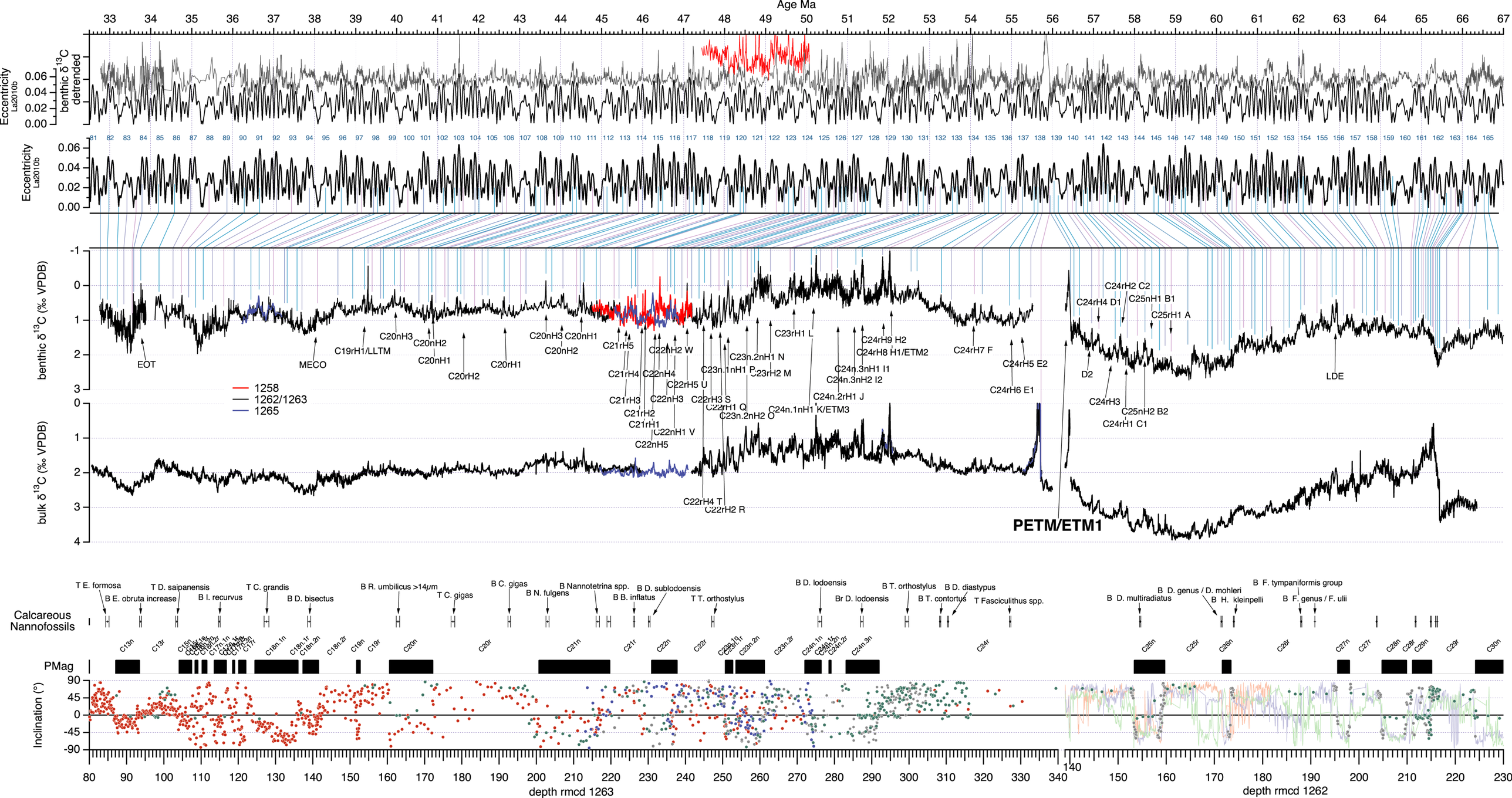
Age Ma
Eccentricity La2010b
benthic δ13C detrended
benthic δ13C (‰ VPDB)
bulk δ13C (‰ VPDB)
1258
1262/1263
1265
EOT
MECO
C19rH1/LLTM
C20nH3
C20nH2
C20nH1
C20rH2
C20rH1
C21rH5
C22nH2 W
C21rH4
C22nH4
C22rH5 U
C21rH3
C22nH3
C22rH3 S
C21rH2
C22rH1 Q
C21rH1
C22nH1 V
C22nH5
C22rH4 T
C22rH2 R
C23n.2nH1 N
C23n.1nH1 P
C23rH2 M
C23n.2nH2 O
C23rH1 L
C24n.1nH1 K/ETM3
C24n.2rH1 J
C24n.3nH1 I1
C24n.3nH2 I2
C24rH9 H2
C24rH8 H1/ETM2
C24rH7 F
C24rH6 E1
C24rH5 E2
C24rH4 D1
C24rH2 C2
C25nH1 B1
C25rH1 A
D2
C24rH3
C25nH2 B2
C24rH1 C1
LDE
PETM/ETM1
Calcareous Nannofossils
T E. formosa
B E. obruta increase
T D. saipanensis
B I. recurvus
T C. grandis
B D. bisectus
B R. umbilicus >14μm
T C. gigas
B C. gigas
B N. fulgens
B Nannotetrina spp.
B B. inflatus
B D. sublodoensis
T T. orthostylus
B D. lodoensis
Br D. lodoensis
B T. orthostylus
B T. contortus
B D. diastypus
T Fasciculithus spp.
B D. multiradiatus
B D. genus / D. mohleri
B H. kleinpelli
B F. tympaniformis group
B F. genus / F. ulii
PMag
Inclination (°)
depth rmcd 1263
depth rmcd 1262

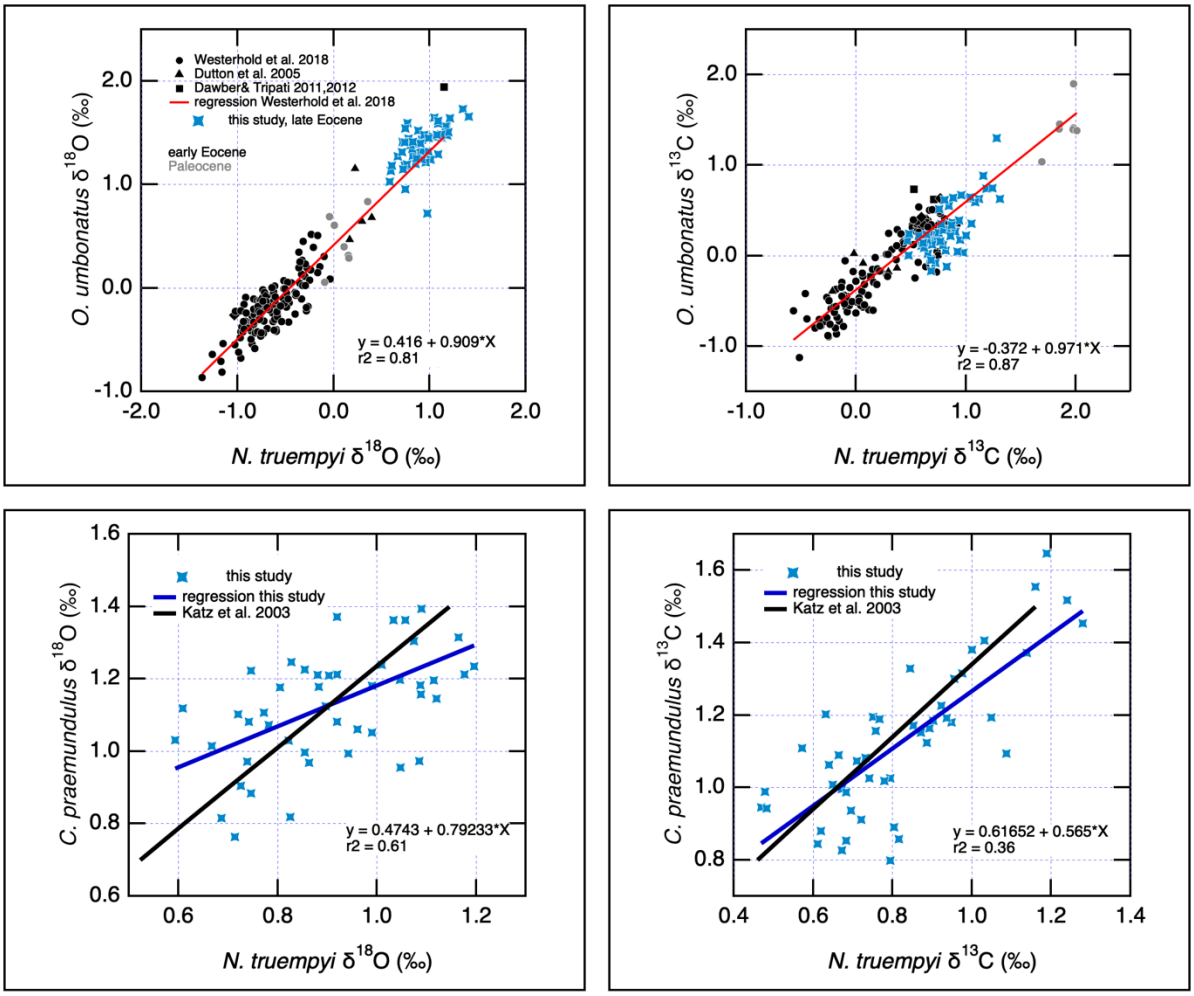

Fig. S12.

Paired isotope analysis of benthic foraminifers *N. truempyi*, *O. umbonatus*, and *C. praemundulus* for (left) $\delta^{18}O$ and (right) $\delta^{13}C$. Paleocene, gray; Eocene, black; Eocene this study in dark red. The light red linear regression line for $\delta^{18}O$ and $\delta^{13}C$ paired analysis of *N. truempyi*, and *O. umbonatus* (*16*) include data from (*16, 145-147*) to establish the isotopic adjustment (i.e., correction) factor for benthic foraminifers from Site 1209. The 1263 data from our study of the late Eocene fall on the established regression line from Site 1209. $\delta^{18}O$ and $\delta^{13}C$ paired analysis of *N. truempyi* and *C. praemundulus* provide a regression line to adjust between the species. See Tab. S2 for details on correction factors used in this study.

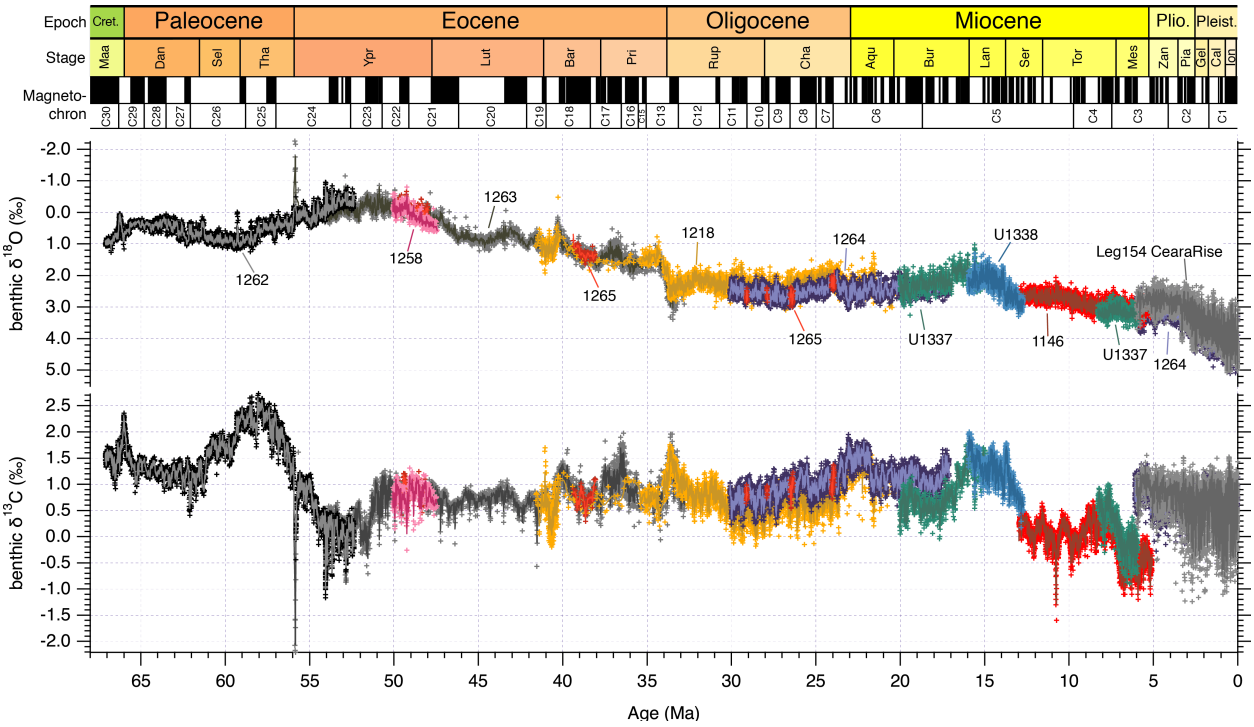

Fig. S13.

Complete benthic foraminifer stable carbon and oxygen isotope records and 10-point LOESS smooth on astrochronology used for building the Cenozoic reference splice.

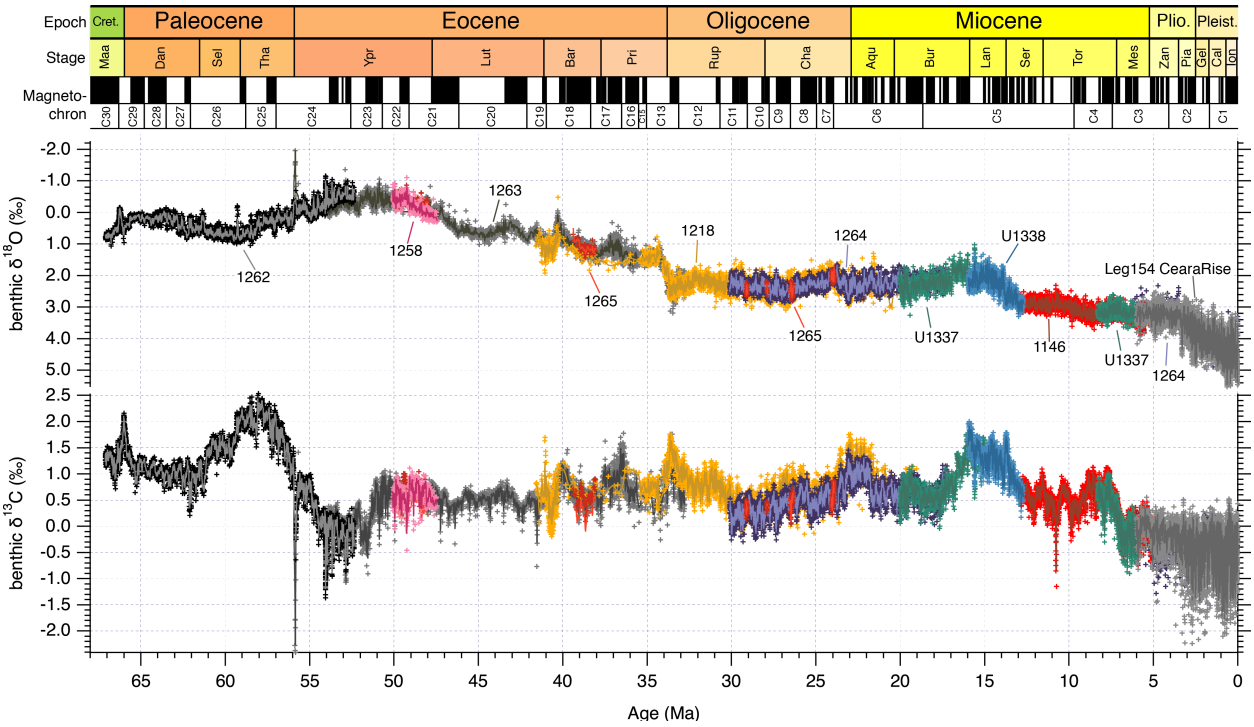

Fig. S14.

Benthic foraminifer stable carbon and oxygen isotope records and 10-point LOESS smooth on an astrochronological timescale used to build the Cenozoic reference splice. $\delta^{18}O$ and $\delta^{13}C$ values of the records are offset as given in Tab. S4 to get rid of interbasin offsets to form a continuous record without offsets due to switches between different records.

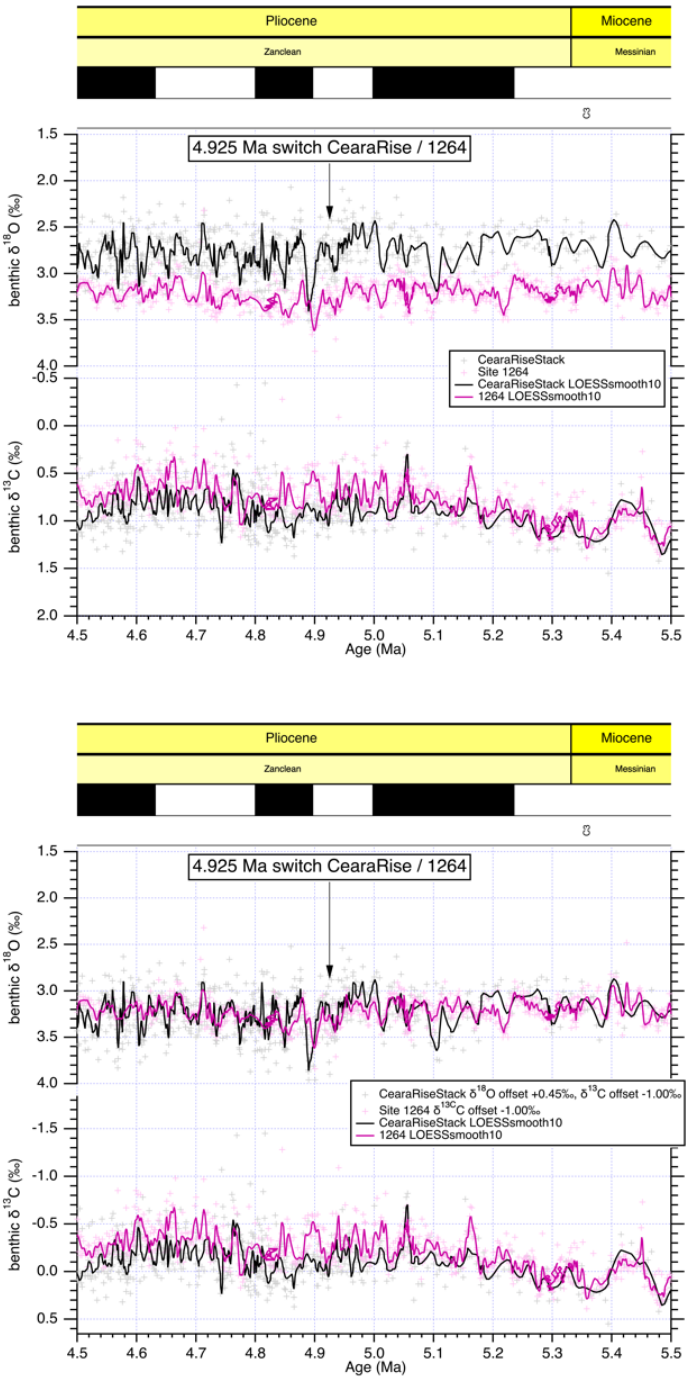

Fig. S15.

Switch at 4.925 Ma from Ceara Rise Stack to Site 1264. Top: benthic $\delta^{13}C$ and $\delta^{18}O$ raw data. Bottom: benthic data with offset for Ceara Rise and Site 1264 spanning 4.5 to 5.5 Ma across reference record switch at 4.925 Ma.

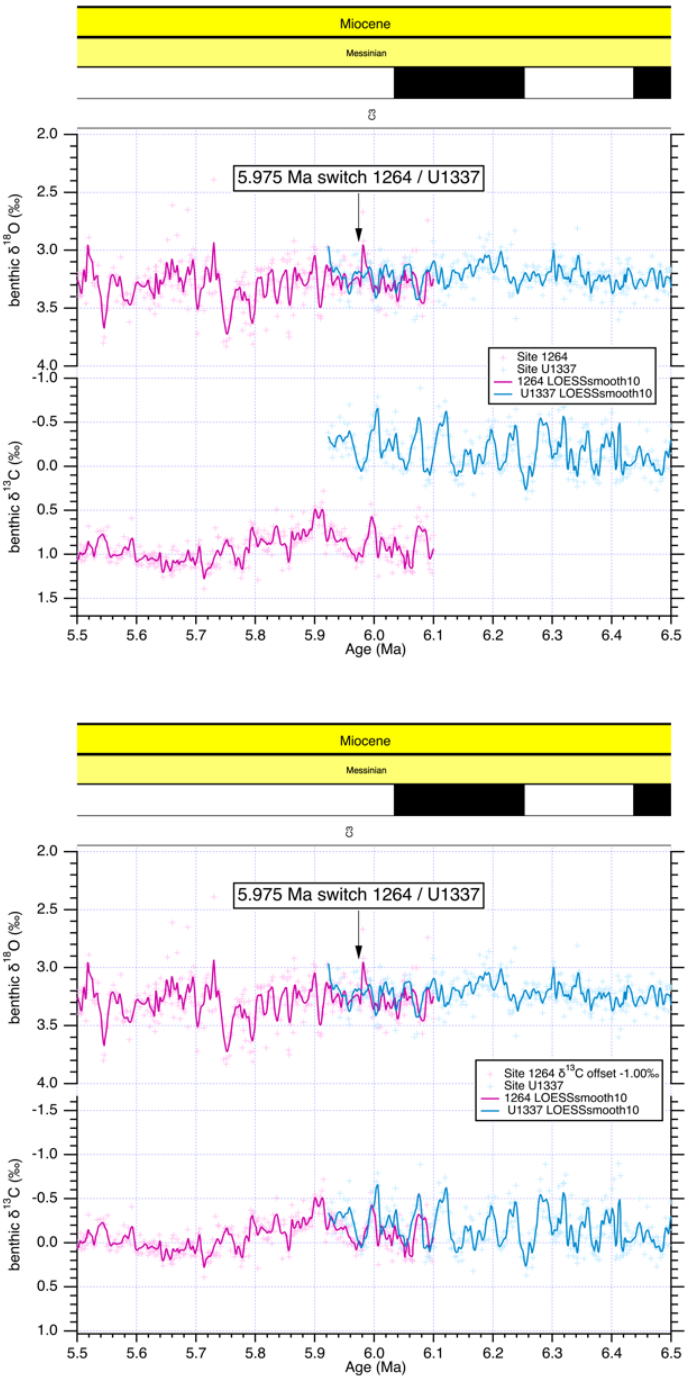

Fig. S16.

Switch at 5.975 Ma from Site 1264 to Site U1337. Top: benthic foraminifer $\delta^{13}C$ and $\delta^{18}O$ raw data. Bottom: benthic data with offset for Site 1264 and Site U1337 spanning 5.5 to 6.5 Ma across reference record switch at 5.975 Ma.

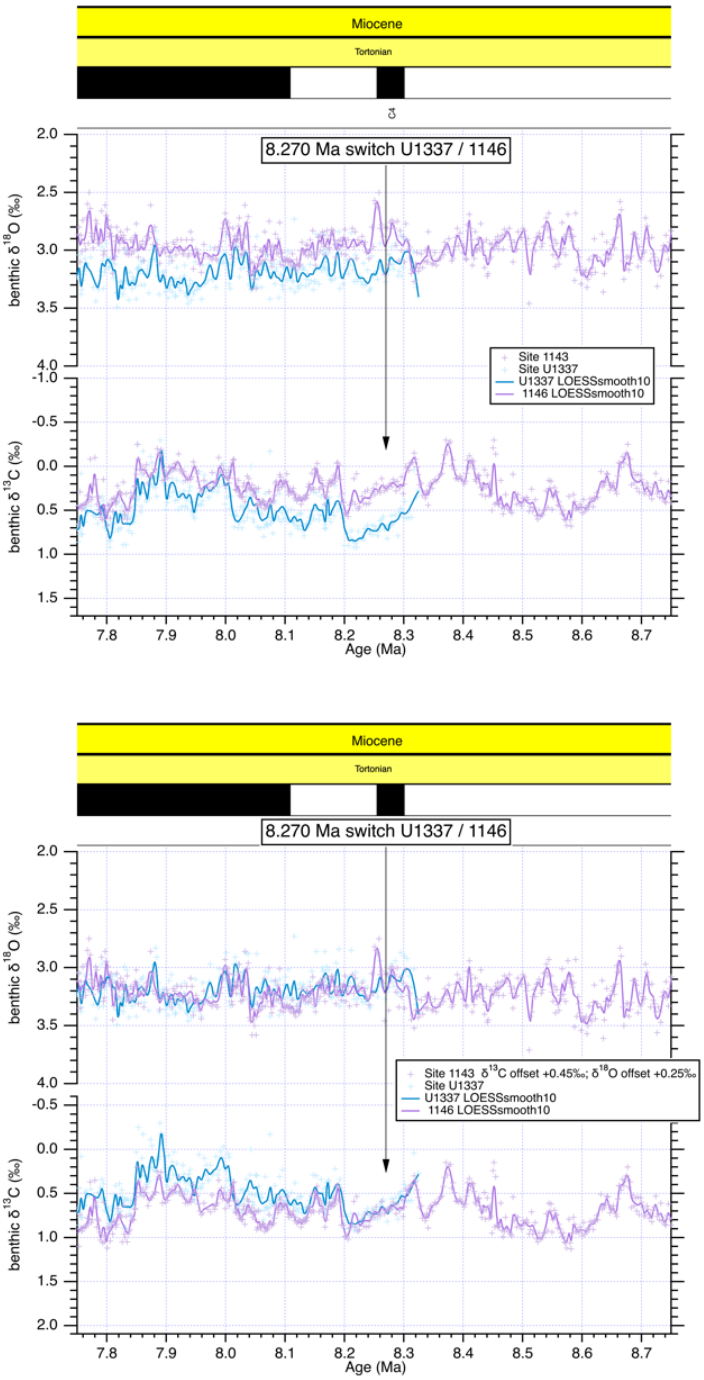

Fig. S17.

Switch at 8.270 Ma from Site U1337 to Site 1146. Top: benthic foraminifer $\delta^{13}C$ and $\delta^{18}O$ raw data. Bottom: benthic data with offset for Site U1337 and Site 1146 spanning 7.75 to 8.75 Ma across reference record switch at 8.270 Ma.

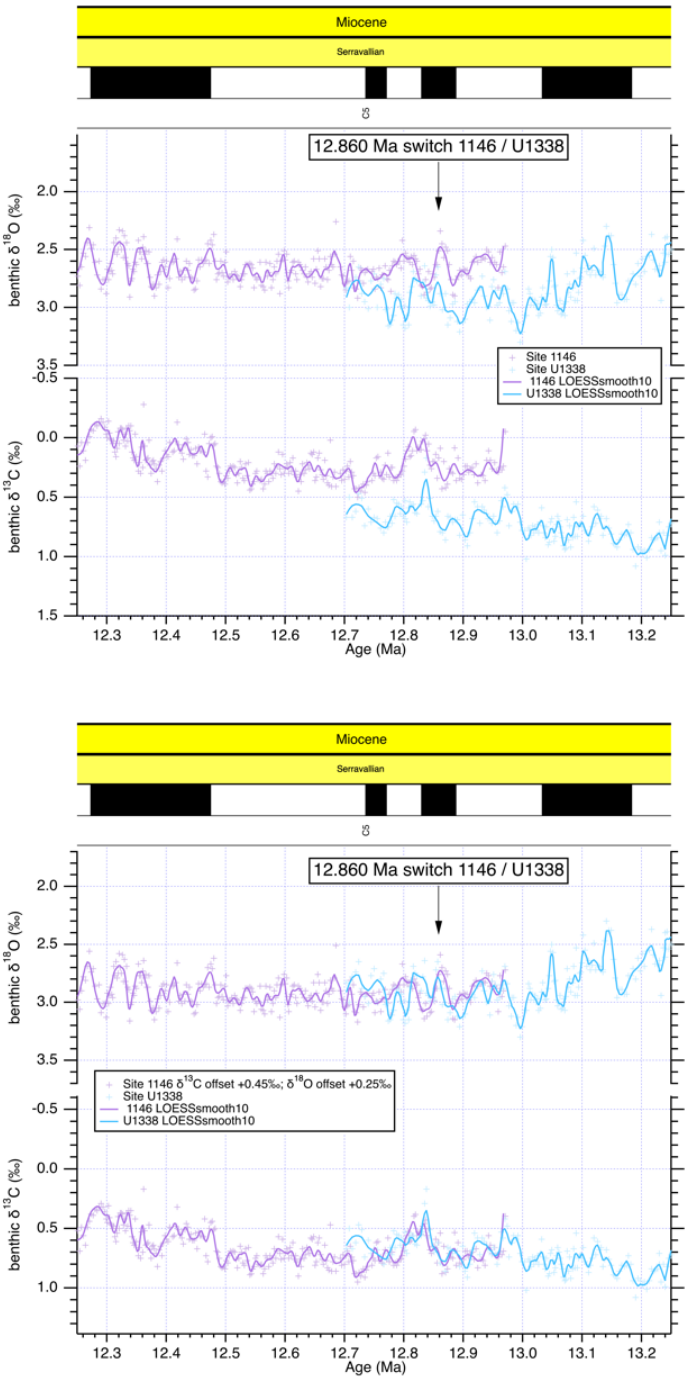

Fig. S18.

Switch at 12.860 Ma from Site 1146 to Site U1338. Top: benthic foraminifer $\delta^{13}C$ and $\delta^{18}O$ raw data. Bottom: benthic data with offset for Site 1146 to Site U1338 spanning 12.25 to 13.25 Ma across reference record switch at 12.860 Ma.

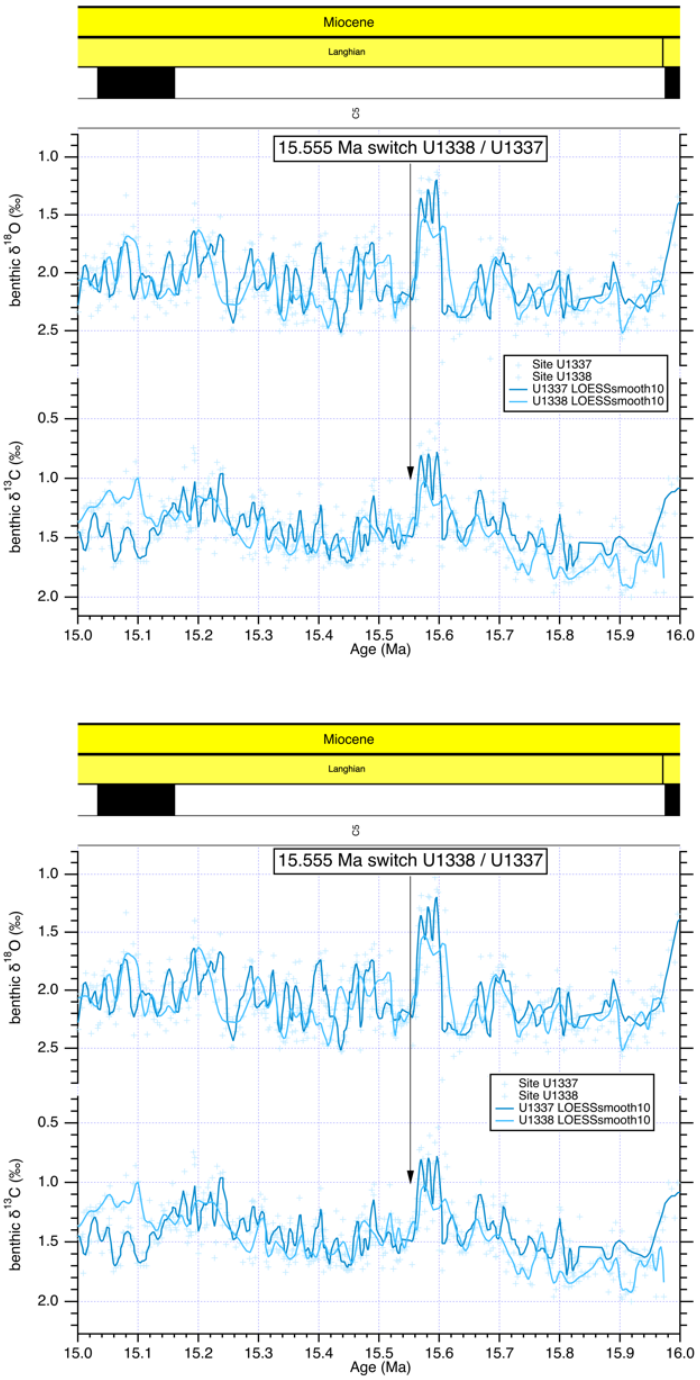

Fig. S19.

Switch at 15.555 Ma from Site U1338 to Site U1337. Top: benthic foraminifer $\delta^{13}C$ and $\delta^{18}O$ raw data. Bottom: benthic data with offset for Site U1338 to Site U1337 spanning 15.00 to 16.00 Ma across reference record switch at 15.555 Ma.

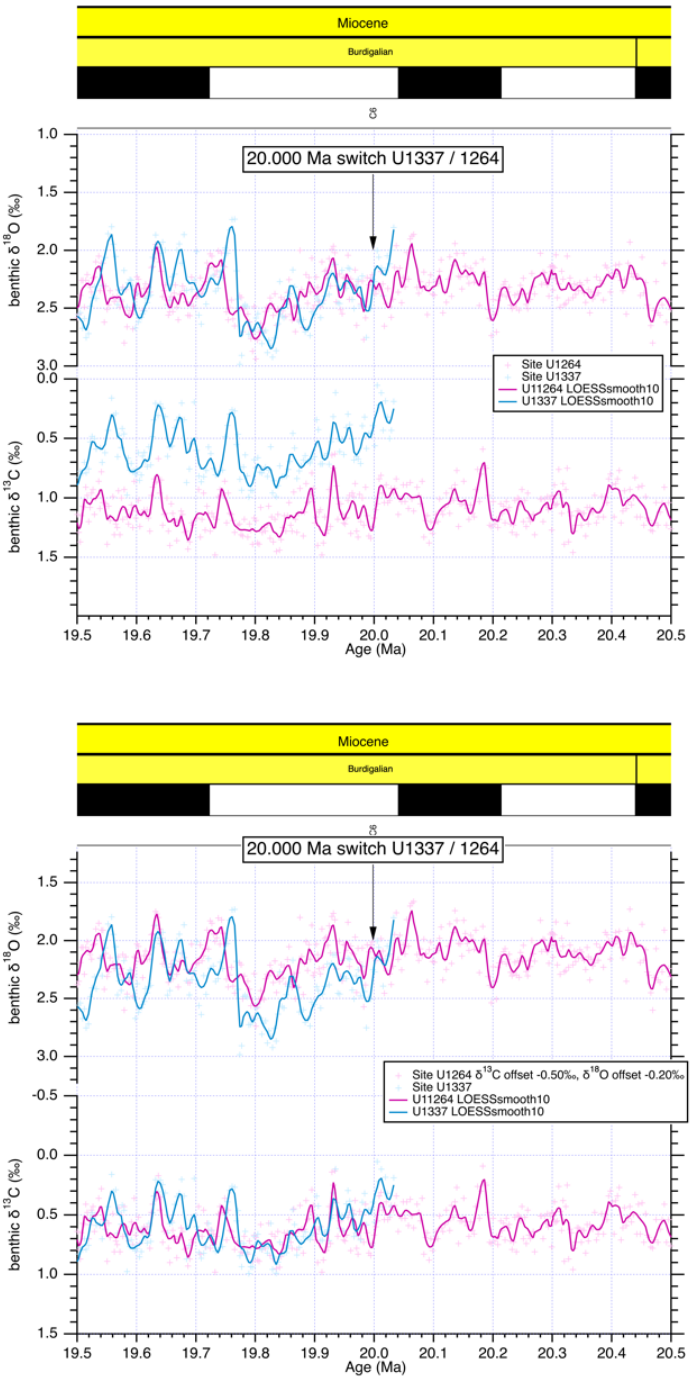

Fig. S20.

Switch at 20.000 Ma from Site U1337 to Sites 1264/1265. Top: benthic foraminifer $\delta^{13}C$ and $\delta^{18}O$ raw data. Bottom: benthic data with offset for Site U1337 to Sites 1264/65 spanning 19.50 to 20.50 Ma across reference record switch at 20.000 Ma.

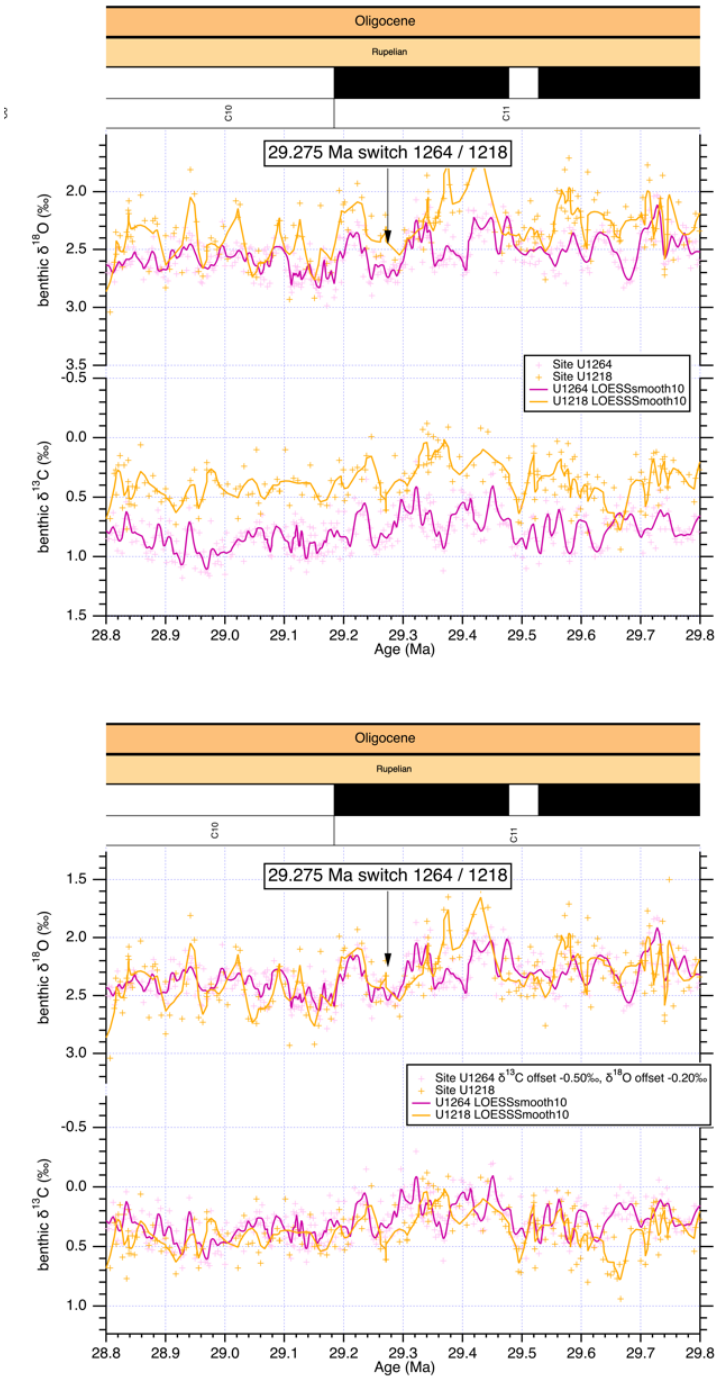

Fig. S21.

Switch at 29.275 Ma from Sites 1264/1265 to Site 1218. Top: benthic foraminifer $\delta^{13}C$ and $\delta^{18}O$ raw data. Bottom: benthic data with offset for Sites 1264/65 to Site 1218 spanning 28.80 to 29.80 Ma across reference record switch at 29.275 Ma.

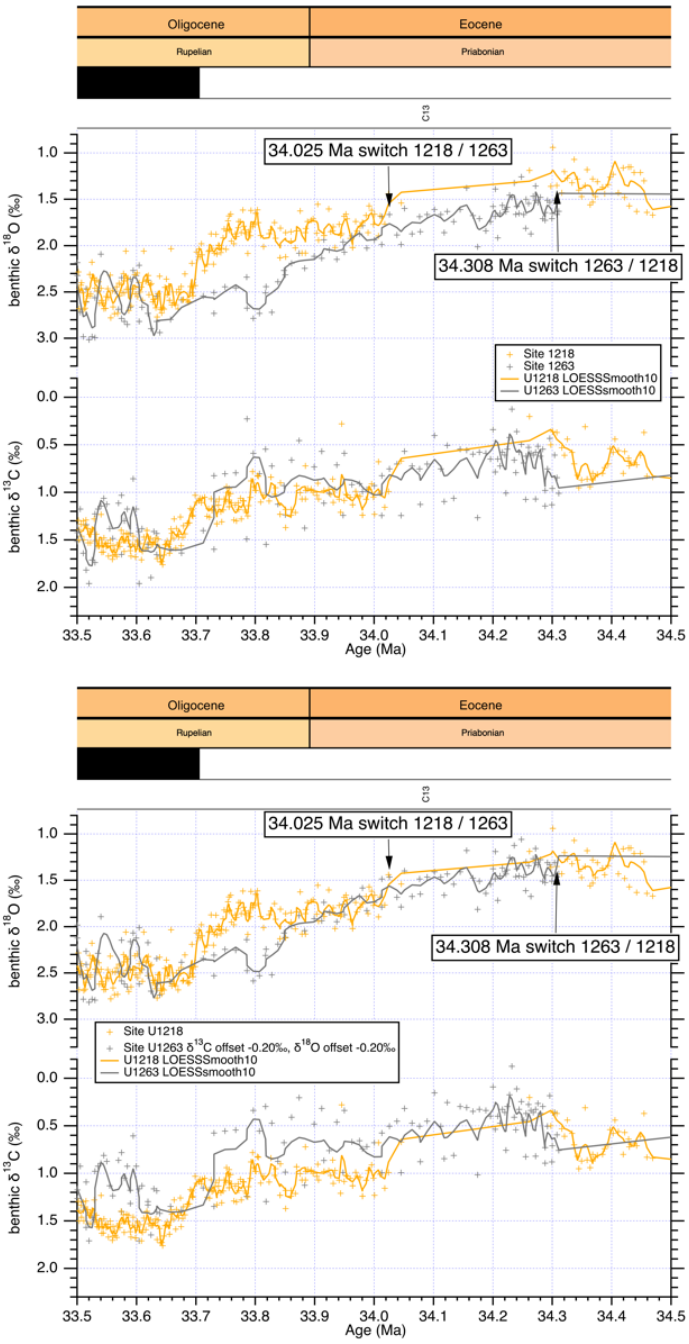

Fig. S22.

Switch at 34.025 Ma from Site 1218 to Site 1263 and back at 34.308 Ma. Top: benthic foraminifer $\delta^{13}C$ and $\delta^{18}O$ raw data. Bottom: benthic data with offset for Site 1218 to Site 1263 and back spanning 33.50 to 34.50 Ma across reference record switch at 34.025 and 34.308 Ma.

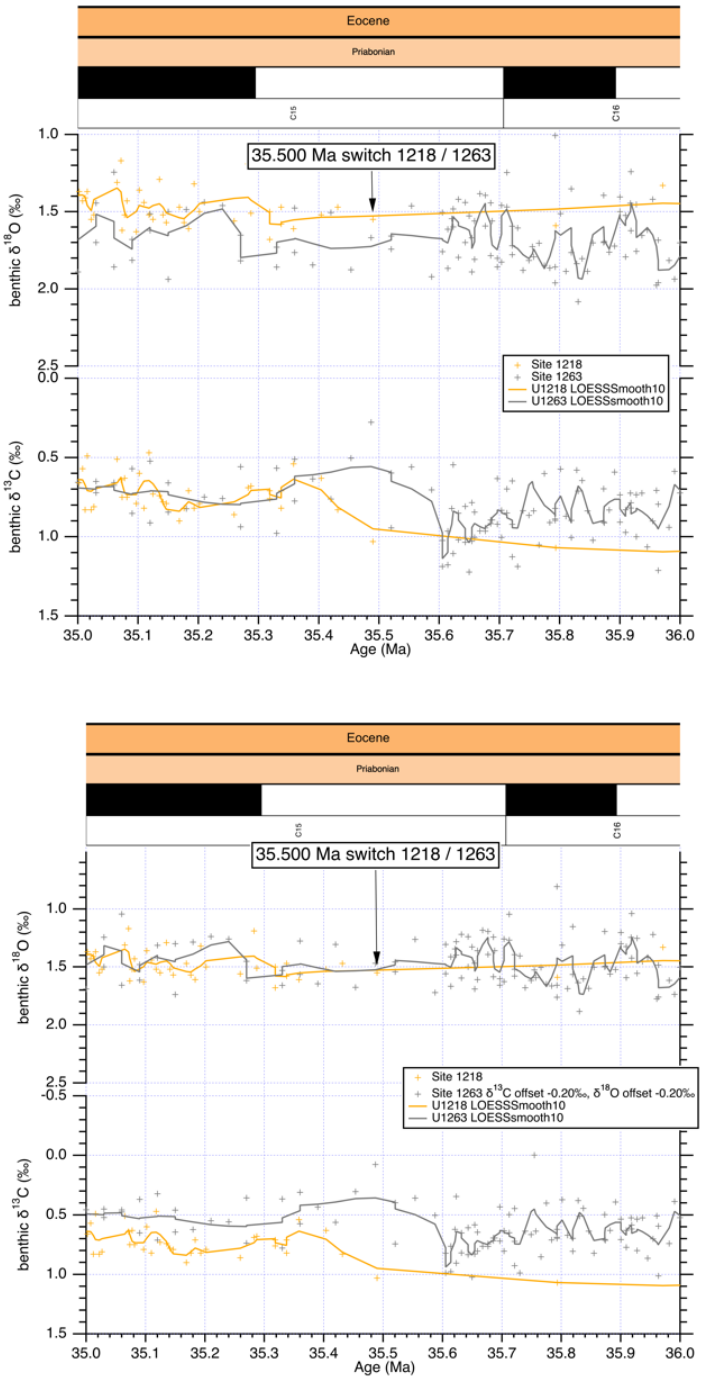

Fig. S23.

Switch at 35.500 Ma from Site 1218 to Site 1263. Top: benthic foraminifer $\delta^{13}C$ and $\delta^{18}O$ raw data. Bottom: benthic data with offset for 1218 to 1263 spanning 35.00 to 36.00 Ma across reference record switch at 35.500 Ma.

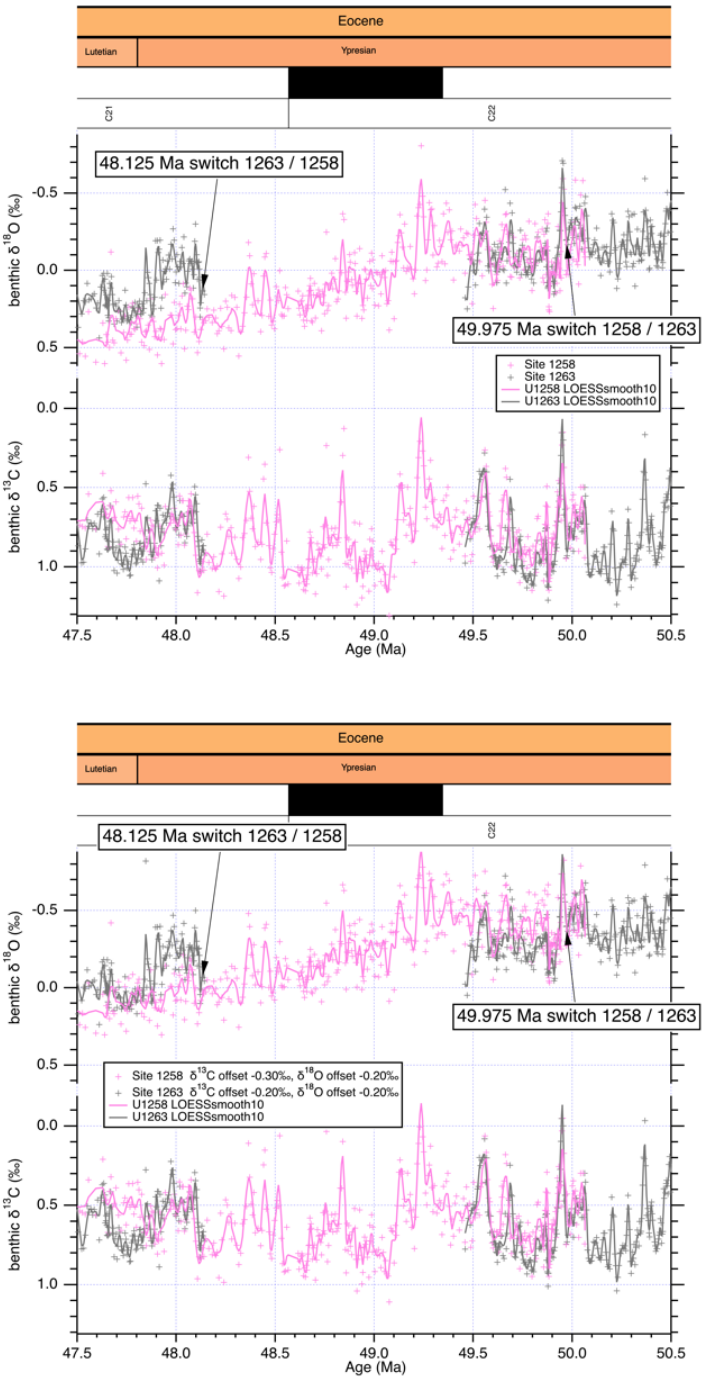

Fig. S24.

Switch at 48.125 Ma from Site 1263 to Site 1258 and back to Site 1263 at 49.975 Ma. Top: benthic foraminifer $\delta^{13}C$ and $\delta^{18}O$ raw data. Bottom: benthic data with offset for 1263 to 1258 and back to 1263 spanning 47.50 to 50.50 Ma across reference record switches at 48.125 Ma and 49.975 Ma.

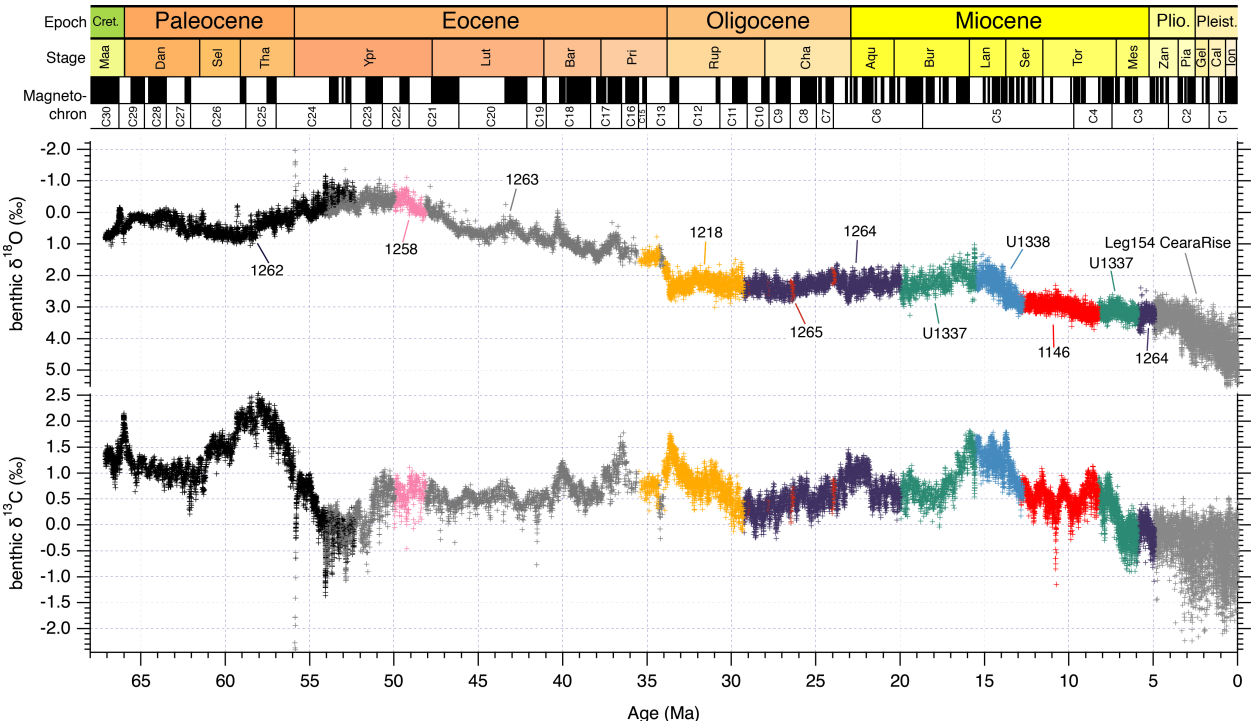

Fig. S25.

Combined astronomically-tuned benthic foraminifer stable carbon and oxygen isotope records forming the Cenozoic reference splice.

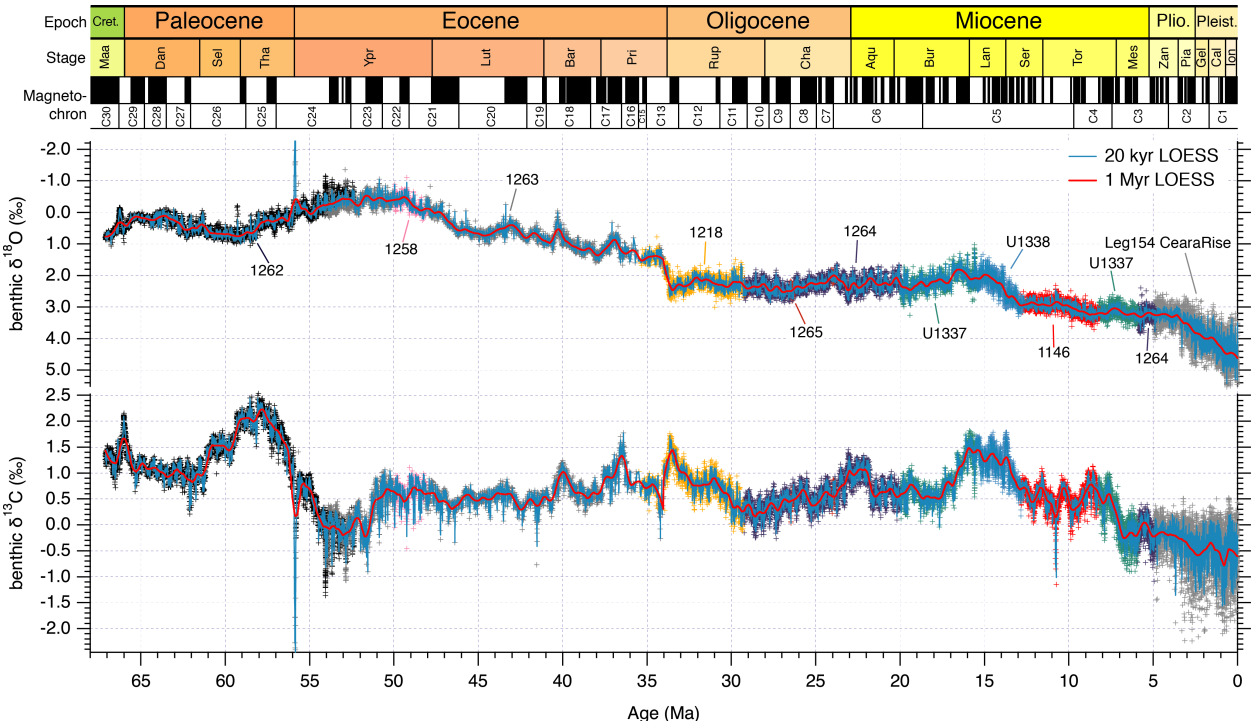

Fig. S26.

Short- and long-term LOESS smooth of the astronomically-tuned combined benthic foraminifer stable carbon and oxygen isotope records forming the Cenozoic global reference benthic carbon and oxygen isotope dataset (CENOGRID).

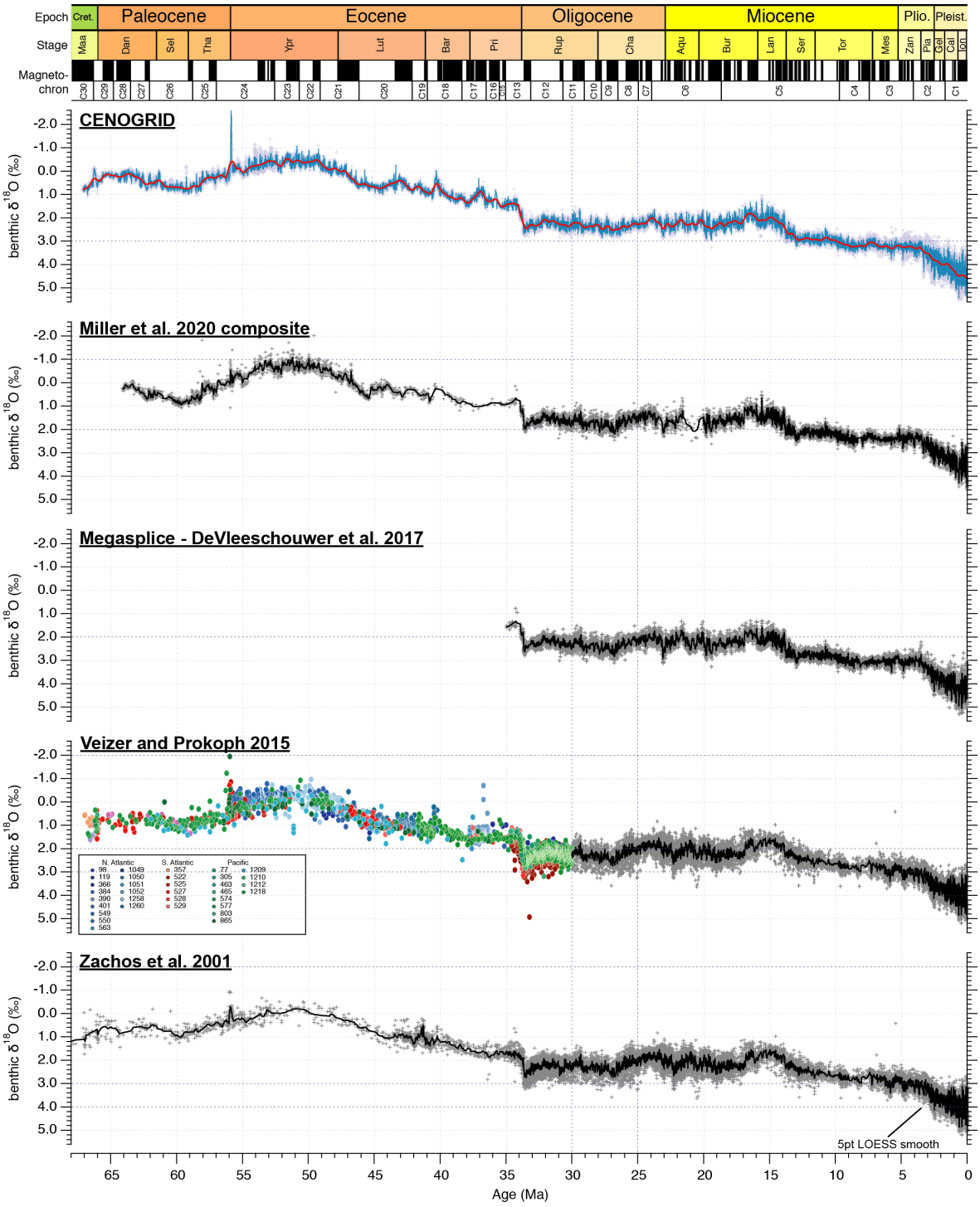

Fig. S27.

Benthic foraminifer stable oxygen isotope compilations from (*8*) and (*1*) as well as the Megasplice of (*5*) and the recent composite of (*10*) compared to the new composite Cenozoic reference global benthic carbon and oxygen isotope dataset (CENOGRID). Note the low resolution in the Paleocene and Eocene for the previous compilations.

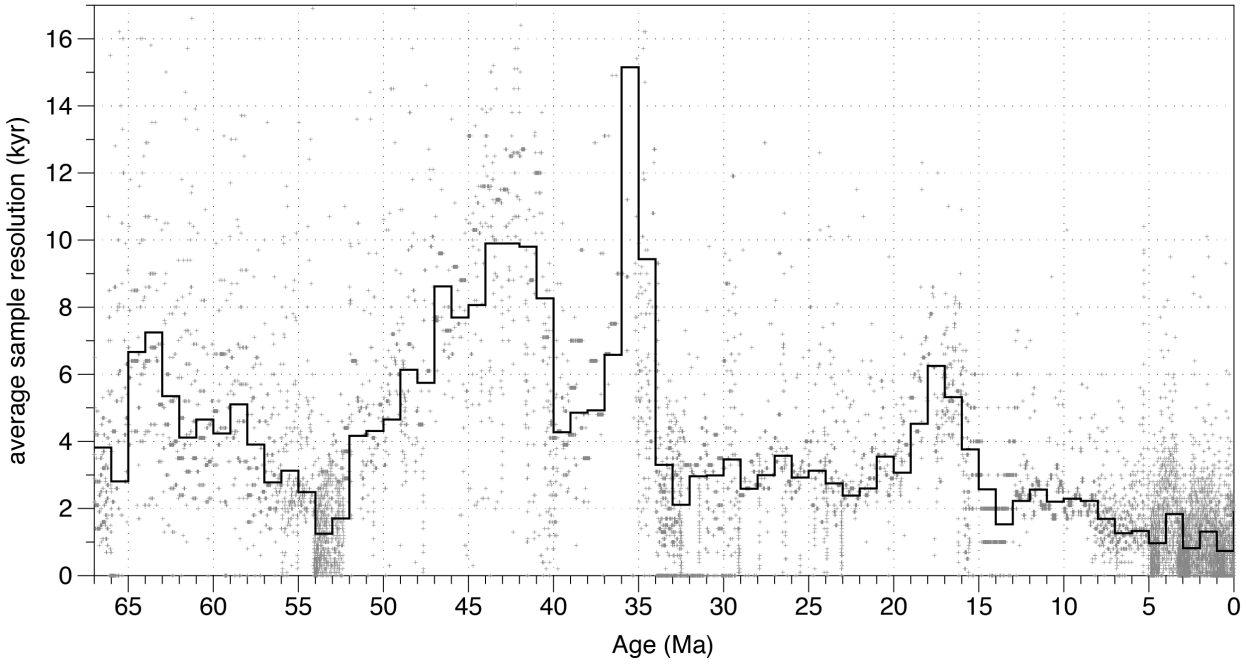

Fig. S28.

Average sample resolution over one million year intervals for the CENOGRID benthic stable isotope data.

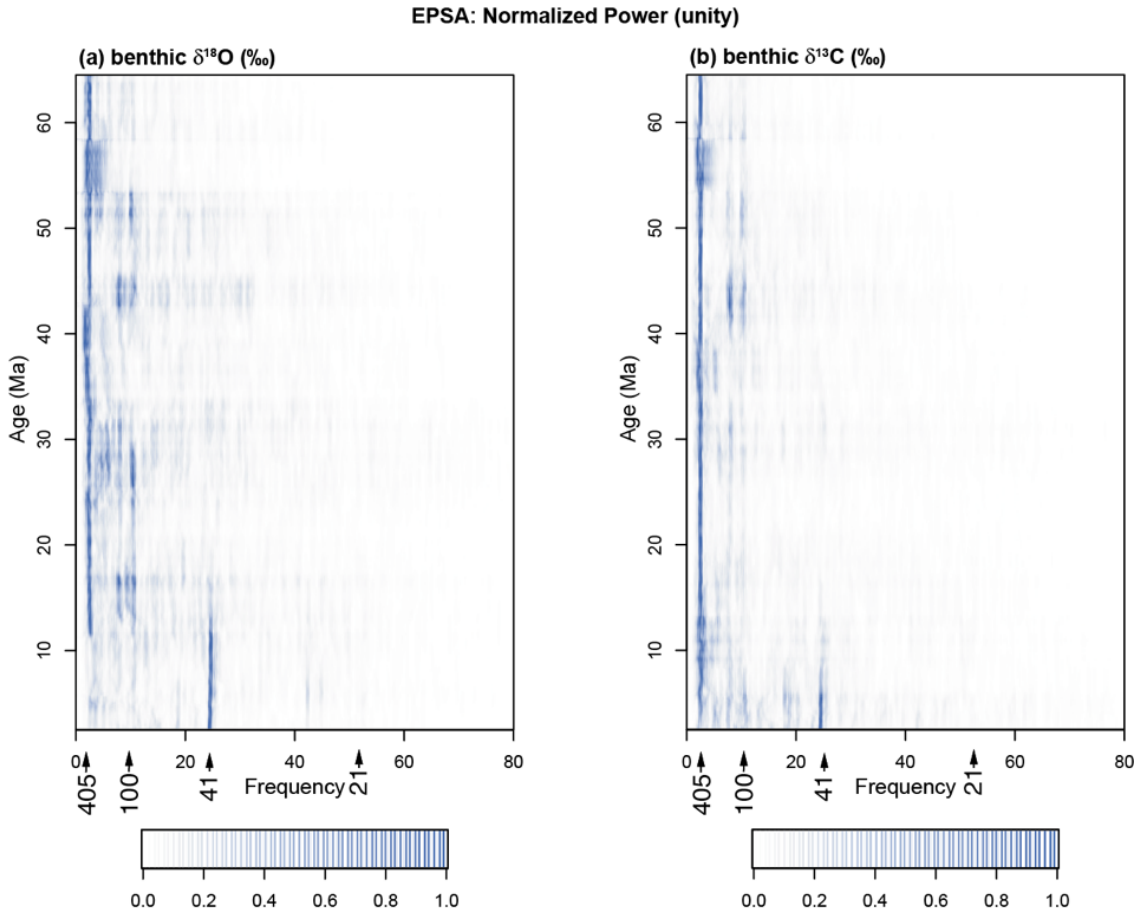

Fig. S29.

Evolutive Power Spectral Analysis (EPSA) on the short-term LOESS smooth of the astronomically-tuned CENOGRID using ASTROCHRON (*148*). The EPSA documents, as in Fig. 2, the dominance of the 405 kyr and ~100 kyr eccentricity cycles from 67 to 13.9 Ma. After 13.9 Ma enhanced obliquity related cyclicity appears first in the oxygen isotope record. In the carbon isotope data obliquity becomes more dominant around 7.7 million years ago. Isotope data have been detrended by the long-term LOESS smooth trend and evenly samples every 2 kyr. The following code was used to compute the spectra in ASTROCHRON:
eha(dat,tbw=2,65536,0,80,0.02,5,demean=T,detrend=T,siglevel=0.90,sigID=F,ydir=1,output=0,
pl=2,palette=3,centerZero=T,ncolors=100,"Frequency","Location",genplot=4,verbose=T).

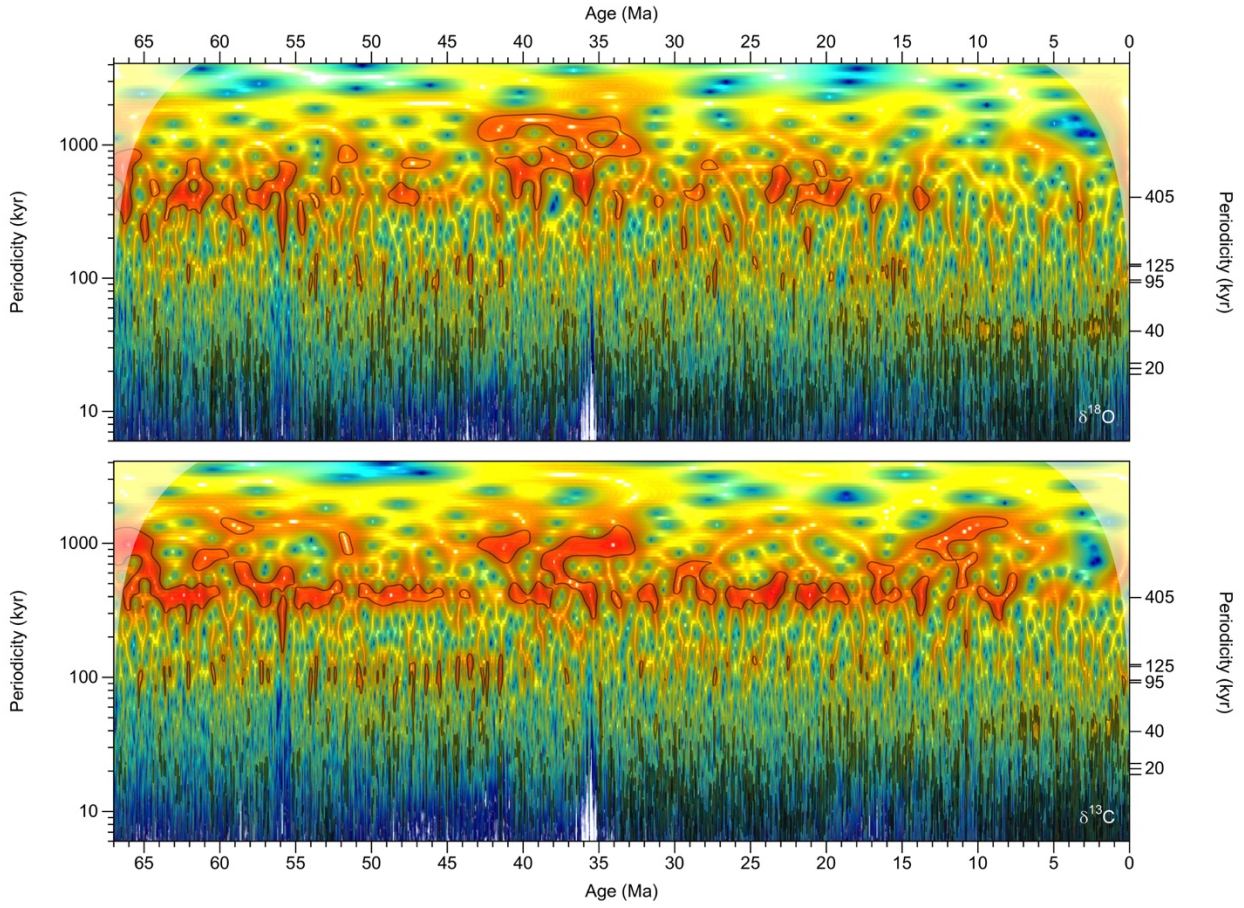

Fig. S30.

3D wavelets of the CENOGRID. Wavelet analysis of the Cenogrid $\delta^{18}O$ (top panel) and $\delta^{13}C$ (bottom panel), using a Morlet transform (*149,150*). Prior to wavelet analysis the records were resampled at 2.5 kyr resolution, detrended using a Notch filter (frequency = 0.0 Myr^{-1}, bandwidth = 1.0 Myr^{-1}) (*151*), and normalized using a 1-Myr sliding window. Gray lines indicate the 95% significance contours. Shaded areas indicate the cone of influence.

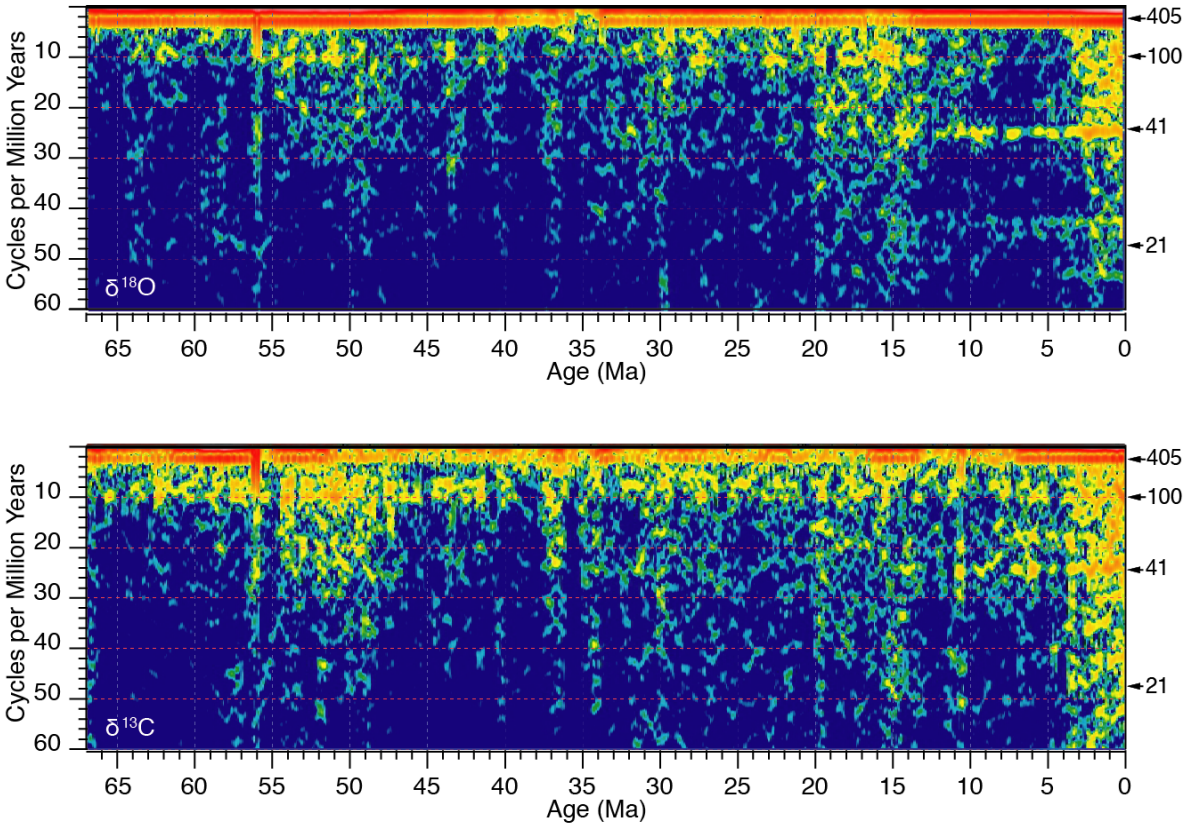

Fig. S31.

Evolutive spectra of CENOGRID computed using the Thomson Multi-taper method (*122*), with v.0.0.7 Spectrogram tool (https://paloz.marum.de/confluence/display/ESPUBLIC/Spectrogram). Data were interpolated to even time steps, and then computed with 700kyr windows stepped every 70kyr. MTM settings were bandwidth product: 3, number of tapers: 4. For the isotope data, the amplitudes are displayed on a logarithmic scale.

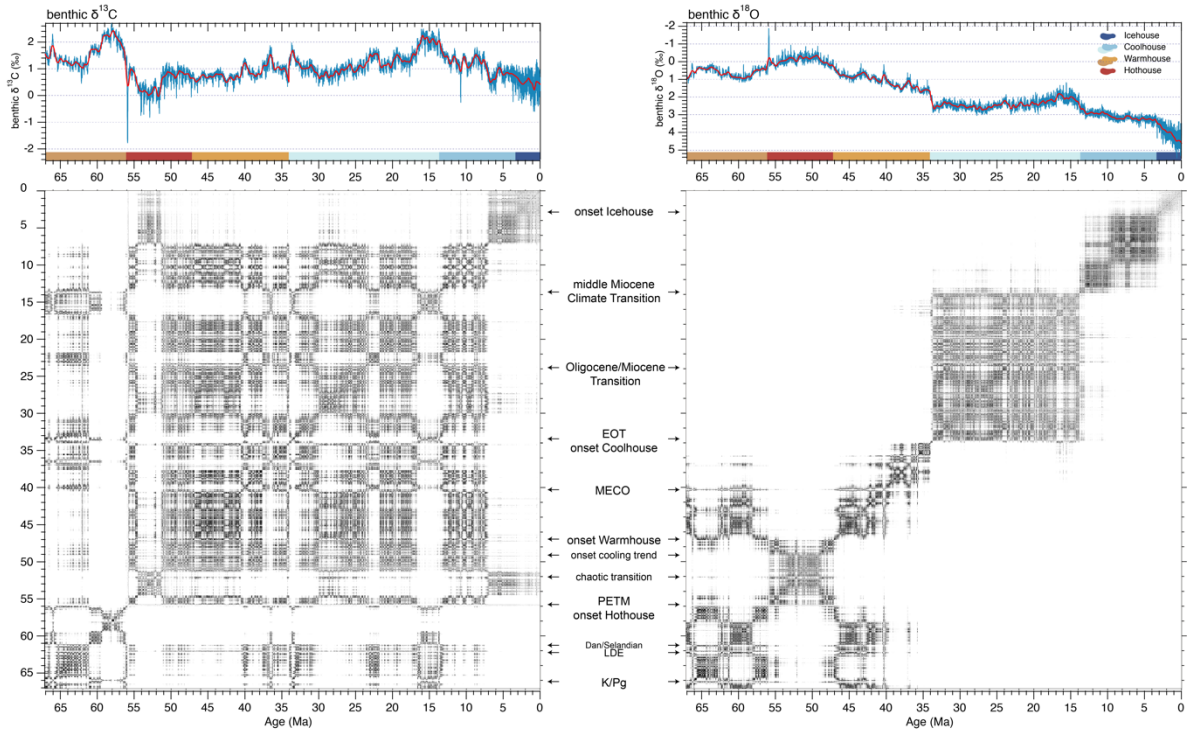

Fig. S32.

Recurrence Plot of undetrended benthic foraminifer carbon (left) and oxygen (right) isotope data versus age; important transitions and events given.

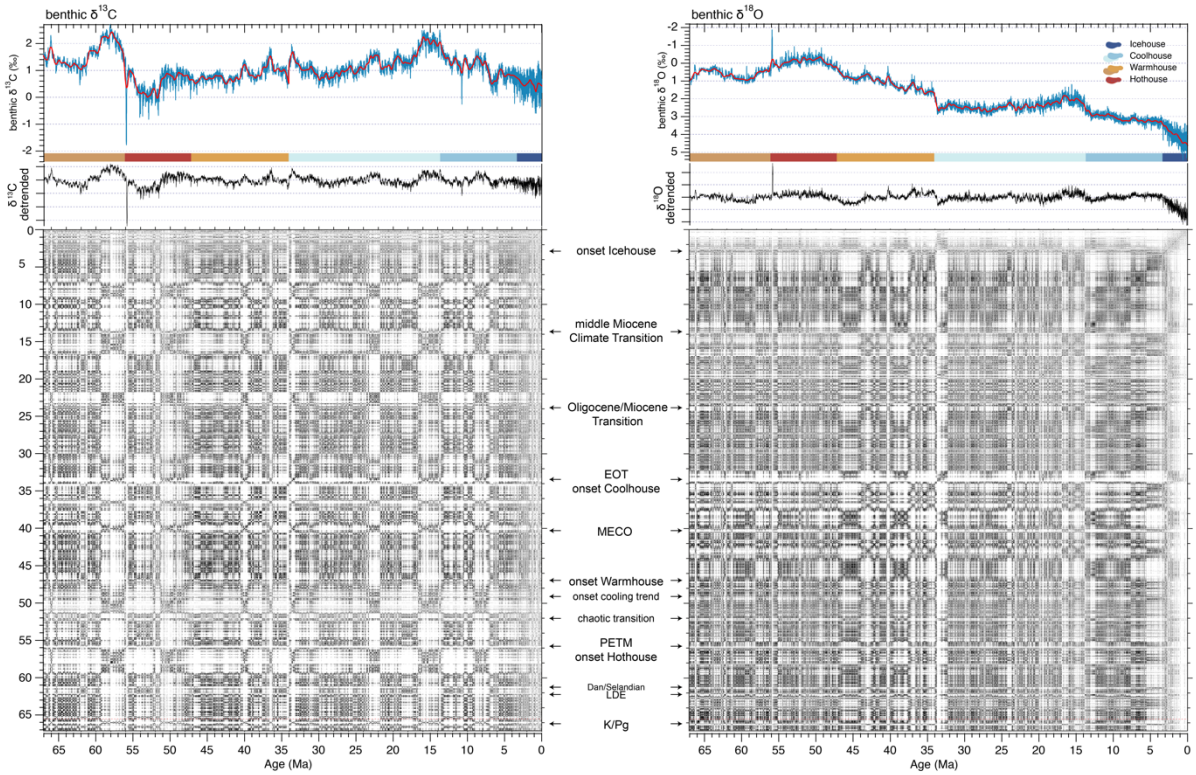

Fig. S33.

Recurrence Plot of detrended benthic foraminifer carbon (left) and oxygen (right) isotope data versus age; important transitions and events given. Note: transparent areas mark transition zones and events.

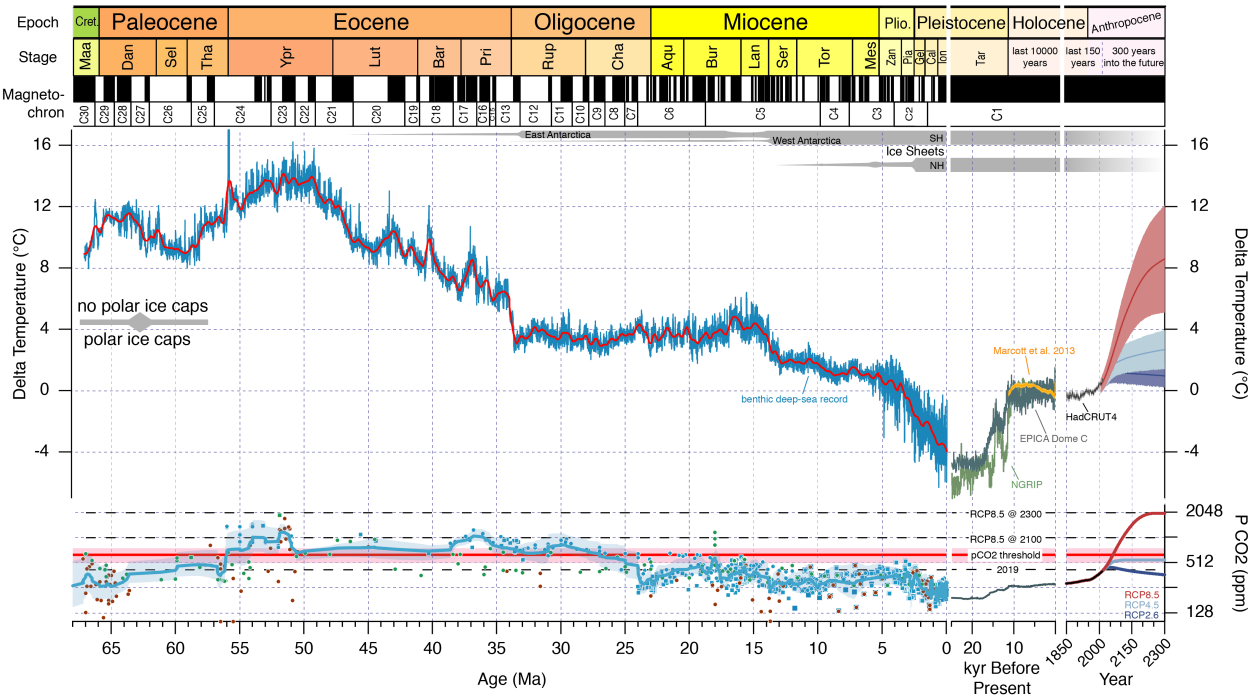

Fig. S34.

Past and future trends in global mean temperature and atmospheric CO_2. Deep-sea benthic foraminifer oxygen isotope values spanning the last 67 million years are a measure of global temperature and ice volume. Here the record was first converted to a deep-sea temperature and then projected to surface air temperature change (92). Temperature is relative to the 1961–1990 global mean, and plotted along with estimates for past atmospheric CO_2 levels (see *Section 6. and supplementary Text S1*). Temperature and CO_2 data from ice core records of the last 25,000 years illustrate the transition from the last glacial to the current warmer period, the Holocene. Historic data from 1850 to today ((*152, 153*); 415 ppm www.esrl.noaa.gov/gmd/ccgg/trends) show the distinct increase for both constituents after 1950 marking the onset of the Anthropocene (*154*). Future projections for global temperature (*44*) and CO_2 (*139*) for three Representative Concentration Pathways (RCP) scenarios in relation to the benthic deep-sea record suggest that by 2100 the climate state will be comparable to the Miocene Climate Optimum (~16 million years ago), way beyond the threshold for nucleating continental ice sheets (*140*). If emissions are constant after 2100 and are not stabilized before 2250, global climate by 2300 might enter the hothouse world of the early Eocene (~50 million years ago) with its multiple global warming events and no large ice sheets at the poles.

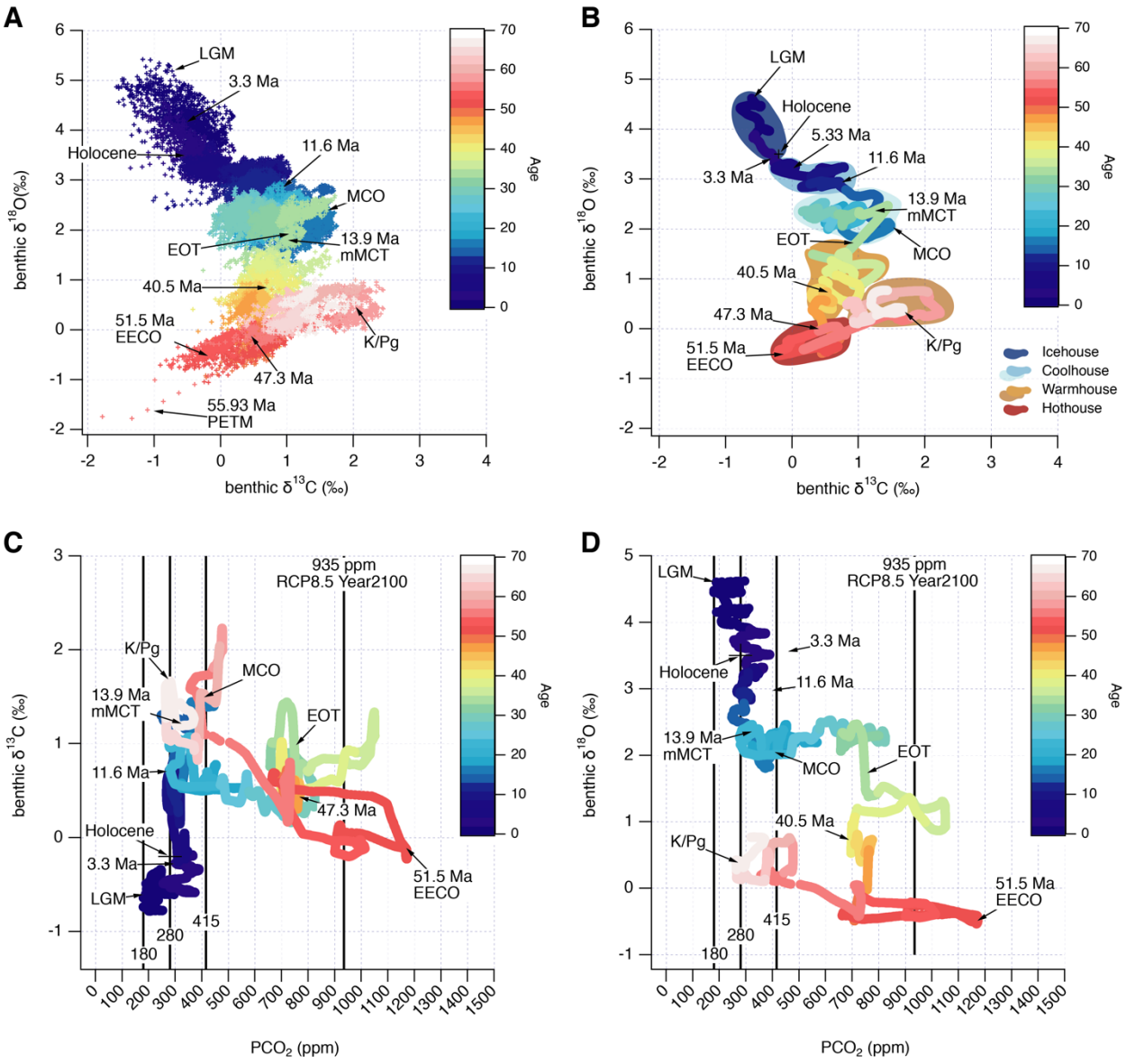

Fig. S35.

Scatter plots of deep-sea benthic high-resolution (A) and long-term (B) carbon versus oxygen isotope data variations as well as long-term atmospheric CO_2 concentrations versus benthic carbon (C) and oxygen (D) isotope data. The relation to atmospheric CO_2 concentrations for both carbon and oxygen, as representative for the global carbon cycle and temperature trends, suggests that the present climate system as of today 415 ppm CO_2 is comparable to the Coolhouse in the Miocene, but will move abruptly into the Warmhouse or even Hothouse by 2100 if emissions of CO_2 are not diminished.

Table S1.

Details on the applied age models for the CENOGRID

Interval	Site	Source / Note
0 to 6 Ma	925, 926, 927, 928, 929	Wilkens et al. 2017, Zeeden et al. 2013, Drury et al. 2017 (*22, 54, 155*)
0 to 6.1 Ma	1264	3.3 to 6.1 Drury pers.comm, Bell et al. 2014 (*51*) updated 0 to 3.3 Ma
5.9 to 8.3 Ma	U1337	Drury et al. 2017 (*22*)
5.1 to 13 Ma	1146	Holbourn et al. 2018 (*67*), corrected due to a doubling of strata in the composite record (DeVleeschouwer/Drury)
12.7 to 16 Ma	U1338	Holbourn et al. 2014 (*68*)
15 to 20 Ma	U1337	Holbourn et al. 2015 (*20*)
17 to 30.7 Ma	1264, 1265	Liebrand et al. 2016 (*120*)
18.6 to 41.3 Ma	1218	18.6 to 28.8 Ma Pälike et al. 2006 (*35*) refined to minimal tuning 28.8 to 30.8 Ma this study to connect above and below 30.8 to 41.3 Ma Westerhold et al. 2014 (*156*)
32.7 to 42 Ma	1263, 1265	this study, Rivero-Cuesta et al. 2019 (*157*)
42 to 67 Ma	1258, 1262, 1263	Westerhold et al. 2017, 2018 (*16, 52*) with a refinement for 48.4 to 49.6 Ma and from Barnet et al. 2019 (*88*) updated to La2010b

Age models for each site given in Tab. S24 to S32.

Table S2.

Isotopic correction factors applied for Paleocene and Eocene benthic foraminifer stable isotopes

Taxa pairs		Formula	Source
Cibicidoides	O18	(Cib * 0.89) - 0.10 = Nutt	Katz et al. 2003 (*12*)
N. truempyi	C13	Cib - 0.34 = Nutt	Katz et al. 2003 (*12*)
Cibicidoides	O18	Orid - 0.28 = Cib	Katz et al. 2003 (*12*)
Oridorsalis	C13	Orid + 0.72 = Cib	Katz et al. 2003 (*12*)
N. truempyi	O18	(Orid - 0.416) / 0.909 = Nutt	Westerhold et al. 2018 (*16*)
Oridorsalis	C13	(Orid + 0.372) / 0.971 = Nutt	Westerhold et al. 2018 (*16*)
N. truempyi	O18	(Cprae - 0.474) / 0.792 = Nutt	this study
C. praemundulus	C13	(Cprae - 0.617) / 0.565 = Nutt	this study

Table S3.

Adjustment factors applied to the isotopic measurements of benthic foraminifer species in order to obtain the best estimates of oxygen isotopic equilibrium and carbon isotopic composition of ocean deep-water dissolved CO_2.

Species	Abbr.	d18O Offset	d13C offset	Source
Paleocene/Eocene				
Cib	CSPP	+0.64	0.00	Shackleton et al., 1984 (*81*)
Nutt	NTRUE	+0.40	0.00	Shackleton et al., 1984 (*81*)
Oligocene/Neogene				
Cibicidoides kullenbergi	CKULL	0.64	0.00	Shackleton et al. 1995 (*158*)
Cibicidoides wuellerstorfi	CWUEL	0.64	0.00	Shackleton et al. 1984 (*81*)
Cibicidoides spp.	CSPP	0.50	0.00	Shackleton et al. 1984 (*81*)
Cibicidoides bradyii	CBRA	0.64	0.00	Bickert et al. 1997 (*159*)
Cibicidoides cicatricosus	CCIC	0.64	0.00	Bickert et al. 1997 (*159*)
Globocassidulina subglobosa	GLOSUB	-0.10	0.50	Shackleton et al. 1995 (*158*)
Gyroidina orbicularis	GORB	0.00	0.00	Shackleton et al. 1995 (*158*)
Nuttalides umbonifera	NUMB	0.35	0.00	Shackleton and Hall 1997 (160)
Oridorsalis spp.	ORID	0.00	1.00	Shackleton et al. 1995 (*158*)
Oridorsalis umbonatus	OUMB	0.00	1.00	Shackleton et al. 1984 (*81*)
Pyrgo murrhina	PMUR	0.00	0.90	Shackleton and Opdyke 1973 (*161*)
Uvigerina spp.	UVIG	0.00	0.90	Shackleton et al. 1995 (*158*)

Table S4.

Applied offsets for individual stable isotope records using equatorial Pacific records as global baseline

Site	Source of benthic data	Age Interval	$\delta^{18}O$	$\delta^{13}C$
Ceara Rise	Wilkens et al. 2017 (*54*)	0.000 to 4.925 Ma	+0.45 ‰	-1.00 ‰
1264	this study, Bell et al. 2014 (*51*)	4.925 to 5.975 Ma	±0.00 ‰	-1.00 ‰
1146	Holbourn et al. 2013,'18 (*36, 67*)	8.270 to 12.860 Ma	+0.25 ‰	+0.45 ‰
1264	Liebrand et al. 2016 (*120*)	20.000 to 29.275 Ma	-0.20 ‰	-0.50 ‰
1263	Riesselmann et al. 2007 (*50*)	34.025 to 34.308 Ma	-0.20 ‰	-0.20 ‰
1263	this study	34.308 to 48.125 Ma	-0.20 ‰	-0.20 ‰
1258	Sexton et al. 2011 (*162*)	48.125 to 49.975 Ma	-0.30 ‰	-0.20 ‰
in the interval older than 49.975 Ma all records from Leg 208			-0.20 ‰	-0.20 ‰

Table S5.

Definition of intervals and records used to define a complete high fidelity benthic foraminifer stable isotope reference splice

Age Interval	Site	Source of benthic stable isotope data
0 to 4.925 Ma	925, 926, 927 928,929	Bickert et al. 1997, deMenocal et al. 1997, Tiedemann and Franz 1997, Billups et al. 1998, Franz and Tiedemann 2002
4.925 to 5.975 Ma	1264	this study, Bell et al. 2014
5.975 to 8.270 Ma	U1337	Drury et al. 2017, Tian et al. 2018
8.270 to 12.860 Ma	1146	Holbourn et al. 2007, 2013, 2018
12.860 to 15.555 Ma	U1338	Holbourn et al. 2014
15.555 to 20.000 Ma	U1337	Tian et al. 2014, Holbourn et al. 2015
20.000 to 29.275 Ma	1264, 1265	Liebrand et al. 2011, 2016
29.275 to 34.025 Ma	1218	Lear et al. 2004, Wade and Pälike 2004, Pälike et al. 2006, Coxall et al. 2005, Coxall and Wilson 2011
34.025 to 34.308	1263	Riesselmann et al. 2007
34.308 to 35.500	1218	Lear et al. 2004, Coxall et al. 2005, Coxall and Wilson 2011
35.500 to 48.125 Ma	1263	this study, Boscolo Galazzo et al. 2014, Westerhold et al. 2018
48.125 to 49.975 Ma	1258	Sexton et al. 2011
49.975 to 67.103 Ma	1262, 1263	Lauretano et al. 2015, 2016, 2018; Littler et al. 2014; Barnet et al. 2017, 2019; Stab et al. 2010; Hull et al. 2020, Thomas et al. 2018

Citations: (*17, 20, 22, 35, 36, 50, 51, 67, 68, 77, 88, 120, 159, 162-181)*

Table S6.

Benthic foraminifer reference splice average resolution and smoothing details

Action item	0.000 to 34.025 Ma	34.025 to 67.100 Ma	
Average sample resolution	2 kyr	4.4 kyr	
Binning interval	2 kyr	5 kyr	
Resampling resolution	2 kyr	5 kyr	
LOESS smooth of resampled series	10 points	5 points	= 20kyr
Long term LOESS smooth	500 points	250 points	= 1 myr

Note: To minimize the effects of outliers the records were smoothed in IGOR Pro 8 using a nonparametric LOESS quadratic regression smooth with a tricube locally-weighted function. For sample resolution overview see Fig. S28.

Table S7.

Equations to calculate deep-sea temperature and surface air temperature (Hansen et al. 2013) (*86*).

Deep Sea Temperature T_{do}		
0.000 to 3.660	T_{do} (°C) = 1 – 4.4 * ((δ18O (‰) – 3.25) / 3)	(1)
3.600 to 34.025	T_{do} (°C) = 5 – 8 * ((δ18O (‰) – 1.75) / 3)	(2)
34.025 to 67.000	T_{do} (°C) = (−4 * δ18O (‰)) + 12	(3)
Surface air temperature change T_S		
0.000 to 1.810	T_s (°C) = 2 * Tdo + 12.25	(4)
1.810 to 5.330	T_s (°C) = 2.5 * Tdo + 12.15	(5)
5.330 to 67.000	T_s (°C) = Tdo + 14.15	(6)
Temperature anomaly with respect to average global temperature from 1961-1990		
Delta Temperature = Surface air temperature – 14.15 (Holocene mean temperature)		(7)